RICE UNIVERSITY

Plasmonic Properties of Nanoparticle-Film Systems and Periodic Nanoparticle Arrays

by

Fei Le

A THESIS SUBMITTED
IN PARTIAL FULFILLMENT OF THE
REQUIREMENTS FOR THE DEGREE

DOCTOR OF PHILOSOPHY

APPROVED, THESIS COMMITTEE:

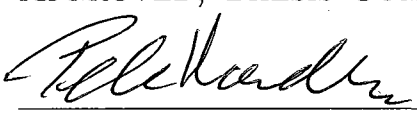

Peter Nordlander, Chair
Professor of Physics and Astronomy;
Professor of Electrical and Computer Engineering

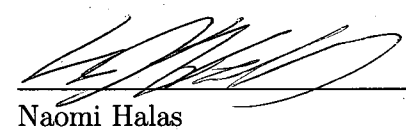

Naomi Halas
Stanley C. Moore Professor of Electrical and Computer Engineering; Professor of Chemistry

Jason Hafner
Associate Professor of Physics and Astronomy; Associate Professor of Chemistry

Houston, Texas
October, 2008

ABSTRACT

Plasmonic Properties of Nanoparticle-Film Systems and Periodic Nanoparticle Arrays

by

Fei Le

In this thesis we perform theoretical investigations on the optical properties of geometrically infinite metallic nano-structures such as nanoparticle / film systems and periodic nanoparticle arrays. We apply both Plasmon Hybridization (PH) and Finite-Difference Time-Domain (FDTD) methods and we obtain quantitative agreement with experimental measurements as well as other theoretical methods such as Mie Theory and Finite Element simulation.

For the nanoparticle over film structure, our research shows that the plasmonic interaction between the nanoparticle and the film is an electromagnetic analogue of the spinless Anderson-Fano model, which was used to describe the interaction of a localized electronic state with a continuous band of electronic states. Three characteristic regimes of the model are realized as the energy of the nanoparticle plasmon resonance lies above, within, or below the energy band of the surface plasmon state. These three

interaction regimes are controlled by the film thickness. In the thin film limit, The plasmonic coupling between the nanoshell and the film induces a low-energy virtual state (VS) mainly composed of delocalized film, which can be further tuned as the aspect ratio of the nanoshell changes. The calculations are found to agree well with experimental measurements. Using FDTD method, we show that the electromagnetic field enhancement induced by the VS in the thin film limit can be very large and the nanoparticle / film system could serve as an ideal substrate for Surface Enhanced Raman Spectroscopy (SERS) and Tip Enhanced Raman Spectroscopy (TERS).

The plasmonic properties of nanoparticle arrays are investigated using FDTD with Periodic Boundary Conditions (PBC). Our research shows that 2D hexagonal (hcp) nanoshell arrays possess ideal properties as a substrate that combines SERS and Surface Enhanced Infrared Absorption (SEIRA), with large electric field enhancements at the same spatial locations in the structure. With small interparticle distance and normal incidence, the multipolar plasmons of each constituent nanoshells hybridize and form band structures. For SERS, a relatively narrow near infrared (NIR) plasmon resonance is induced by the quadrupolar plasmonic interactions among neighboring nanoshells. For SEIRA, an extremely broad mid infrared (MIR) is induced by the dipolar resonances of the nanoshells. The relation between the field enhancements and the interparticle separation in the MIR regime is systematically investigated using an electrostatic model.

We apply the Multiple Unit Cell (MUC) PBC implementation for calculating the optical properties of periodic nanoparticle arrays for oblique excitations using the Finite-Difference Time-domain method. We discuss computational and numerical aspects and present a detailed investigation of its convergence properties. We investigate the extinction spectra of one-dimensional metallic nanosphere arrays under different incident angles and polarizations. The dispersion relation of the transverse and the longitudinal plasmon modes are calculated and found to be in qualitative agreement with simple electrostatic models.

Acknowledgments

I am deeply grateful to my advisor, Prof. Peter Nordlander for his guidance and encouragement. His exceptional intuition in physics and his persistent desire for beautiful and simple physical pictures have been constantly inspiring my research. I would like to thank my previous and current group members, Dr. Chris Oubre, Dr. Daniel Brandl, Dr. Emil Prodan, Mr. Yanpeng Wu, Mr. Feng Hao, Mr. Britan Willingham, Mr. Tae-ho Park, Mr. Tamer Ali, Dr. Chizuko Dutta, for their invaluable discussions. I would like to thank my collaborators in research, Dr. Hui Wang, Dr. Javier Aizpurua, Dr. Yaroslav Urzhumov, Prof. Mikael Käll, for their contributions and enlightenment to my research. I would like to thank Prof. Naomi Halas, Prof. Jason Hafner for taking time off their busy schedules to participate in my thesis defense. I also would like to thank the Laboratory for Nanophotonics (LANP), a great platform for my exposure to latest publications and discussions with experimentalists. I would like to thank my family, especially my wife Yawen who has been constantly supporting me. I also would like to give credits to the funding providers. This work is supported by the U.S. Army Research laboratory and the U.S. Army Research Office under contract / grant number W911NF-04-1-0203, the Robert A. Welch Foundation under grant C-1220 and C-1222, and by NSF under grants EEC-0304097 and ECS-0421108.

Contents

List of Figures

Chapter 1
Introduction

Plasmonics is an intriguing field of science which focuses on plasmons, the collective oscillations of the free electron gas density[1]. Similar to photons and phonons, plasmons can be considered as quasi-particles originated from the quantization of plasma oscillations in metals. Using the Drude model[2], metals are treated as free electron gas sitting on top of a uniform, positive charge background. The bulk plasmon energy is usually considered as a constant that only depends on the free electron density n_0 and takes the form $\omega_0 = \sqrt{4\pi n_0 e^2/m_e}$, where m_e is the electron mass.

Plasmons crucially determine the optical properties of metals. For example, incident electromagnetic waves with frequency below the bulk plasmon frequency is reflected since the electric field in the incident light is screened by the free electrons in the metal. In most metals and some semiconductors, the bulk plasmon level is at ultraviolet, hence leading to their shiny colors because of a nearly total reflection of incident visible light.

Surface plasmons are the plasmons which propagate exclusively on the surfaces of metals. The interaction between plasmons and photons is often strong enough to create quasi-particles called surface polaritons[3, 4] at the interface between materials with positive dielectric constants (glass, air, vacuum, etc.) and materials with

negative dielectric constants (most metals). A striking feature of surface plasmon is its capability of controling the color of a metallic object by changing its geometric properties. Since surface plasmon strongly depends on the geometric parameters of the metallic surfaces, changing the shape or size of the object alters the resonant and propagating wavelengths of surface plasmons. This in turn controls the coupling between light and the surface plasmons.

The experimental research on surface plasmons has recently been pushed into visible light regime by the rapid development in nanotechnogy. Highly advanced fabrication techniques, such as self-assembly method, Electron-Beam Direct-Write Lithography (EBDW) and Extreme Ultraviolet Lithography (EUV), have enabled the economical and efficient production of nanoscale particles and substrates for scientific research as well as industrial applications[5, 6, 7, 8, 9, 10, 11]. When excited resonantly, the surface plasmons of the metallic nanostructures can generate a strong local electro-magnetic field enhancement, which can induce a large cross-section for surface enhanced spectroscopy studies, such as Surface Enhanced Raman Spectroscopy (SERS) and Surface Enhanced Infrared Absorption (SEIRA).

SERS[12, 13, 14, 15, 16, 17, 18, 19] is a surface sensitive technique which applies the strong electromagnetic field hotspot from the rough surface of metals to produce large enhancement of Raman scattering of adsorbed molecules. Based on specific geometric configuration and surface roughness, a typical SERS enhancement factor can

be as large as 10^{15}. Such hugh enhancement can dramatically increase the detection sensitivity to virtually allow a single molecule to be identified.

SEIRA[20, 21, 22] is the effect where molecules adsorbed on metal island films or particles exhibit a much stronger (10-1000 times) infrared absorption than would be expected from conventional absorption measurements without the metal. The electromagnetic coupling between the incident photon and the metal surface plays an important role in this effect. Due to its relatively weak signal strength, SEIRA has not received as much attention as SERS. However SEIRA has its unique advantages such as working with mid-infrared excitations and being responsive to a very broad energy regime.

Although many of the predecent studies have focused on individual nanoparticles or small nanoparticle clusters (dimer, trimer, etc.) [23, 24, 25], potential applications of nano-plasmonics to promising fields such as Tip-Enhanced Raman Spectroscopy (TERS)[26, 27, 28], negative refractive index metamaterials[29, 30, 31, 32] and sub-wavelength waveguiding [33, 34, 35] require systematic experimental and theoretical investigations on the plasmonic properties of infinitely extended nanostructures, such as the nanoparticle / metallic film system and the one and two dimensional nanoparticle arrays.

Tip-Enhanced Raman Spectroscopy (TERS) has recently been a hot topic for its promising capability of combining scanning probe microscopy such as Atomic Force

Microscopy (AFM) or Scanning Tunneling Microscopy (STM) with SERS. Traditional Raman spectroscopy measurement suffers a lot from weak signals due to the small Raman cross-sections of molecules. Unlike SERS which requires complex fabrication technique to deliberately create roughened metallic surface for local electromagnetic hotspots, TERS utilizes the field concentration around the metal tip of a microscopy close to a smooth metallic film. Compared with SERS, TERS has a similar resolution for molecule detection and is much more flexible since the location of the hotspot can be freely modulated by repositioning the tip.

Metamaterial is another highly promising field in nano-plasmonics. Metamaterials are macroscopic composites having a manmade, three dimensional, periodic cellular architecture designed to produce an optimized combination, not available in nature, of two or more responses to specific excitations. The first metamaterial was developed by W. E. Kock in the late 1940's Metal-lens antenna[36]. In 1999, Pendry demonstrated that left-handed materials, which possess negative permeability and permittivity at the same wavelength regime, can be created from metamaterials with carefully designed geometric properties[37]. Numerous fascinating applications have emerged thereafter, including superlens[38], cloaking devices[39] and agile antennas[40].

Subwavelength waveguiding technique refers to the method that allows transmission of visible light through nanostructures. This technique is crucial in developing future genenerations of optical circuits and super computers. It has been shown[41]

that nanoparticles with different dielectric and magnetic properties are analogous to basic electronic circuit components (resistors, inductors and capacitors) so that nanocircuits can potentially be analyzed and designed classically.

The main theoretical methods applied in this thesis are Plasmon Hybridization (PH) and Finite-Difference Time-Domain (FDTD). Plasmon Hybridization is a quasi-static analytical approximation of the Maxwell's Equations, developed here at Rice University[42, 2]. In the PH method, metal is treated as irrotational, incompressible electron gas on top of uniform, rigid positive background. The plasmons of the interacting system are expressed in terms of the primitive plasmons of the elementary surface modes. Since PH does not include phase retardation effect, our research with PH mainly focuses on quasi-static limit where the size of the particle is at most a quarter of the incident wavelength. The plasmonic interaction in the system is modeled with instantaneous Coulomb potential.

Finite-Difference Time-Domain method is a brute-force "boot-strapping" algorithm in solving Maxwell's Equations in differential forms on an offset Yee cell[43, 44]. Shortly after being introduced by Yee[45], FDTD did not receive much attention due to its difficulty in modeling an infinitely "open" space. This conundrum was successfully solved by Mur in 1981 by introducing the absorbing boundary conditions[46]. Ever since then FDTD has been widely applied in engineering fields such as antenna array design[47, 48], wireless communication[49], biomedical research[50], photonic

crystal studies[51, 52, 53], etc. Recently FDTD has been successfully applied in spectral analysis and electric field enhancement simulations of metallic nanostructures[54, 55].

The combined power of PH and FDTD has led to exciting discoveries in nanoplasmonics [56, 57, 58]. Although fully numerical methods such as FDTD usually lack intuitive physical interpretations, it can be fully compensated by a PH calculation on the same system. With a straightforward eigen-mode analysis from PH, we can understand the dominant plasmonic interactions in complex nanostructures.

This thesis is comprised of the materials from the following publications:

"Optical Properties of Metallic Nanoparticle Arrays for Oblique Excitation using the Multiple Unit Cell Method", F. Le, and P. Nordlander, *Journal of Computational and Theoretical Nanoscience* (Accepted)

"Metallic Nanoparticle Arrays: A Common Substrate for Both Surface-Enhanced Raman Scattering and Surface-Enhanced Infrared Absorption", F. Le, D. Brandl, Y. A. Urzhumov, H. Wang, J. Kundu, N. Halas, J. Aizpurua, and P. Nordlander, *ACS Nano*, **2**, 707-718 (2008)

"Surface Enhanced Infrared Absorption (SEIRA) Spectroscopy Using Infrared Resonant Nanoshell Aggregates Substrates", J. Kundu, F. Le, P. Nordlander, and N. Halas, *Chem. Phys. Lett.*, **452**, 115-119 (2008)

"Plasmonic Interactions between a Metallic Nanoshell and a Thin Metallic Film", F.

Le, N. Z. Lwin, N. Halas, and P. Nordlander, *Phys. Rev. B*, **76**, 165410 (2007)

"Nanorice: A Hybrid Plasmonic Nanostructure", H. Wang, D. Brandl, F. Le, P. Nordlander, and N. Halas, *Nano Letters*, **6**(4), 827-832 (2006)

"Plasmonic Substrates for Surface Enhanced Spectroscopies", F. Le, F. Hao, and P. Nordlander, *SPIE Proceedings*, **6324**, 63240P (2006)

"Plasmon Hybridization in Complex Metallic Nanostructures", P. Nordlander, F. Le, and Y. Wu, *SPIE Proceedings*, **5927**, 59270W (2006)

"Plasmonic Structure and Electromagnetic Field Enhancements in the Metallic Nanoparticle-Film System", P. Nordlander, and F. Le, *Appl. Phys. B*, **84**, 35-41 (2006)

"Plasmons in the Metallic Nanoparticle-Film System as a Tunable Impurity Problem", F. Le, N. Z. Lwin, J. M. Steel, M. Käll, N. Halas, and P. Nordlander, *Nano Letters*, **5**(10), 2009-2013 (2005)

This thesis is organized as follows. In Chapter 2 we study the nanosphere / metallic film system for different film thicknesses and we focus on analyzing the Virtual State (VS). In Chapter 3 we study the tunability in the nanoshell / film system by modulating the aspect ratio of the nanoshell. In Chapter 4 we study the optical properties of 2D hcp array of nanoshells. In Chapter 5 we apply MUC FDTD in simulating the extinction spectra and dispersion relations of periodic nanoparticle arrays under various incident angles. In Chapter 6 we present the main conclusions of the thesis.

Chapter 2
Nanosphere and Metallic Film

2.1 Introduction

In recent years several compelling analogs of quantum systems have been constructed and studied where light takes the place of electrons. Simple periodic electromagnetic lattices, known as photonic crystals, support complex band structures directly analogous to the electronic bands in crystalline solids.[59] Electrons and photons undergo strikingly similar behavior in disordered geometries, where properties of diffusion are modified and a transition from a delocalized to a localized state may be induced.[60, 61] This transition from delocalized to localized behavior has also been seen in 2D surface electromagnetic waves, known as plasmons.[8] Recently we have reported that the plasmon resonances in localized metallic nanostructures may be understood as electromagnetic analogs of simple atoms and molecules, where their resonances mix and hybridize in a rigorous analogy with molecular orbital theory.[2, 62]

2.2 Theory

For metallic nanostructures, the nearby presence of a conducting plane induces frequency shifts in their plasmon resonances, just as it would for simple atoms and molecules,[63, 64] and can affect the already strong coupling between directly adjacent metallic nanoparticles.[65] Here we examine the interaction between the discrete,

localized plasmon of a metallic nanosphere and the continuum of delocalized surface plasmons of a directly adjacent metallic film of finite thickness (Fig. 2.1). Using plasmon hybridization, we show that this geometry is in fact the electromagnetic analog of the standard impurity problem, i.e. the spinless Anderson-Fano model.[66, 67, 68] The standard impurity problem is ubiquitous in condensed matter physics, underlying such important phenomena as chemisorption,[69] charge transfer at surfaces,[70, 71] and the device operation of single electron transistors.[72] Unlike the numerous groups that have studied this problem in the past, focusing primarily on how the particle-substrate separation Z controls the interaction,[73, 74, 75, 76, 77, 78, 79, 80] we show that there are important fundamental aspects of this interaction controlled by varying the film thickness T. For a metallic film of finite thickness, the plasmon density of states and its effective interaction with the discrete nanoparticle plasmons is a thickness-dependent continuous function of energy ranging from zero to the bulk plasmon energy.

In the plasmon hybridization method, the plasmons of the interacting system are expressed in terms of primitive plasmons associated with the elementary surfaces of the system.[2, 42] The primitive plasmons of each nanostructure can be viewed as incompressible deformations of the electron gas of the particle on top of a uniform, rigid background of positive charge. The present study concerns small nanospheres where retardation effects are negligible and where the interaction is modeled using

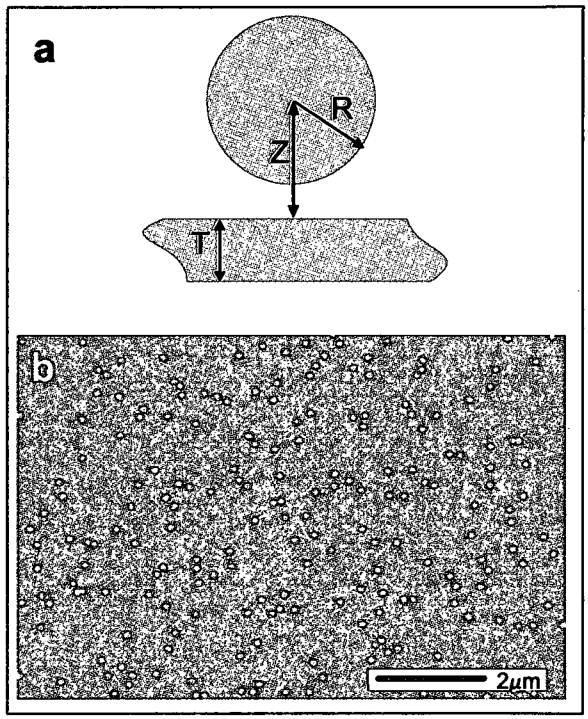

Figure 2.1 Schematic (a) depicting the geometrical parameters of the interacting nanoparticle and film. The interaction is controlled by varying the film thickness, T. R is the nanoparticle radius and Z is the distance between the center of the nanoparticle and the surface of the film. Electron micrograph of a representative experimental sample (b) of a thin Au film on which Au nanoparticles have been dispersed. The film was grown in vacuum by e-beam evaporation onto glass substrates following the deposition of a 1.5 nm Ti adhesion layer. Film thicknesses were established in situ using a calibrated thickness monitor and checked using ellipsometry. A spacer layer was formed by depositing polyvinylpyridine (PVP) from a 1% solution in ethanol for 8 hours. The resulting PVP layer was measured by ellipsometry to be 3.5 0.5 nm, a measurement which may also have had contributions from thickness variations in both the film and the underlying glass substrate. Au nanoparticles of 25 nm and 50 nm dimensions from British Biocell International with a monodispersity of 8% were dispersed on the films.

the instantaneous Coulomb potential.For a nanoparticle close to the surface, $Z_0 \approx R$ and the dominant interaction ranges from $k_{max} = (l + \frac{1}{2})/R$ for a thin film to $k_{max} = l/R$ for a thick film. Thus the interaction is mediated by surface plasmon of wave vectors larger than 1/R and retardation effects in the nanoparticle/film problem can be neglected for small nanospheres. We also neglect non-Drude contributions to the damping of the plasmons.

In the following, we assume a uniform conduction electron density n_0 in the nanosphere and the film. This electron density correspond to a bulk plasmon energy $\omega_B = \sqrt{\frac{4\pi n_0 e^2}{m_e}}$. In the present calculations we will use ω_B=4.6eV. The effect of a background polarizability of the metal is a screening of the surface charges associated with the surface plasmons. This effect can be modeled using a lower conduction electron density. In the application to metallic structures of gold, we therefore use an effective bulk plasmon frequency of 4.6 eV which corresponds to the experimental value of 2.6eV for the dipolar sphere plasmon in vacuum.

The incompressible electron liquid deformations can be expressed in terms of a scalar potential η which in the case of a solid nanosphere outside a thin film takes the form:

$$\eta = \int \frac{d\vec{k}}{(2\pi)^2} \dot{P}_{\vec{k}}(t) e^{i\vec{k}\cdot\vec{\rho}+kz} + \int \frac{d\vec{k}}{(2\pi)^2} \dot{Q}_{\vec{k}}(t) e^{i\vec{k}\cdot\vec{\rho}-k(z+T)} + \sum_{l,m} \sqrt{\frac{1}{lR^{2l+1}}} \dot{S}_{lm}(t) r^l Y_{lm}(\Omega) \tag{2.1}$$

where T is the film thickness and R is the radius of the sphere. The integrals are over

the two-dimensional angular momenta of the surface plasmons and the summation is over the multipolar components of the primitive sphere plasmons. The coordinates of the primitive film plasmons are expressed in cylindrical coordinates with an origin centered on the film surface closest to the nanosphere, on the surface normal through center of the nanosphere. $\vec{\rho} = (\rho, \phi)$ denotes the lateral position along the surface and z is the coordinate perpendicular to the surface. For the sphere plasmons we use spherical coordinates with a polar axis oriented away from the surface. The quantities $P_{\vec{k}}$ and $Q_{\vec{k}}$ are the amplitudes of the primitive plasmons associated with the surfaces of the film and S_{lm} are the amplitudes for the primitive sphere plasmons. Using the above expression for η, the kinetic and potential energy of the primitive plasmons can be expressed in terms of the amplitudes $P_{\vec{k}}$, $Q_{\vec{k}}$ and S_{lm}.[42]

The Lagrangian for the film can be written in a diagonal form by introducing bonding and antibonding combinations of P and Q, $M_{\vec{k}\pm} = \frac{1}{\sqrt{2}}(P_{\vec{k}} \pm Q_{\vec{k}})$ which can be shown to correspond to the plasmonic states of a thin film with energies $\omega_{\vec{k},\pm} = \frac{\omega_B}{\sqrt{2}}\sqrt{1 \mp \exp[-kT]}$. In this representation the Lagrangian for the film takes the form

$$L^{film} = \frac{n_F m_e}{2} \sum_{i=\pm} \int \frac{d\vec{k}}{(2\pi)^2} k(1 - e^{-2kT})[\dot{M}^2_{\vec{k}i} - \omega^2_{\vec{k}i} M^2_{\vec{k}i}] \tag{2.2}$$

The surface plasmons of the film form a continuous band, ranging from zero energy up to the bulk plasmon frequency of the metal. The plasmonic density of states is peaked around the surface plasmon energy $\omega_{sp} = \omega_B/\sqrt{2}$. The plasmonic density of

states depends strongly on film thickness. For infinite thickness, the film plasmons have no dispersion and the plasmonic density of states is a delta function centered on the surface plasmon energy ω_{sp}. For decreasing film thickness, the density of states broadens. The modes $M_{\vec{k}\pm}$ represent the linearly independent non interacting plasmons of a thin film. In the presence of the sphere, they no longer represent the stationary states of the system.

Making use of the azimuthal symmetry of the problem and introducing Fourier transforms of the film plasmon amplitudes as in Ref. [81] the Lagrangian of the combined system can be written $L = \sum_m L^m$, where

$$\begin{aligned} L^m &= \sum_l [\dot{S}_{lm} - \omega_{S,l}^2 S_{lm}^2] \\ &+ \sum_{i=\pm} \int dk [\dot{M}_i^2(k,m) - \omega_{ki}^2 M_i^2(k,m)] - \sum_l \sum_{i=\pm} \int dk S_{lm} M_i(k,m) V_{lk}^m(Z_0) \end{aligned} \quad (2.3)$$

where the interaction term can be evaluated analytically and has the form:

$$V_{lk}^m(Z) = \sqrt{\pi}\omega_B^2 y_l^m \sqrt{lR}\sqrt{1-e^{-2kT}} e^{-kZ} \frac{2}{2l+1} \frac{(-kR)^l}{(l-m)!}, \quad (2.4)$$

This Lagrangian describes localized plasmons interacting with a continuum. With the substitution ω^2 for energy, the secular equation resulting from the Euler-Lagrange equation is equivalent to the determinant obtained when diagonalizing the spinless Anderson model. The primitive plasmon amplitudes S_{lm} and $M_\pm(k,m)$ correspond to the field operators for the discrete and continuum states, and the function $V_{lk}^m(Z_0)$ corresponds to the hopping matrix element in the Anderson model. Since the model

is quadratic, there are no effects of statistics. The interaction V_{lk}^m is a continuous function of k.

The parameter determining the interaction between the localized sphere plasmons and the film plasmons is $\rho(\omega)V_l^2(\omega)$ where ρ is the plasmonic density of states of the film and $V_l(\omega)$ is the interaction term Eq. (A.20). We will refer to ρV^2 as the effective continuum of the film. The effective continuum consists of a lower branch derived from the M_+ film plasmon modes and an upper branch derivied from the M_- plasmon modes. Since the energies of the lower continuum are closer to the discrete sphere plasmons, it is this band that will mediate most of the interaction. In the discussion that follows, we refer strictly to the lower band although the upper band is included in all calculations.

2.3 Results

2.3.1 Plasmon Hybridization

The interaction regimes between the discrete plasmon level of the nanoparticle and the continuum of surface plasmon states of the metallic film are shown schematically in Fig. 2.2. Here three distinct regimes of interaction are depicted. As in the quantum impurity models, the interaction can result both in virtual resonances at energies in the continuum and in localized states at energies outside the continuum, i.e., above or below the band, depending on the continuum parameters. In the thick film case ($T > 2Z_0$), illustrated in Fig. 2.2(a)(left), the effective film continuum lies above

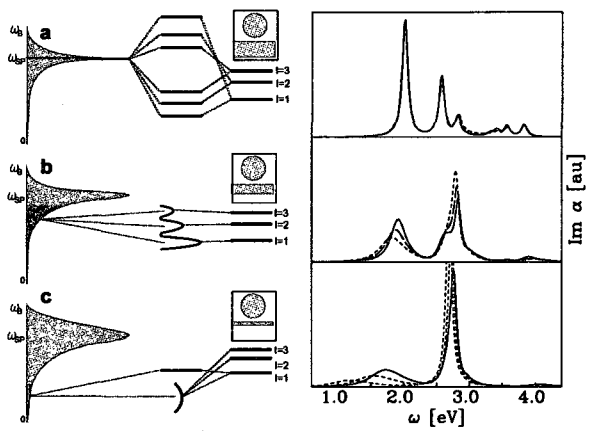

Figure 2.2 The three interaction regimes (a,b,c) for a plasmonic nanoparticle and the surface plasmons of a thin metallic film. For each case, the left panel illustrates the energetics of the interaction regime, while the right panel shows the corresponding calculated dipolar optical absorption spectra for the ($m = 0$) excitation, for various film thicknesses corresponding to this regime. The plasmonic density of states $\rho(\omega)$ is illustrated in light blue, the effective continuum of the film ρV^2 is illustrated in dark blue and the resulting hybridized plasmons are shown in black. (a) left panel: the regime corresponding to the thick film limit, where the effective continuum of the film ρV^2 lies at higher energies than the discrete nanoparticle plasmon. (a) right panel: the spectrum for thick films ($T > 2Z_0$) T=400 (solid), 200 (dashed) and 100 nm (dotted).(b) left panel: the energetics of the intermediate regime, where the nanoparticle plasmon is resonant with the effective continuum ρV^2 of the film. (b) right panel: we show the spectra for films of intermediate thickness ($T \approx Z_0$) , T=25 (solid), 20 (dashed), 16nm (dotted). (c) left panel: the regime of the thin film limit, where the effective continuum of film plasmons ρV^2 lies at lower energies than the nanoparticle plasmon. (c) right panel: the corresponding spectra for thin films ($T < Z_0/2$), T=12 (solid), 8 (dashed), and 4 nm(dotted). The parameters are R=25nm, Z_0=29nm, and ω_B=4.6eV.

the nanosphere plasmon energy. In this case, the effective continuum is extremely narrow and the surface plasmon density of states is highly degenerate. Hybridization between the localized sphere plasmons and the sharp distribution of surface plasmons around ω_{sp} results in strong, low-energy bonding and higher energy anti-bonding states. This is qualitatively similar to the hybridization of a nanosphere outside a semi-infinite surface.[81] For intermediate film thicknesses ($T \approx Z_0$), the nanosphere plasmon energies lie within the effective surface plasmon continuum (Fig. 2.2(b), left). In this case, the interaction results in a broadening of the discrete nanoparticle plasmons. In the thin film regime ($T < Z_0/2$), the effective film continuum lies at lower energies than the discrete plasmons of the nanosphere (Fig. 2.2(c), left). The high energy hybridized plasmon is a localized state above the continuum and remains narrow. It is composed primarily of the discrete localized plasmon resonances but weakly blueshifted due to the interaction with the continuum. The broad low energy feature in the continuum is a virtual resonance in the continuum. It is composed primarily of film plasmons and can be viewed as an incomplete image-like response of the film to the oscillating nanoparticle plasmon. The energy and shape of the virtual state follows the effective interaction ρV^2 with the continuum states. These thin film features contrast markedly with the case of a nanoparticle interacting with a semi-infinite metal, where the plasmon density of states is essentially a delta function at the surface plasmon resonance energy and the hybridization results from image-like

interactions between the nanoparticle and the metal. Furthermore, we can anticipate from this interaction that the energy of this broad low energy plasmon would be strongly controlled by film thickness, and that as the film thickness is reduced, further downshifting the effective continuum of the film plasmons, the virtual state would concurrently shift to lower energies.

In the right panels of Fig. 2.2, we show the calculated dipolar optical absorption spectra for perpendicular ($m = 0$) polarization of the incident wave for different film thickness T. The dipolar optical absorption is equivalent to the spectral function of the discrete $l = 1$ state in the impurity problem. The upper panel (Fig. 2.2(a), right) shows the optical absorption for thick films. The shapes of the curves are qualitatively similar to those of a nanosphere outside a semi-infinite surface.[81] The highly degenerate film plasmons at ω_{sp} mediate an efficient hybridization of the nanosphere plasmons, resulting in several dipole active modes. The three pronounced absorption peaks at 2, 2.5, and 2.8 eV correspond to hybridized states derived from the $l = 1, 2, 3$ sphere plasmons. For the thickest film, the half widths of the plasmon resonances is equal to the damping used when calculating the optical response function, i.e. 0.1 eV. As the film thickness is reduced, the widths of the plasmon resonances are increased slightly. The broadening is strongest for the $l = 3$ resonance. This broadening is caused by the increased interaction with the effective film continuum as illustrated in Fig. 2.2(a), (left). The width of the $l = 2$ and $l = 3$ resonances are more strongly

influenced by T than the $l = 1$ resonance because they overlap more strongly with the continuum.

The middle panel (Fig. 2.2(b), right) shows the optical absorption for intermediate film thicknesses. In this regime the discrete sphere plasmons lie inside the continuum, and the interaction results in broadened plasmon resonances. The hybridization of the sphere plasmons is reduced due to the decrease in plasmonic density of states at $\omega = \omega_{sp}$. This reduction in hybridization reduces the dipole moment of the $l = 2$ and $l = 3$ modes and hence their effective cross section for optical absorption.

The lower panel (Fig. 2.2(c), right) shows the optical absorption in the thin film regime, for a nanosphere on a film with thickness smaller than $Z_0/2$. Here the optical spectra are characterized by two features: a sharp localized state above the continuum and a broad low energy virtual state in the continuum. As the film thickness is further decreased, the effective band ρV^2 shifts to lower energies resulting in a redshift of the low energy virtual state. The localized state above the continuum is essentially composed of the $l = 1$ sphere plasmon. This resonance remains slightly above the energy $l = 1$ sphere plasmon and only exhibit a weak redshift with decreasing film thickness. The virtual state in the continuum is predominantly composed of thin film plasmons and can be viewed physically as an incomplete image response to the nanosphere dipolar plasmon oscillation.

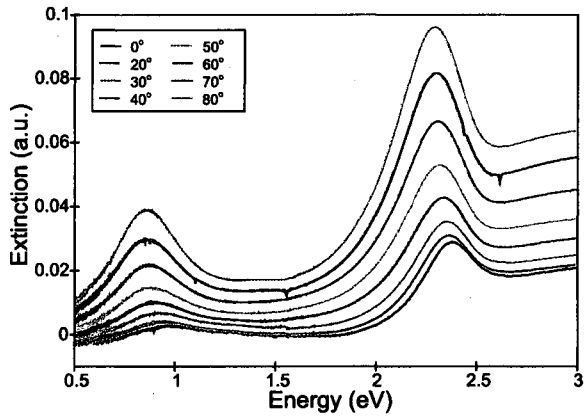

Figure 2.3 UV-Vis extinction spectra of Au nanoparticles with radius of 50nm deposited over conducting film of 4nm thickness with a 3.5±0.5nm spacer layer. Spectra are taken using p-polarized light at different incident angles using a Cary 5000 Spectrometer.

2.3.2 Experimental Measurements

Experimentally, the thin film regime is the regime that can be probed most straightforwardly by performing optical transmission measurements on thin film-nanoparticle samples (Fig. 2.1b). The samples were constructed such that the interparticle spacing was much larger than the nanoparticle diameters, to ensure that interparticle coupling effects would be negligible. Optical transmission spectra of the nanoparticle-thin film system are shown in Fig. 2.3. The spectral features we observe here are qualitatively similar to those previously reported by Okamoto et al.[75] Since the hybridization is polarization dependent, we examine the plasmon response as a function of angle for p-polarized light. This allows us to excite the $m = \pm 1$ coupling case (plasmons oscillating parallel to the film) for light of normal incidence, and the $m = 0$ case (plasmons oriented perpendicular to the film surface) as we approach

90 degree excitation (maximum angle 80 degrees). Here the two plasmon resonances are clearly observed. The high energy resonance corresponding to the localized state above the continuum remains very much unmodified relative to the plasmon resonance one would expect for an isolated Au nanoparticle.[82] The low energy feature around 0.9 eV is the virtual state in the continuum. The spectra are in qualitative agreement with theory (Fig. 2.2). The decreased amplitude of the higher energy peak in the experimental spectra results from damping caused by interband transitions in Au, not accounted for in the present theory.

As the incident angle is increased, both $m = 0$ and $m = 1$ plasmons are excited and the resulting spectrum is an angle-dependent superposition of the response for the two polarizations. The spectral weight of the low energy feature increases with increasing incident angle. This is in agreement with our theoretical predictions which show that the intensity of the virtual state is stronger for the $m = 0$ case than for the $m = 1$ case. The weak redshift of the virtual state with increasing angle is caused by the anisotropy of the sphere-film interaction: the virtual state for $m = 0$ has lower energy than for $m = 1$.

The virtual state can be tuned to lower energies by decreasing the film thickness, which lowers the energies of the effective film plasmon continuum. We see this very clearly in our experimental measurements. In Fig. 2.4a, four spectra for the thin film regime taken at 80 degree incident angle such that the predominantly m=0 case was

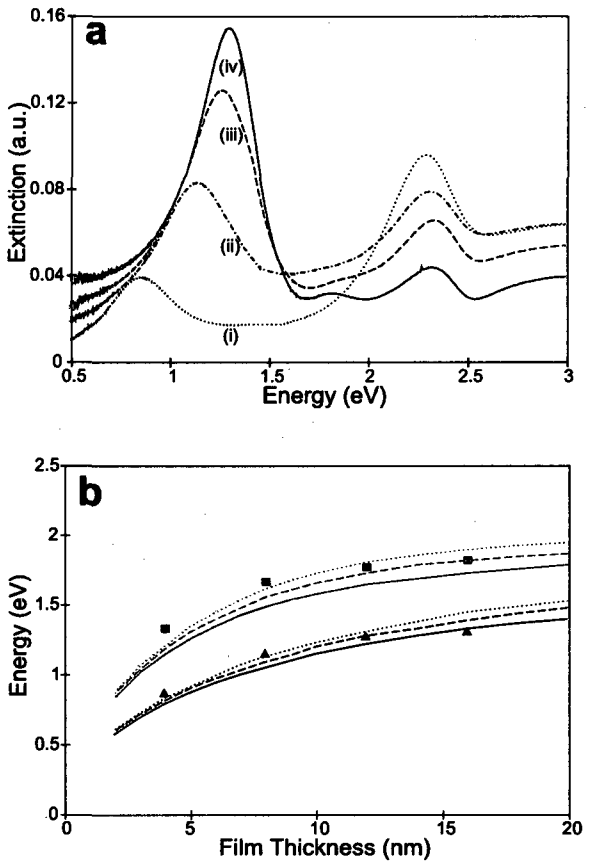

Figure 2.4 (a) Extinction spectra of Au nanoparticles with radius of 50nm deposited over conducting film with thickness (i) 4nm; (ii) 8nm; (iii) 12nm; (iv) 16nm. (B) Energy of the virtual plasmon state as a function of film thickness for Au nanospheres deposited on top of Au films. The blue curves refer to nanospheres of radius R=25nm and the red curves are for R=50nm. The symbols are the experimentally observed energies for extinction maximum of the virtual state. The continuous lines are the results from the plasmon hybridization method using an effective bulk plasmon energy of 4.6eV. The dotted lines are for Z-R=5nm, the dashed are for Z-R=4nm and the solid line is for Z-R=3nm.

probed. These four spectra show the progression of the virtual state as a function of film thickness. In these data we see both a strong downshift of the virtual state as the film thickness is reduced, and that the higher energy, localized plasmon is essentially unperturbed. In Fig. 2.4b, we show that the energy of the virtual state redshifts with decreasing film thickness for nanospheres of radii 25 and 50nm. This trend is modeled quite well for the sample geometry using an effective bulk plasmon of 4.6eV, corresponding to a plasmon resonance for the isolated nanosphere of 2.6eV. Although the dielectric function of the spacer layer is neglected in this simple modeling, the energy downshift of this feature is followed quite well by this approach. The effects of dielectric screening on this calculation are yet to be fully examined.

2.4 Summary and Discussions

In summary, we have shown that the plasmonic properties of the nanoparticle/metallic film problem can be described as a classical impurity problem, i.e. the spinless Anderson model. We show that the nature of the interaction is essentially controlled by film thickness. In the thin film limit the interaction results in localized plasmon levels with essentially the same plasmon energies as an individual nanosphere and a low energy broad virtual resonance consisting of film plasmons. The analogy with the classical impurity model may provide further insight and understanding of the plasmonic properties of film structures such as tip-film junctions in scanning probe microscopies, and nanoparticle and nanometric hole arrays in films.

Chapter 3
Nanoshell and Metallic Film

3.1 Introduction

The optical properties of macroscopic and mesoscopic metallic structures are of considerable importance in both fundamental and applied science.[7, 83, 84] Applications such as chemical and biosensing, for example, are beginning to exploit surface enhanced Raman spectroscopy (SERS), where the excitations of nanoparticle plasmons in a nanostructure-based substrate can provide large enhancements of the local electromagnetic field and drastically increase the Raman cross section of adsorbed molecules. [12, 13, 14, 15, 16, 17, 19] Other applications include the development of ultrasmall waveguides depending upon subwavelength plasmonic structures, as potential optical interconnects in computer chips.[33, 34, 35, 85, 86, 87]

The energies of the plasmon resonances of nanoparticles depend sensitively on their composition and shape.[5, 88, 89, 10, 90, 11, 91, 92, 93] In nanoparticle aggregates such as dimers, the plasmon resonances depend strongly on interparticle separations.[94, 95, 96, 97, 54, 98, 99] For nanoparticles near semi-infinite metallic surfaces, the plasmon resonances have been shown to depend strongly on nanoparticle-surface separation.[73, 100, 78, 101, 81] The plasmon resonances have been found to depend strongly on interparticle separations in nanoparticle arrays of various dimensionalities.[102, 65, 103, 104, 105]

In the previous chapter we showed that the metallic nanosphere/film system represents a highly tunable plasmonic nanostructure, where the plasmon energies can depend sensitively on the ratio of nanoparticle radius to the thickness of the film. We showed that the plasmonic interactions in the system are described by a model analogous to the standard impurity models such as the spinless Anderson-Fano Model. The discrete and localized nanoparticle plasmons interact with the continuum of delocalized film plasmons, an interaction that can result in localized states, resonances and virtual states (VS) in the continuum. These concepts were originally introduced to describe the nature of the electronic states resulting from the interaction of a discrete impurity level with a continuum.[66] The VS is a state composed primarily of continuum states with only a small admixture of the discrete state, in contrast to the localized state, which is primarily composed of the discrete state. Both the localized and VS were identified experimentally, and the tunability of the VS was observed in a series of systematic experiments, where metallic nanospheres were deposited, along with a constant-thickness spacer layer, onto metallic films of decreasing thickness. In a subsequent paper, the Finite Difference Time Domain (FDTD) methods were used to study the electromagnetic properties of the VS. It was shown that the VS is characterized by a strong coupling between the nanosphere and the film, with large field enhancements induced in the junction between the nanosphere and the nearest film surface.

In this chapter, we generalize our method to include the effects of dielectric backgrounds and a realistic description of the metals and apply our method to a metallic nanoshell outside a thin metallic film. In contrast to a solid nanosphere, the nanoshell is in itself a highly tunable metallic nanoparticle consisting of a thin metallic shell around a spherical dielectric core.[5] The discrete plasmon resonances of a nanoshell depend strongly on its aspect ratio x, the ratio of inner shell radius a to outer shell radius b, and can be tuned across the visible and infrared region of the spectrum. Thus the nanoshell/film system can exhibit a higher tunability than that of the nanosphere on a film. For a low aspect ratio nanoshell where the discrete nanoshell plasmon resonances lie above the effective film continuum (the regime inside the film plasmonic band that strongly interacts with the nanoparticle) we find a localized plasmon resonance above the continuum and a broad VS in the continuum. For a nanoshell of intermediate aspect ratio, where the discrete nanoshell resonances lie within the film continuum, the finite probability of plasmon hopping into the film results in a broadening of the plasmon resonances. For a nanoshell of large aspect ratio, the virtual state is further tuned into the low energy part of the film plasmon continuum. Our calculated optical spectra compare well with experimental measurements. Using FDTD we investigate the electric field enhancements induced by excitations of the plasmon modes and show that these enhancements can be very large. Our study shows that the nanoshell/thin film system exhibits greater tunability and larger electromagnetic

field enhancements than the nanosphere/film system.

3.2 Theory

The physical situation being modeled is that of the discrete plasmons of a finite metallic nanoshell interacting with a continuum of delocalized surface plasmons of a directly adjacent metallic film of finite thickness. In the PH method,[42, 106] the plasmons are modeled as incompressible deformations of the electron gas of the particle on top of a uniform, rigid background of positive charge. The kinetic energy of the time-dependent deformations is balanced by a force resulting from the potential energy of the spill-out charges at the surfaces of the nanostructure. The potential energy is calculated using the instantaneous Coulomb potential. Since the method is nonretarded, it applies rigorously only to nanostructures of dimensions much smaller than the wavelength of incident light. This condition is satisfied in the present problem because the interactions between the film and nanoparticle are mediated by nonretarded film plasmons of wavelengths comparable to the size of the nanoparticle.[81]

To describe the plasmons of the interacting system, the charge deformations are expanded in a complete set of primitive plasmons associated with the elementary surfaces of the system.[42] The primitive plasmons interact and hybridize with each other, forming bonding and antibonding plasmons in direct analogy with molecular orbital theory. The method provides an intuitive understanding of how the geometri-

cal and structural properties of a nanostructure influence its plasmon resonances, and agrees very well with simulations performed using computational approaches such as the fully retarded FDTD method.[106]

In the following, we assume a uniform conduction electron density n_S in the nanoshell and n_F in the film. These densities will enter the formalism in terms of the corresponding bulk plasmon energies $\omega_{B,S} = \sqrt{4\pi e^2 n_S/m_e}$ and $\omega_{B,F} = \sqrt{4\pi e^2 n_F/m_e}$. The inner radius of the nanoshell has a radius a and the outer radius is b. The aspect ratio of the nanoshell is $x = a/b$. The film is assumed to have a thickness T and the separation between the center of the nanoshell and the upper surface of the film is denoted Z_0. The width of the junction between the nanoshell and the upper film surface is $H = Z_0 - b$. These geometric variables are sketched in Figure 3.1. We will also include the effect of dielectric backgrounds, such as the dielectric background permittivity of the metals, ϵ_M, representing the polarizability of the metallic ions. The resulting dielectric function of the metal has a Drude form $\epsilon(\omega) = \epsilon_M(\omega) - \omega_B^2/\omega^2$. When the optical absorption of the structure is calculated, we add a damping term $i\delta(\omega)$ to the frequency. This damping describes the energy dissipation in the system and results in a complex dielectric function of the form $\epsilon(\omega) = \epsilon_M(\omega) - \omega_B^2/(\omega + i\delta(\omega))^2$. The real parameters $\epsilon_M(\omega)$ and $\delta(\omega)$ can be fit straightforwardly to measured real and imaginary parts of the dielectric function of Au[107] to provide an accurate description of the dielectric properties of Au over all frequencies of interest. The specific

dielectric backgrounds that will be included are illustrated in Fig. 3.1.

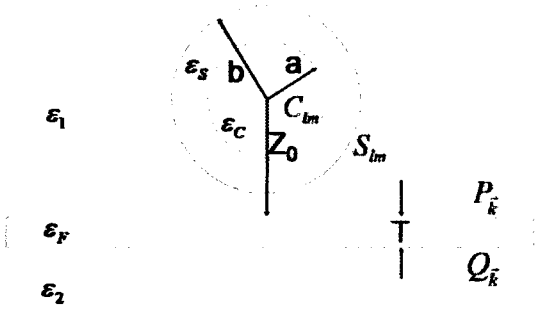

Figure 3.1 The geometry of the nanoshell-film system. Geometric variables a, b, T and Z_0 represent the inner and outer radii of the nanoshell, the metallic film thickness and the shell-film separation respectively. C_{lm}, S_{lm}, $P_{\vec{k}}$ and $Q_{\vec{k}}$ are the amplitudes of the primitive nanoshell cavity, sphere plasmons and the film plasmons on both sides. ϵ_C, ϵ_S, ϵ_1, ϵ_2 and ϵ_F are the background dielectric constants of the nanoshell core, the nanoshell metallic layer, the embedding media above and below the film and the metallic film respectively. The effects of varying the dielectric background constants are investigated in Figure 3.4.

The deformation field associated with the plasmons can be obtained from a scalar potential η,[42] which for the present system takes the form,

$$\begin{aligned}\eta &= \int \frac{d\vec{k}}{(2\pi)^2}\dot{P}_{\vec{k}}(t)e^{i\vec{k}\cdot\vec{\rho}+kz} + \int \frac{d\vec{k}}{(2\pi)^2}\dot{Q}_{\vec{k}}(t)e^{i\vec{k}\cdot\vec{\rho}-k(z+T)} \\ &+ \sum_{l,m}\left[\sqrt{\frac{1}{lb^{2l+1}}}\dot{S}_{lm}(t)r^l + \sqrt{\frac{a^{2l+1}}{l+1}}\dot{C}_{lm}(t)r^{-l-1}\right] \\ &\times Y_{lm}(\Omega) \qquad (3.1)\end{aligned}$$

The radial coordinate r is defined in a spherical coordinate system centered on the nanoshell and with a polar axis oriented perpendicularly to the upper film surface. The quantities Y_{lm} are the spherical harmonics. $P_{\vec{k}}$ and $Q_{\vec{k}}$ are the amplitudes of

the primitive film surface plasmons associated with the surfaces closest and furthest from the nanoshell. The quantities S_{lm} and C_{lm} are the amplitudes for the primitive sphere and cavity plasmons of the nanoshell. The first two integrals are over the 2D wave vectors describing the primitive film plasmons and the two summations are over the discrete multipolar plasmonic levels of the nanoshell.

In Appendix (Derivation of the Lagrangian) it is shown how one can exploit the cylindrical symmetry of the problem and transform the primitive plasmon basis into a more convenient form. The resulting Lagrangian is diagonal in azimuthal index m and can be written,

$$\begin{aligned} L^m &= \sum_{l,i=\pm} [\dot{N}^2_{lm,i} - \omega^2_{l,i}(x) N^2_{lm,i}] \\ &+ \sum_{j=\pm} \int dk [\dot{M}^2_j(k,m) - \omega^2_{k,j}(T) M^2_j(k,m)] \\ &- \sum_l \sum_{i=\pm,j=\pm} \int dk N_{lm,i} M_j(k,m) V^m_{lk,i,j}(Z_0,T). \end{aligned} \tag{3.2}$$

In this expression, $N_{lm,\pm}$ represent the tunable discrete bonding (-) and antibonding (+) plasmon modes of an isolated nanoshell of aspect ratio x with energies $\omega_{l,\pm}(x)$ given by Eq. (A.1). The amplitudes $M_\pm(k,m)$ describe the continuum of bonding (-) and antibonding (+) plasmons of an isolated metallic film with energies $\omega_{k,\pm}(T)$ given by Eq. (A.8). With the present use of cylindrical symmetry, plasmons polarized perpendicularly to the surface are described by $m = 0$ and plasmons polarized parallel

to the surface correspond to $m = \pm 1$.

This Lagrangian represents a classical impurity problem, i.e., the interaction between discrete localized states with a continuum of delocalized states. The interaction $V^m_{lk,i,j}(Z_0)$ corresponds to the hopping element. The parameter describing the nature of the interaction is the effective continuum $\rho V_l^2(\omega)$ where ρ is the density of states of the bare film plasmon continuum and ω is the energy (frequency). Our previous study showed that the spectral structure of the VS is similar to that of the effective continuum. In chemical terms, the VS can be viewed as a "bonding" many-particle state resulting from the interaction of a finite continuum with a higher energy discrete state. In physical terms, it can be described as an incomplete image response to an oscillating dipole. In the present chapter we will investigate thin metallic films where the effective continuum forms a broad band in the low energy region of the film plasmon density of states. In our discussion we will focus on the dipolar $l = 1$ couplings although higher multipolar couplings are present and induce a hybridization of the primitive nanoshell plasmon modes.

Since the plasmon energies of a nanoshell are dependent on its aspect ratio x, we can tune the discrete nanoshell plasmons to arbitrary positions within the effective continuum. In Figure 3.2, we illustrate schematically how the interaction changes as the aspect ratio of the nanoshell is increased. The light blue areas to the left show the plasmonic density of states of the individual film, and the dark blue areas

denote the lower-energy band of the effective continuum $\rho(\omega)V_{l=1}^2(\omega)$, representing the film plasmons that couple strongly to the discrete, dipolar "bonding" plasmon of the nanoshell. The effective continuum is peaked an energy around $\omega_{k=3/2R,-}(T)$, and extends continuously down to zero energy. The higher-energy branch of the effective continuum only interacts weakly with the bonding plasmons of the nanoshell and is therefore not highlighted in the figure. On the right, we show the location of the discrete dipolar plasmon energies of the nanoshell. Panel (a) shows the interaction for a thick nanoshell. The nanoshell plasmon lies above the effective continuum (as in the case of a nanosphere outside a thin film). The interaction results in a localized state above the continuum and a VS in the continuum. Panel (b) shows the interaction for a nanoshell of intermediate aspect ratio. Here the energy of the discrete nanoshell plasmon falls within the effective continuum and becomes a broadened resonance. In panel (c) we show the interaction for a thin nanoshell where the VS gets pushed further to lower energies.

We discretize the continuum and introduce a vector notation which is described in Appendix (Discretization and Vector notation). The Lagrangian can be represented in a quadratic form

$$L^m = \frac{1}{2}\dot{\vec{X}}^T\hat{T}_X\dot{\vec{X}} - \frac{1}{2}\vec{X}^T\hat{V}_X\vec{X}, \tag{3.3}$$

where $\vec{X}$ is a vector representing the primitive plasmon amplitudes and $\hat{T}_X$ and $\hat{V}_X$ are matrices representing the kinetic and potential energy of the primitive plasmon

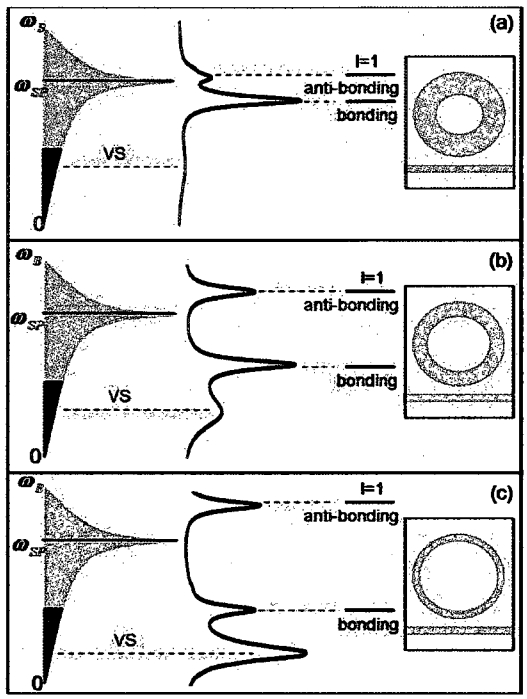

Figure 3.2 (Color online) Schematic illustration of the nanoshell-metallic film interaction as the aspect ratio ($x = a/b$) of the nanoshell increases (a-c). The light blue area to the left represents the plasmonic density of states of the film $\rho(\omega)$. The dark blue area represents the effective continuum $\rho V_{l=1}^2(\omega)$. The right part illustrates the geometry and energy of the discrete nanoshell plasmon. The black curves depict the absorption spectrum resulting from the plasmonic interaction between the nanoshell and the film.

in the $\vec{X}$ basis. The superscript T denotes the transpose of a vector or matrix. In Appendix (Effects of dielectric background) we show how the effects of dielectric backgrounds can be included in the formalism. Background dielectrics have no effect on the kinetic energy of the primitive plasmons but modify the potential energy matrix $\hat{V}_X$, Eq. (C.2).

The application of the Euler-Lagrange equations results in a linear equation system

from which the plasmon energies of the interacting system are obtained as eigenvalues,

$$\omega^2(\hat{T}_X + \hat{T}_X^T) - (\hat{V}_X + \hat{V}_X^T) = 0. \tag{3.4}$$

3.3 Results

This section contains three subsections. In the first subsection we present the results obtained from the PH approach. Then we focus on the aspect-ratio dependence of the nanoshell and show how it increases the tunability of the VS. We also investigate the effects of background dielectrics on the plasmonic structure of the system. In the second subsection we compare the PH results with results from FDTD simulations. We also present an investigation of the local electromagnetic field enhancements in the junction between the nanoshell and the film. In these two theory subsections we use smaller nanoshells of varying inner radii but with a fixed outer radius of b=50 nm. We use a small nanoshell to minimize the computational effort and to enable a more direct comparison between PH and FDTD. In the third subsection, we present the experimentally measured extinction spectra of the system and compare with theoretical calculations. The gold nanoshell studied and modeled here has an inner radius of a=60 nm and an outer radius of b=70 nm.

3.3.1 Plasmon hybridization

In Figure 3.3, we show the optical absorption spectra calculated for perpendicular polarization ($m = 0$) for the systems that correspond to the situations depicted in

Figure 3.2. We only consider optical absorption by the nanoshell and neglect optical absorption in the film. This figure illustrates the shift to lower energies of the discrete nanoshell plasmon with increasing aspect ratio $x = a/b$. In each panel, the solid curve is the spectrum of the nanoshell-film system and the dashed line is for the individual nanoshell only. The spectra in the top panel are dominated by the localized state around 2.4 eV. A broad VS is observed on the low energy side of the localized state. The small shoulder around 2.5 eV is the antibonding dipolar nanoshell plasmon, which is strongly damped and broadened due to interband transitions. For small aspect ratios, the splitting of the bonding and antibonding nanoshell plasmons is very small.[42] The middle panel shows a situation where the discrete bonding nanoshell resonance is shifted into resonance with the effective continuum. The result is a formation of a resonance which is broadened relative to the discrete nanoshell resonance. The antibonding resonance remains as a broad shoulder around 2.5 eV. In the lower panel where the discrete nanoshell state is shifted further down into the continuum, a VS appears at even lower energy and the intensity of the VS gets significantly stronger than the localized state. The reversal of the relative intensities of the localized peak at higher energy and the VS at lower energy from panel (b) to panel (c) does not mean a higher admixture of the discrete state into the VS. A careful analysis of the eigenvectors of the lowest-energy peak shows that the film states still dominate the mode, and thus it remains a VS. (Further evidence for this

will be presented in Fig. 3.5(c) where the electromagnetic field enhancements for the low energy peak display the strong coupling between particle and film which is characteristic of a VS.) For a thinner film, the VS would be shifted to lower energies. The figure clearly demonstrates the additional tunability that is introduced by absorbing a nanoshell rather than a nanosphere on the film.

In Figure 3.4, we investigate the effect of dielectric backgrounds on the absorption spectrum of the nanoshell/film system. Panel (a) shows the spectra for an Au film in vacuum. A VS appears around 1.5 eV and the localized state around 2.2 eV. The antibonding peak is strongly damped due to interband transitions and appears as a small shoulder around 2.5 eV. Panel (b) shows the effect when $\epsilon_2 = 5$ while $\epsilon_1 = 1$. The spectrum is similar to Panel (a), with a small redshift of the VS as well as the localized bonding state of the nanoshell, but the intensity of the VS is reduced. This is because ϵ_2 redshifts the film continuum but does not influence the discrete nanoshell plasmon. The increased energy separation between the discrete state and the continuum reduces the magnitude of the interaction, resulting in less hybridization. Panel (c) shows the optical absorption when $\epsilon_1 = 5$ while $\epsilon_2 = 1$. Both the VS and the localized bonding nanoshell plasmon redshift significantly. The antibonding nanoshell plasmon is not affected, since it is composed primarily of cavity plasmons which do not depend on the dielectric properties of the media outside the shell. The redshift of the VS is consistent with that of both the discrete bonding

nanoshell plasmon and the film plasmon continuum, redshifted by ϵ_1. The $l = 2$ localized nanoshell state also appears at around 1.9 eV. Panel (d) shows the result when $\epsilon_1 = \epsilon_2 = 5$. Compared with Panel (c) we find a slight redshift of both the localized and VS and a strong decrease in the intensity of the VS analogous to the decrease of the VS intensity observed between panels (a) and (b). The effects of the two background dielectrics ϵ_1 or ϵ_2 can be summarized in the following manner: increasing ϵ_1 significantly redshifts both the localized and VS, whereas increasing ϵ_2 only weakly redshifts the localized state but reduces the intensity of the VS.

3.3.2 Finite difference time domain simulations

To further visualize the local electromagnetic interaction in the nanoshell and metallic film system, we have numerically calculated the extinction spectra of a nanoshell on a thin slab using the fully retarded FDTD method,[43, 55, 54] Our current FDTD code does not allow us to simulate a finite nanoparticle interacting with an infinite film, so the system is modeled as a nanoparticle near a finite slab. For a finite slab, the plasmons do not form a continuum, but rather,they appear as standing waves with discrete frequencies. The resulting VS are therefore only sampled at the discrete slab plasmon energies resulting in a VS composed of discrete slab states rather than a smooth resonance structure containing film plasmons of all wavevectors within the effective continuum. The slab we use has sufficient lateral extent that the VS is sampled in sufficient detail. FDTD calculations cannot be performed efficiently

for an arbitrary description of dielectric function data.[43] For this reason in this subsection we use a Drude fit of the Au dielectric data, $\epsilon(\omega) = \epsilon_M - \omega_B^2/\omega(\omega + i\delta)$ with $\epsilon_M = 9.5$, $\omega_B = 8.94\ eV$, and $\delta = 0.05eV$ for both the FDTD and PH calculations. This parameterization provides an accurate fit of the dielectric data for Au bulk metal above 500 nm.[55, 54]

In Figure 3.5 the extinction spectra from FDTD with the absorption spectra from PH are compared, for nanoshells of several different aspect ratios interacting with the slab. To avoid overestimating the electromagnetic field enhancements in the junction between the particle and the film we include a thin PVP spacer layer between the nanoparticle and the film in the FDTD simulations. Such a spacer layer would need to be included in any experimental realization of a nanoparticle-film junction (and is used in the experiments and simulations on a larger nanoshell in subsection IIIC). This spacer layer has no effect on the calculated extinction spectra. The size of the nanoshell is small (radius 50 nm), so that the extinction spectra (containing both absorption and scattering terms) should be mainly determined by absorption.[108] We observe that the strengths and distribution of the discrete VS peaks calculated by FDTD fit well within the broad resonance obtained from the PH calculation, indicating good agreement between these two theoretical approaches. The slight redshift of the FDTD spectra is due to retardation effects. To the right are the electric local field enhancements calculated for the specific peak labeled by the arrow in the spec-

tra. Enhancement is defined here as the absolute value of the electromagnetic field at a specific point divided by the absolute value of the incident field. For simplicity, we show the enhancement only for the lowest energy discrete peak in the VS. The calculated electric field enhancements are large and show that the VS represents a strong coupling between the nanoshell and the film. As the aspect ratio of the nanoshell increases, the electric field enhancement increases from 121 to 244. Compared to the field enhancement factors obtained previously for the nanosphere/film system, we find that the thin nanoshell and film interaction produces a VS of lower energy and larger local field enhancements. This shows that the nanoshell/film system is a more suitable substrate for surface enhanced spectroscopy studies than the nanosphere/film structure.

The electric field enhancements for excitation of the $m = 1$ VS (not shown) are much smaller than for $m = 0$. The magnitude is similar to the enhancements of an individual nanoshell but the location is in the junction between the nanoshell and the film.

3.3.3 Experimental measurements

In this section, we show experimental results for the extinction spectra of the nanoshell/film system. The fabrication details are similar to those reported in our previous study of the nanosphere/film structure. In Figure 3.6 an SEM image of a representative sample is shown. This image shows that the number density of

nanoshells over the film is low. The majority of nanoshells scatter sparsely onto the film but many form aggregates and are therefore also sampled in the experiment. The theoretical calculations presented in this section refer to the highly idealized situation of an isolated nanoshell on a uniform thin film. We do not try to model local variations of film thickness, nonuniform nanoshell-film separations, or the effect of nanoshell-nanoshell interactions. Instead, we focus more on trends such as the effect of polarization, film thickness and dielectric overlayers rather than attempting a quantitative explanation of experimental data. The incident laser beam comes from beneath the film and the extinction spectra are determined by subtracting the transmitted light from the incident light. The incidence angle is defined as the angle between the wave vector of the incident light and the surface normal of the film.

Extinction spectra for each sample were taken using p-polarized light with the incident angle varied from 0 to 80 degrees at 10 degree intervals. In Figure 3.7 the raw extinction spectra are shown for one of the samples of nanoshell/metallic film structures as a function of incident angle. The Au film thickness is 12 nm. An incidence angle of zero degrees refers to light polarized parallel to the surface (normal incidence) that can interact with $m = 1$ plasmons. Varying the angle from normal incidence in TM, or p-polarization, the largest angle of incidence that can be achieved in the experiment is 80 degrees. This near grazing incidence angle results in light polarized 96% ($\sin^2 80^o$) perpendicular and 4% ($\cos^2 80^o$) parallel to the film. We refer

to this geometry as perpendicular polarization; it predominantly couples to $m = 0$ plasmons although a small fraction of $m = 1$ modes are excited at this angle. At normal incidence (0^o), the spectrum is characterized by two peaks, a peak at 1.8 eV and a broad shoulder around 1.3 eV. These features correspond to the localized state above the continuum and a $m = 1$ VS in the continuum, respectively. As the angle is increased, the intensity of the $m = 1$ VS decreases and a new feature appears around 0.8 eV. This feature is the $m = 0$ VS. The energy of the localized state at 1.8 eV does not depend on polarization, since it is essentially composed of a pure "bonding" nanoshell dipolar plasmon. The discontinuity around 1.6 eV is an experimental artifact caused by a change of spectrometer grating at 800 nm. (In the following spectra this discontinuity is removed by a linear interpolation procedure.) The nature of the weak feature around 0.65 eV which appears most clearly at normal incidence is unknown. Possible origins include a nanoshell dimer or aggregate resonance which for normal incidence would be redshifted to below 1 eV or a Fabry-Perot resonance generated by the glass substrate.

In order to experimentally investigate the effect of the dielectric embedding medium surrounding the nanoshell (ϵ_1) on the extinction spectra, a thick layer (nominally 10 microns) of polyvinylpyridine (PVP), fully embedding the layer of dispersed nanoshells, was spin-coated onto the substrates. In the following we will refer to the samples where PVP is present only as a spacer layer between the film and nanoshell, as air-

ambient samples.

In Figure 3.8 the extinction spectra for perpendicular polarization ($m = 0$) for air-ambient and PVP-coated samples are shown. Each measurement is performed for four different film thicknesses, $T = 4, 8, 12, 16$ nm, respectively. For the air-ambient samples (panel a), the peak around 1.7 eV is the localized bonding nanoshell dipolar resonance, which is independent of film thickness. The VS shifts to lower energies from around 0.9 eV for $T = 16$ nm to nominally 0.7 eV for $T = 4$ nm. Panel (b) shows the effects of the PVP overcoating. Both the localized and the VS are redshifted compared to the air-ambient samples. The localized state appears at an energy around 1.5 eV, and the VS redshifts from around 0.75 eV for $T = 16$ nm to 0.54 eV for $T = 4$ nm. The peak intensities in the PVP-coated samples are strongly suppressed relative to the air-ambient samples due to the dielectric screening. In the inset of Panel (b) we show a close-up of the low-energy part of the $T = 4$ nm curve where the VS appears as a shoulder around 0.54 eV.

In Figure 3.9 we compare the energy of the VS determined from the experimental spectra with those obtained from PH as a function of film thicknesses for different surrounding media ϵ_1. The important trend of a decreasing energy of the VS with reduced film thickness is reproduced very well. The best fit is obtained for $\epsilon_1 = 4$, which is larger than the experimental value of $\epsilon_1 = 2.25$ for bulk PVP. Possible reasons for the discrepancy may be local variations of the dielectric environment of

the nanostructures, or the neglect of retardation effects, which for the present system of a nanoshell of radius 70 nm can be as large as 0.15 eV (estimated from Mie Theory for a spherical nanoshell).

In Figure 3.10 the energy of the $m = 1$ VS obtained from the measurements is compared to the results from the PH method. As for $m = 0$ polarization the energy of the VS state shifts to lower energies with decreasing film thickness. Interestingly, though the overall interaction energy for $m = 1$ polarization is weaker than that for $m = 0$ polarization, we find that the effect of over-coating with PVP is much larger than for $m = 0$ polarization. The reason is that the energy of the virtual state depends on the difference in energy between the discrete nanoshell state and the effective continuum. On the air-ambient sample for $m = 0$ polarization, the surface charges associated with the discrete nanoshell plasmon are located in the junction between the nanoparticle and the film and on top of the nanoshell. The PVP spacer layer thus both screens the nanoshell mode and the bare thin film plasmons. This screening results in a redshift of both the nanoshell mode and the effective film continuum which enables a more efficient interaction as discussed in Fig. 3.4. For $m = 1$ polarization, where the effective dipole lies parallel to the film, the effect of the PVP coating is different. On the air-ambient sample, only the film plasmons are screened, since the surface charges associated with the discrete nanoshell plasmon are located at a distance b from the spacer layer. The effect of PVP-coating is an efficient

screening and a redshifting of the discrete nanoshell plasmon mode. The redshift brings the mode closer to the effective film continuum resulting in a stronger redshift of the VS.

3.4 Summary and Discussions

In this chapter we have shown that the metallic nanoshell/film system represents a highly tunable plasmonic structure with strong resonances in the infrared region of the spectrum, accompanied by large local electric field enhancements. This easily fabricated geometry has properties that are of fundamental physical interest, as an experimental physics testbed where the parameters of the spinless Anderson model can be varied controllably. The "antenna-over-conducting-plane" paradigm for this system lends it naturally to a variety of applications in subwavelength plasmon optics. This geometry provides a wavelength-specific method for the selective coupling of light to or from freely propagating light waves and surface plasmons, of likely importance for plasmon-based devices. The large local fields in the particle-film junction provide an important model for tip-sample junctions in scanning microscopies such as NSOM, enabling the design of both tip and substrate for scanning tip-enhanced Raman spectroscopy, known as TERS. In our theoretical analysis of this system we have shown how the plasmon hybridization method can be extended to include electrostatic screening from background dielectrics. We have shown that in the limit of a thin metallic film, the interaction between the discrete nanoshell plasmons and the

continuum of delocalized film plasmons can result in a low energy virtual state. The electromagnetic field enhancements induced by excitation of the virtual states are of a similar magnitude to those obtained in the junction of a nanoparticle dimer. The energy of the virtual state can be tuned by changing the aspect ratio of the nanoshell and/or by changing the thickness of the film. Further studies including the application of periodic boundary FDTD for modeling a continuous film, and thus the VS, more accurately, and single particle optical measurements, are currently in progress.

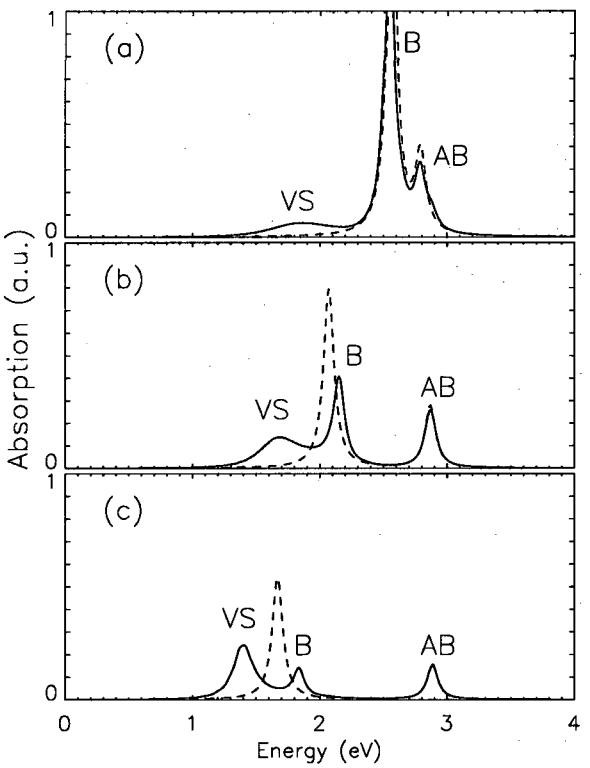

Figure 3.3 Optical absorption spectra of the Au nanoshell-thin film system in geometries corresponding to Figure 3.2. The solid lines are dipolar optical absorption as a function of frequency for a nanoshell of outer radius $b = 50$ nm and different inner radii $a = 20$ nm (panel a), $a = 40$ nm (panel b), and $a = 45$ nm (panel c). The center of the nanoshell is at a position $Z_0 = 53$ nm outside a metallic film of thickness $T = 12$ nm. The gold metal is modeled using Johnson-Christy data,[107] and $\epsilon_C = 2.04$ (SiO_2), $\epsilon_1 = 1$ (air) and $\epsilon_2 = 2.25$ (glass). The dotted lines are the absorption spectra for the individual nanoshells. The peaks labeled "VS" are the virtual states. The peaks labeled "B" and "AB" are the discrete dipolar bonding and anti-bonding nanoshell peaks, respectively. The antibonding peaks are strongly damped and broadened due to interband transitions.

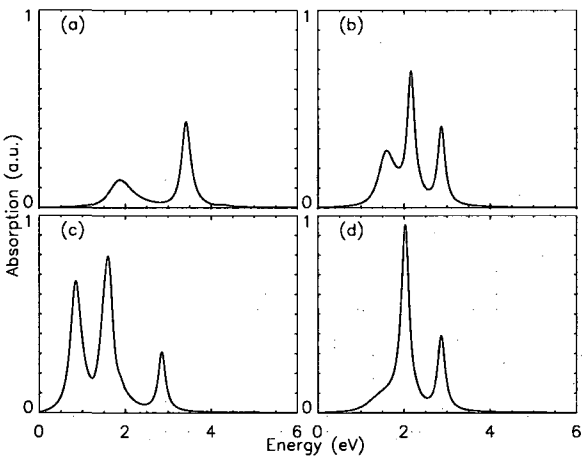

Figure 3.4 Effect of the background dielectric on the optical absorption of a nanoshell near a metallic film for perpendicular polarization $m = 0$. The nanoshell has $a = 40$ nm, $b = 50$ nm and $Z_0 = 53$ nm. The film thickness is $T = 8$ nm. Panel (a) shows the spectra for the film in vacuum. Panel (b) is the spectra for $\epsilon_1 = 1$ and $\epsilon_2 = 5$. Panel (c) is for $\epsilon_1 = 5$ and $\epsilon_2 = 1$. Panel (d) is for $\epsilon_1 = \epsilon_2 = 5$.

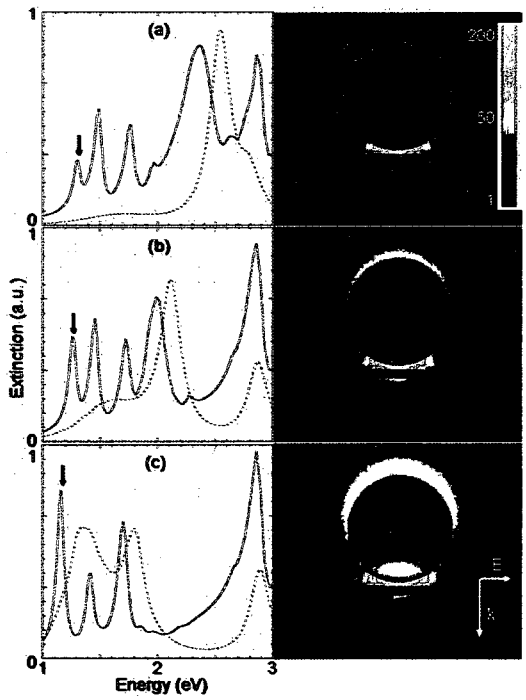

Figure 3.5 (Color online) Extinction spectra (left panels) and local electric field enhancements (right panels) calculated by FDTD for the gold nanoshell/slab system for perpendicular polarization $m = 0$. The slab has a thickness $T = 8$ nm and lateral dimensions 300x300 nm. It is covered by a PVP spacer layer ($\epsilon = 2.25$) of thickness 3 nm and placed on a glass substrate ($\epsilon_2 = 2.25$) of thickness 100 nm. The nanoshell has an outer radius $b = 50$ nm and a silica core ($\epsilon_C = 2.04$). The inner radius $a = 20$ nm (a), $a = 40$ nm (b), and $a = 45$ nm (c). The dotted lines are the absorption spectra calculated using the PH method. The arrows indicate the energies for which the electric field enhancements were calculated. The maximum field enhancement factor in each structure is 120.8, 177.2 and 244.3 for Panel (a), (b) and (c), respectively.

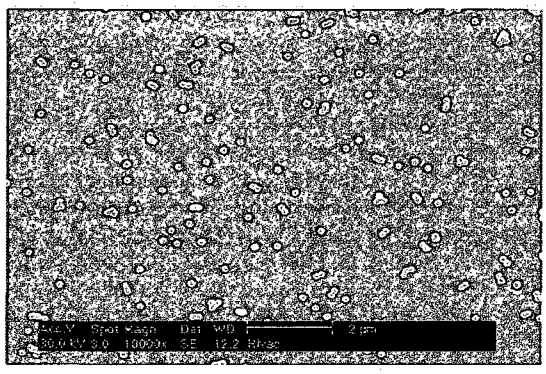

Figure 3.6 SEM image of a representative sample of a thin Au layer on which Au nanoshells have been dispersed. The Au film thickness is 4 nm and the nanoshell has a 60 nm radius core made from SiO_2 and a shell thickness of 10 nm. The Au film is thermally evaporated onto a clean glass slide at base pressure of 10^{-6} torr. A thin Ti film with 1.5 nm thickness is used as an adhesion layer between gold film and glass substrate. A spacer layer of (3.5 ± 0.5) nm is formed by depositing polyvinylpyridine (PVP) from a 1 percent ethanol solution for 8 hours.

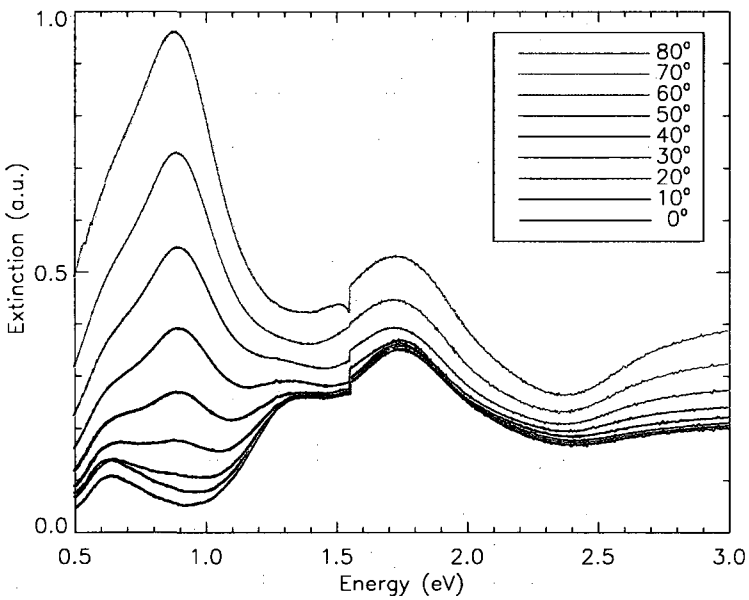

Figure 3.7 (Color online) Experimental extinction spectra of the nanoshell/film system with film thickness of 12 nm. The Spectra are taken using p-polarized light at varying incident angles.

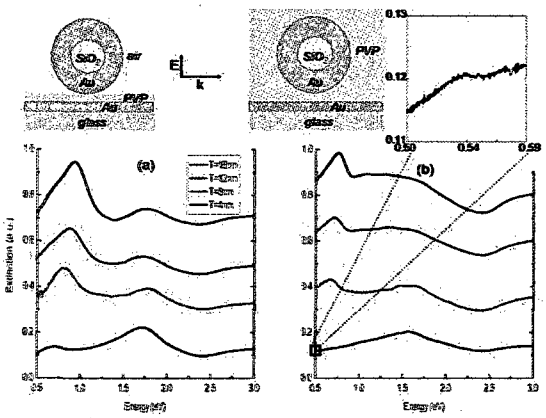

Figure 3.8 (Color online) Extinction spectra for perpendicular polarization $m = 0$ measured for air-ambient (a) and PVP-coated samples (b). In each panel the measurement is performed for 4 different film thicknesses, T=4, 8, 12, 16 nm, respectively. The inset in Panel (b) is the magnified low-energy part of the $T = 4$ nm curve for identifying the VS.

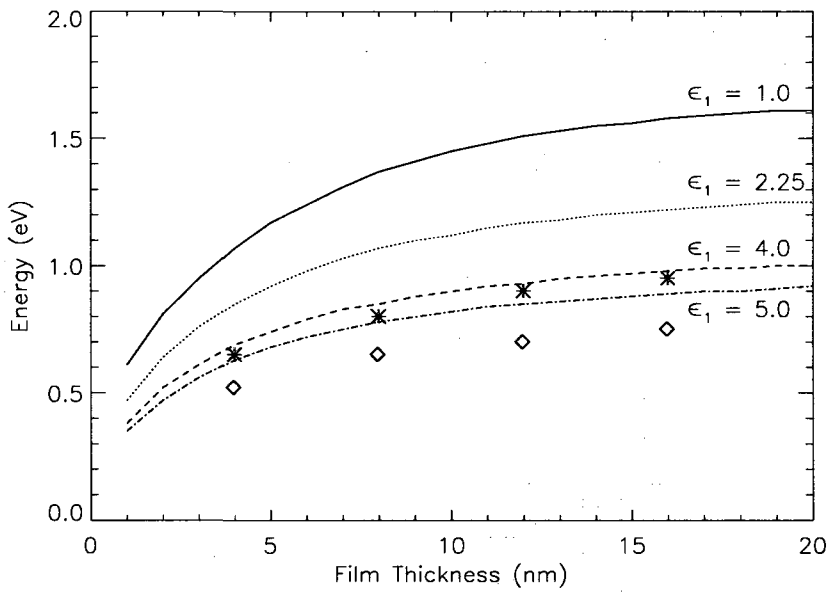

Figure 3.9 (Color online) Comparison of experimentally obtained energies of the $m = 0$ VS with the results from PH as a function of film thickness for different dielectric constants of the embedding medium ϵ_1. The curves are the theoretical calculations with ϵ_1 increasing from 1.0 to 5.0. The blue and red symbols are the experimental measurements for regular and PVP over-coated samples, respectively.

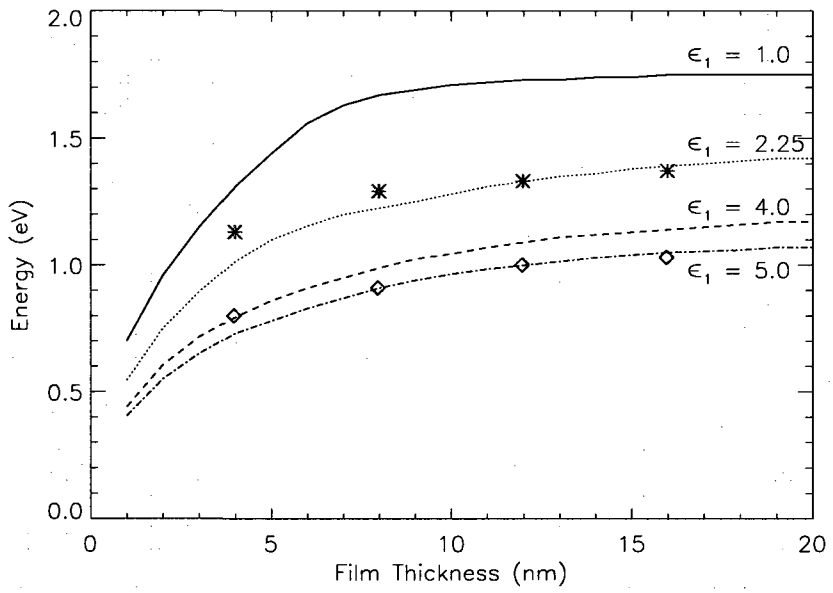

Figure 3.10 (Color online) Comparison of experimentally obtained energies of the $m = 1$ VS with the results from PH as a function of film thickness for different dielectric constants of the embedding medium ϵ_1. The lines an the symbols refer to the same structures as in Figure 3.9.

Chapter 4
Two Dimensional Hexagonal Arrays of Nanoshells

4.1 Introduction

An important application in the emerging field of plasmonics is the development of substrates capable of providing hotspots for Surface Enhanced Spectroscopies (SES).[109, 17, 110, 111] The resonant excitation of plasmons in metallic nanostructures can provide large electromagnetic field enhancements on the surfaces of the constituent metals.[112, 113, 114, 90] These field enhancements can provide a drastic increase of the detected spectroscopic signals. The most widely used SES is Surface Enhanced Raman Scattering (SERS), where the electromagnetic enhancement factor is proportional to the fourth power of the field incident on the molecule.[115, 116, 117, 118] Recently there has been a resurgence of interest in another type of SES, Surface Enhanced Infrared Absorption (SEIRA).[21, 119, 120, 121, 122] Although the electromagnetic enhancement effect in SEIRA is only proportional to the square of the electromagnetic field enhancements, SEIRA is likely to play an important role in the field of chemical and biological sensing because it probes dipole active vibrational modes and thus provides a complementary vibrational analysis of an analyte.

The major reason why SEIRA has received so much less attention than SERS is the difficulty in fabricating nanostructures with tunable plasmon resonances in the infrared (IR) region of the spectrum. The maximum electromagnetic enhancement

in a plasmonic nanostructure occurs for resonant excitations of the plasmons. The plasmon resonances of metallic nanoparticles are strongly dependent on structure and composition.[123, 89, 124, 10, 125, 106, 31] This tunability has been very important in the field of SERS where a variety of plasmonic nanostructures with plasmon resonances overlapping simple laser sources in the visible range have been developed.[19]

In a recent publication[126] it was shown that a two dimensional (2D) hexagonal close-packed (HCP) array of nanoshells can provide significant enhancements to both SERS and SEIRA. The analysis of the SEIRA signals of paramercaptonaniline (pMA) molecules deposited on these arrays suggested enhancement factors between 10^3 to 10^5. Such large values indicate that the dominant enhancement mechanism is electromagnetic rather than chemical. The surprising discovery in this experiment is thus that the same substrate can provide electromagnetic enhancements both in the Near Infrared (NIR) and the Mid Infrared (MIR) region of the spectrum. The extinction spectra of the arrays were found to be characterized by two features, a relatively sharp resonance in the NIR and a very broad, continuum-like resonance in the MIR. While strong electromagnetic field enhancements are expected for excitations of sharp plasmon resonances and can be understood simply as the resonant pumping of a harmonic oscillator (the plasmon), it is not immediately clear what physical mechanism underlies the enhancements associated with the excitation of an overdamped oscillator such as the MIR structure. The purpose of the present chapter

is to elucidate and understand this phenomenon.

In this chapter we analyze the optical and electromagnetic properties of 2D HCP nanoshell arrays on substrates using a variety of computational and analytical techniques. We show that the NIR resonance in the 2D HCP nanoshell arrays are formed by interactions of the quadrupolar resonances of the individual nanoshells in a manner similar to how a d-band is formed from the atomic d-orbitals in a transition metal. The hybridized NIR mode is only weakly redshifted from the quadrupolar nanoshell plasmon because of the weak interparticle coupling of quadrupolar modes. The broad MIR resonance is a hybridized mode originating from the dipolar plasmon resonances of the individual nanoshells, and the strong redshift of the MIR resonance compared to that of NIR resonance is due to the much stronger interparticle interactions for dipoles. The strong broadening of the dipolar resonance is caused by radiative damping. The large field enhancements induced within the MIR resonance are caused by the lightning rod effect. For long wavelengths, the metals act as perfect conductors and expel the electric field from the interior of the metals. This screening squeezes the electric field into the junctions between the nanoshells, resulting in large field intensities. This effect can be described semi-analytically for arrays of arbitrarily shaped nanoparticles using an electrostatic analysis, exploiting the fact that metals at low frequencies behave almost like perfect conductors. The result shows a universal inverse linear relation between the maximum electric field enhancement and the

lattice constant, a parameter that is independent of the shape of the particle. To describe the relevance of the field enhancements for SEIRA, we introduce the concept of hotspot volume. The hotspot volume is defined as the volume within which the electric field enhancements are larger than half of the maximum field enhancement. We show that this quantity depends strongly on the shape of the particles.

4.2 Optical Properties of two dimensional HCP Nanoshell arrays

4.2.1 Experimental spectra

Figure 4.1a shows an SEM image of a typical array sample fabricated using a technique described in a previous publication.[126] The geometry of the nanoshells is $(R_1, R_2) = (152, 172)$ nm, where R_1 and R_2 are the inner and outer radius of the nanoshell, respectively. The separation between adjacent nanoshells is d=8 nm, determined by the thickness of the double spacer layer Cetyl-trimethylammonium bromide (CTAB) molecule in the junction. In Fig. 4.1b we show the extinction spectrum of the array and that of an individual nanoshell of the same size. For the individual nanoshell, the dipolar peak is around 900 nm and the quadrupolar peak is around 700 nm. The shoulder at 2500 nm is a spectral feature which most likely is caused by the presence of nanoshell dimers and larger multiparticle structures on the surface. Although the array spectrum is cut-off at 3000 nm due to the wavelength limit of the spectrometer, we clearly observe the short wavelength part of a broad

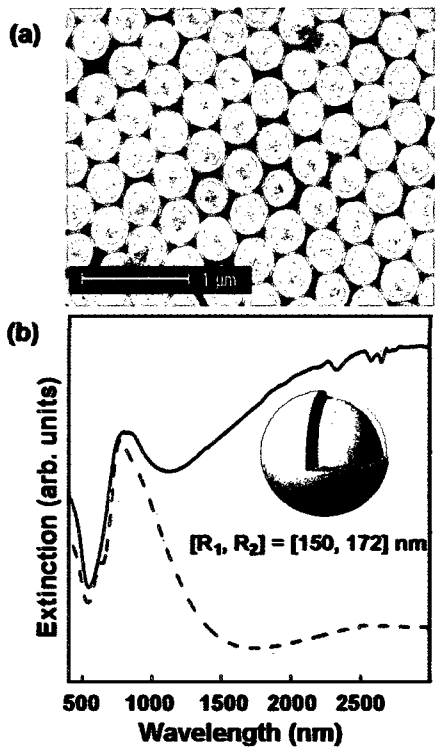

Figure 4.1 SEM image and extinction spectra of a typical HCP Au nanoshell array sample. Panel (a) shows an SEM image of the sample. The inner radius of the nanoshells is 150 ± 12 nm and the gold shell thickness is 22 ± 1 nm. The separation d between adjacent nanoshells is around 8 nm. Panel (b) shows the normal incidence extinction spectrum of the array (solid) and that of an isolated nanoshell with the same size (dashed).

resonance which as will be demonstrated below, extends well into the MIR. Since the resonance is leveling off at 3000 nm we will refer to this feature as a 3000 nm MIR resonance.

4.2.2 Finite Difference Time Domain Simulation

In order to model the HCP nanoshell array, we use the FDTD method with Periodic Boundary Conditions (PBC).[127] The implementation of PBC is straightforward

for light incident on the array at normal incidence. To describe the optical response of gold we use a Drude dielectric function with parameters fitted to experimental data.[55]. We are able to computationally model rectangular unit cells with sizes of around 500 nm. Thus, in principle we can include a substrate with a thickness of a few hundred nanometers. For normal incidence, the major effect of the substrate is a minor 50-150 nm redshift of the spectral features of the array. In addition, for short wavelengths, the spectra displays thickness dependent modulations of the extinction spectrum caused by Fabry-Perot resonances in the substrate. Since the experiments are performed on glass substrates with a thickness of a few millimeters, such Fabry-Perot modulations will not occur. To avoid these artifacts we will neglect the glass substrate in the calculations presented below.

In Fig. 4.2 we show the calculated FDTD-PBC spectra and local electric field enhancements for the HCP nanoshell array studied in Fig. 4.1. Panel (a) shows the extinction, scattering, and absorption. The calculated extinction spectrum shows a narrow resonance at an energy of around 750 nm and very broad feature beginning around 1000 nm and extending far into MIR well beyond the graph cut-off at 3000 nm. Figure 4.2a also shows that the low-energy (long wavelength) broad feature in the extinction spectrum is dominated by scattering. The reason is that in the low-energy limit the gold metal acts as a perfect conductor and excludes all electromagnetic fields, limiting absorption. In panels (b) and (c) we show the local electromagnetic

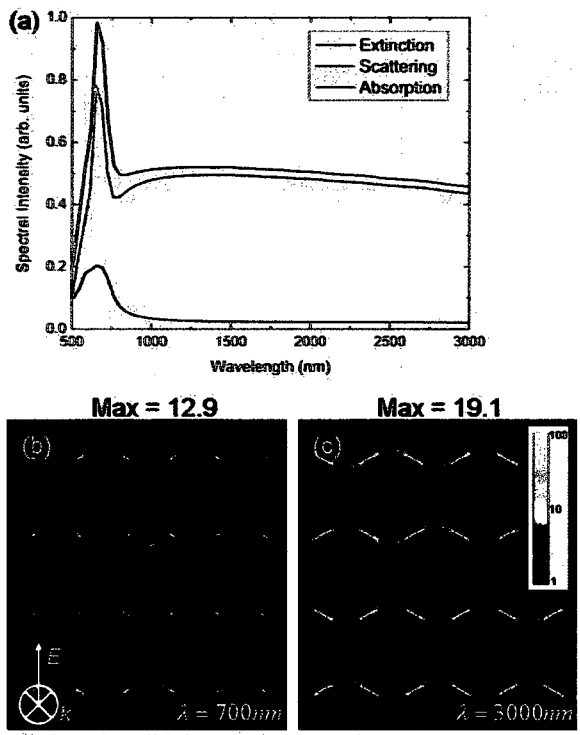

Figure 4.2 FDTD simulation results for an HCP Au nanoshell array. The geometry of the nanoshell is (R_1, R_2)=(150,172) nm, the separation is d=8 nm and the grid size is 2 nm. The periodic unit cell is composed of four half-nanoshells. Panel (a) show the extinction (black), scattering (red), and absorption (blue). Panels (b) and (c) shows the local electromagnetic field enhancements at wavelengths of 700 nm and 3000 nm, respectively.

field enhancement induced at λ=700 nm and at λ=3000 nm. The field enhancement is defined as the ratio of the electric field amplitude at a given position to the field value when the nanostructure is absent. Panel (b) shows relatively small local field hot spots between neighboring nanoshells (maximum field enhancement=12.9) and non-zero enhancement factors inside each nanoshell. Panel (c) shows much larger hot spots between adjacent nanoshells with a maximum field enhancement factor 19.1.

The spatial location of the hotspots for these two wavelengths are identical.

Although both the energy and lineshape of the high energy resonances of the calculated spectra in Fig. 4.2 agree nicely with the experiments in Fig. 4.1, the low-energy (long wavelength) features look slightly different. The experimental spectrum shows a feature which appear to be centered at 3000 nm while FDTD shows a broad band-like structure above 1000 nm. To further investigate this discrepancy we have systematically investigated how the structural parameters of the array influence the resonances in the extinction spectrum. Varying the array separation, d, from 6 nm to 500 nm results in a blueshift and narrowing of broad the low-energy (long wavelength) continuum and ultimately changes the array spectrum into an individual nanoshell spectrum. We were never able to reproduce a strong extinction maximum observed experimentally at 3000 nm. We also investigated the effects of including the dielectric screening mediated by the CTAB layers around each nanoshell. This screening has negligible effect on the spectra but changes the maximum field enhancement factors by 5-10%. As described above we also performed calculations including the glass substrate but again, the low-energy (long wavelength) feature remains a broad structureless continuum. In short, the low-energy feature of the array spectrum shown in Fig. 4.1 cannot be reproduced by modeling the HCP nanoshell array as a perfectly periodic structure.

The microscopic reason for the strong broadening of the MIR resonance in the

array spectrum in Fig. 4.2 is superradiance, i.e. the collective enhancement of the dipolar radiation from an ensemble of interacting coherently oscillating dipoles within a volume of spatial extent smaller than the wavelength of the incident light.[128].

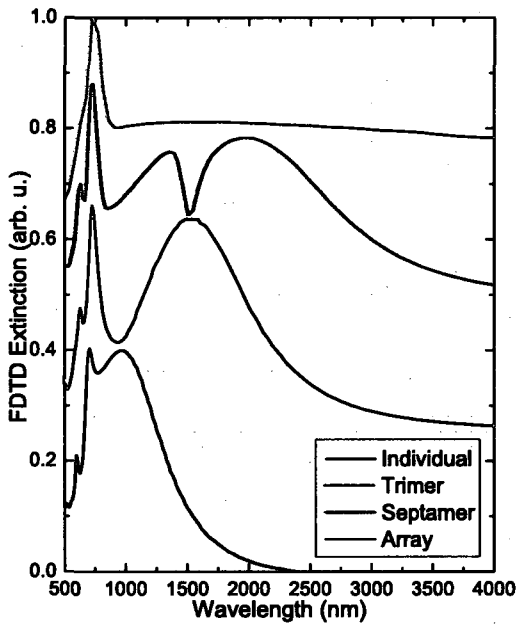

Figure 4.3 FDTD extinction spectra of an individual nanoshell (black), a nanoshell trimer (red), a nanoshell septamer (blue), and a HCP nanoshell array (green). The geometry of the nanoshells is (R_1, R_2)=(150,172) nm, and the separation is d=8 nm. The quadrupolar modes of these structures are all located around 700 nm. The dipolar peaks show a strong redshift because of the increasing number of neighboring nanoshells.

In order to provide more insight into the microscopic nature of the plasmons in the HCP nanoshell arrays we have calculated the extinction spectra for an individual nanoshell, a symmetric nanoshell trimer, and a symmetric nanoshell septamer (one nanoshell in the center and six nanoshells symmetrically distributed around it in the

same plane). In Fig. 4.3 we compare the normalized extinction spectra of these four systems. The finite structures were modeled using the same interparticle spacings as in the array. A simple analysis using Mie theory for the individual nanoshells shows a dipolar resonance around 1000 nm, a quadrupolar around 750 nm, and a weak octupolar resonance around 600 nm. In all four spectra the sharp peaks at 750 nm overlap perfectly. Therefore we can conclude that they originate from the quadrupolar plasmon resonances of the individual nanoshells. The reason for the very weak shift of the quadrupolar resonance with increased coordination is the very weak interaction and hybridization of quadrupolar modes in adjacent nanoparticles.[56] The low-energy (long wavelength) resonances in Fig. 4.3, on the other hand, follow a clear trend of redshifting and broadening with increasing coordination. The individual dipolar nanoshell resonance at 1000 nm shifts to 1500 nm for a nanoshell trimer, and to 2000 nm for the lowest energy nanoshell septamer resonance. The lineshape of the septamer spectrum is characterized by a broad peak centered at 2000 nm with a much narrower, asymmetric dip in the extinction spectrum located around 1500 nm. The asymmetric lineshape of the septamer spectrum is an interference between a narrow (subradiant) and a broad (superradiant) plasmon modes producing a Fano type profile similar to what was recently discussed in a study of multilayer plasmonic wires.[129].

The interference between the two modes in the septamer spectrum is clearly il-

lustrated in Fig. 4.4 where we show the electromagnetic field enhancements for wavelengths around the dip. For the subradiant mode on the blue side of the dip, the largest fields occur in the junctions within the six particles surrounding the center particle. For the superradiant mode, the largest fields are induced between the center particle and the surrounding particles. At the dip, both modes are excited.

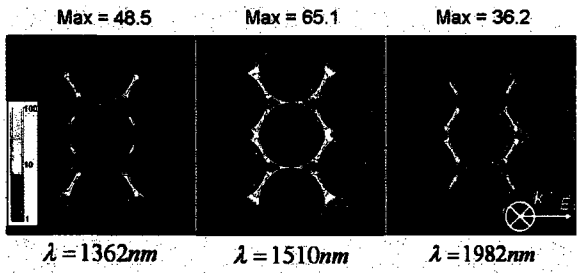

Figure 4.4 FDTD calculations of the electromagnetic field enhancements for the symmetric septamer in Fig. 4.3 at wavelengths 1362 nm, 1510 nm, and 1982 nm.

To further understand the septamer spectra, we have performed extensive FDTD calculations of the optical spectra of the structures discussed in Fig. 4.3, scaling down all dimensions by a common factor ranging from a 1.1 to 8, thus continuously reducing the effects of retardation. In the electrostatic limit, such a scale transformation would leave the optical spectra invariant.

In Fig. 4.5 we show the FDTD extinction spectra for a scaling factor of 8, thus setting the overall dimensions of the nanoshells to 21.5 nm and their separation to 1 nm, and the spectra calculated using the electrostatic Plasmon Hybridization (PH) method[2, 42] for the structures discussed in Fig. 4.3. The quadrupolar resonances

can clearly be seen in the spectra for the trimer, septamer, and the array, as a shoulder and peaks just below 1000 nm. The dipolar resonances of the individual nanoshell, nanoshell trimer, nanoshell septamer and the HCP nanoshell array appear at 1000 nm, 1330 nm, 1300 nm and 2070 nm, respectively. The energies of these modes are blueshifted compared to the larger structures in Fig. 4.3 due to weaker retardation. Since retardation effects always cause a redshift of dipolar resonances, Fig. 4.5a suggests that the location of the strongly damped dipolar resonance in the real HCP nanoshell array should be positioned at a wavelength significantly larger than 2070 nm.

A comparison of the FDTD for the scaled-down structures and the PH spectra in Fig. 4.5 shows very good agreement. The various plasmon modes show up at very similar wavelengths. Since the optical absorption in the PH method is proportional to the square of the dipole moment of the plasmon mode while the FDTD calculation also includes the coupling to higher multipoles, the relative peak intensities in PH and FDTD spectra can be different. For this reason, the quadrupolar modes do not show up in the PH spectra of the individual nanoshell but are clearly visible in the larger structures due to the hybridization of quadrupolar and dipolar plasmon on adjacent nanoparticles. The slight blueshift of the PH spectra compared to the FDTD spectra is due to the complete neglect of retardation in the PH method. The most noticeable differences between the PH and FDTD spectra is the width of the array resonance.

In the PH method, the width of the resonance originates entirely from the imaginary part of the dielectric function. In the FDTD calculation, radiative damping will also contribute.

It is interesting and significant that an electrostatic approach such as the PH method can reproduce the peak positions of an infinite periodic system. The reason for this is that the interactions between plasmons on different nanoparticles decreases rapidly with nanoparticle separation. The plasmon energies are thus determined by the local structure of the array. This local region includes nearest and next nearest neighbors. Therefore, if the size of the local region is much smaller than the wavelength of the incident light, the energies of the plasmon modes can be described using an electrostatic approach.

The spectrum for the small septamer in Fig. 4.5a does not display a Fano resonance. A careful analysis of the septamer spectra for different scaling factors show that the the superradiant mode redshifts much faster than the subradiant mode with decreasing scaling factor. For scaling factors smaller than 2, the energies of the two modes are similar and the subradiant mode appear as an asymmetric dip in the spectra. For smaller systems (scaling factors larger than 2), the energy of the energy for the subradiant mode is lower than the superradiant mode and the subradiant mode appears as a positive peak on the red side of the superradiant peak. The PH method provides for a simple group theoretical analysis of the microscopic nature of the plas-

mon modes in a multi-particle aggregate.[56, 130] The point group of the septamer is D_{6h}. In the inset of Fig. 4.5b, we show the energies and irreducible representations of the five lowest energy plasmon modes of the septamer. The sub and superradiant modes belong to the E_{1u} irreducible representation. In the superradiant mode the nanoshell in the center of the septamer has in phase plasmonic oscillations with the six other peripheral nanoshells, therefore inducing a strong radiative damping and a broad peak in the spectrum. In the subradiant mode, the plasmons in the central nanoshell oscillates oppositely with the plasmons of the peripheral nanoshells so that the radiative damping is strongly suppressed. The higher energy superradiant mode has a large dipole moment while the subradiant mode has no net dipole moment. The subradiant mode can therefore only be excited through its quadrupoles and thus when the size of the system becomes comparable to wavelength of the incident light.

We are now in a position to qualitatively explain the difference between the experimental spectra in Fig. 4.1 and the FDTD spectra in Fig. 4.2. The FDTD calculation with its assumption of a perfectly periodic array structure overestimates the radiative damping. A closer look at the SEM image of the HCP array in Fig. 4.1 reveals that the 2D order is not perfect. Some of the nanoshells appear to have a slightly smaller diameter, and some are slightly moved out of position. Such defects can localize the plasmon modes and introduce inhomogeneous broadening. However, any such deviation from perfect periodicity will also break the coherence of the collective dipolar

plasmon mode and can lead to the destruction of the superradiance.[131] For dipoles oscillating out of phase, the radiative damping can become smaller than the radiative damping of an individual dipole which leads to subradiance. From the perspective of coherence, due to the small disorder, the substrate can probably best be described as consisting of independent finite domains within which coherence is maintained. These optical coherence effects only influence the damping of the plasmon resonance and not their energies which are determined by local properties, i.e., the hybridization of individual nanoparticle plasmons on adjacent nanoparticles. The fact that the calculated trimer and septamer spectra in Fig. 4.3 look much more similar to the experimental spectrum than the calculated array spectra supports this hypothesis. However, even the septamer dipolar resonance is considerably narrower than the experimental MIR resonance indicating that the size of the coherent domains must be larger than seven nanoparticles.

In the next section we investigate the nature of the electromagnetic field enhancements in this type of arrays in the visible (Fig. 4.2b) and in the MIR (Fig. 4.2c).

4.3 Investigation on Quasi-static Electric Field Enhancements

In Fig. 4.2 we showed that significant electric field enhancements were induced at the same locations (in the junctions) of the HCP nanoshell array for two very different wavelengths, a NIR resonance of relevance for SERS and a MIR resonance of relevance for SEIRA. As discussed in the introduction, this is a finding of consider-

able importance in sensing applications since it allows the use of two complementary vibrational spectroscopies for the detection of the same analyte at the same spot on the same substrate. In this section we will further analyze the physical mechanisms underlying these enhancements.

In Fig. 4.6 we show the calculated maximum electric field enhancements in the 2D HCP nanoshell array as a function of the wavelength of the incident light. Further investigation shows that the maximum field enhancement factor continues to grow until it saturates at a value of around 40 beyond 20 microns. The peak in the field enhancement around 750 nm is due to the resonant excitation of the NIR quadrupolar plasmon. This mode is only weakly damped which allows for an efficient pumping of the quadrupolar oscillator. The electromagnetic field enhancements associated with this mode therefore has a wavelength dependence similar to the far field extinction spectrum. In contrast, the large field enhancements for the largest wavelengths can be understood as a electrostatic "Lightning Rod" effect.[132, 133] The slow monotonous increase of the maximum field enhancement between 2000 nm and 20 micron can be understood simply as the response of an overdamped dipolar harmonic oscillator. Only for very slow perturbations, will the oscillator adjust adiabatically to the applied force. The screening associated with the lightning rod effect does not correspond to excitations of plasmons and will therefore not show up in the far field excitation spectrum.

The relevance of the "lightning rod" effect for the understanding of the large field enhancements in nanoparticle dimers was recently discussed by Käll and coworkers.[134] The physical origin of the "Lightning rod" effect is metallic screening. For a perfect metal, no electric field penetrates inside the material. The metal becomes equipotential and all potential drops must occur in the junctions between the metals. Indeed, the electric field enhancement plot in Fig. 4.2c shows this effect already at 3 microns, with the electric field almost perfectly expelled from the metallic shells. The reason for the efficient screening of metals at low frequencies is that the real part of the dielectric function becomes large and negative. The expulsion of the electric field from the interior of the nanoparticles gives rise to the intense field enhancements in the junctions between the metals. This phenomenon provides yet another simple way of understanding the slow monotonous increase of the maximum field enhancement in Fig. 4.6. As the wavelength is increased and the dielectric permittivity becomes more and more negative, the electric field are gradually expelled from the metallic shells with a resulting increase in the field strength in the junctions.

Our finding of large electric field enhancements in metallic structures at long wavelengths in nanoparticle arrays is not limited to nanoshells. Our results would apply equally well to finite aggregates of arbitrarily shaped nanoparticles as long as the wavelength of the incident light is in the mid to far infrared, thus, resulting in a extremely versatile system to perform highly efficient SEIRA spectroscopy indepen-

dently of the structural constitution of the array unit cell.

In the original work on the relevance of the lightning rod effect for SERS on individual nanoparticles, it was noted that the structure of of the particles will influence both the magnitude of the maximum field enhancement and the volume within which the field enhancements remain large.[133] To investigate if this applies to arrays, we now use a simple electrostatic approach and investigate the field enhancements in two-dimensional square lattices of finite metallic spheres (S), finite cylinders (C), and finite blocks (B). The simulations are performed using the electrostatic module of COMSOL Multiphysics 3.3a, which is a Finite-Element based commercial numerical simulation software.

In Fig. 4.7 we schematically illustrate the numerical experiment. The structures are periodic square lattices as illustrated in Panel (a). For the cylinders and blocks when the separation distance d is small compared to the overall size of the individual structures D, the maximum field enhancement E_{max} occurs in the middle of the junction between two adjacent particles. For the spheres, a slightly larger field enhancement (10%) can sometimes be found on the sphere surface. For consistency, we will define the maximum field enhancement as the value in the middle of the junction. Using PBC the calculation of the fields needs only to be performed in a unit cell as shown in Panel (b). The left and right boundaries are set to be equipotential surfaces with electric potentials $V/2$ and $-V/2$, respectively. For the other bound-

aries we apply symmetric (zero charge) boundary conditions. When the separation d is changed, V is tuned so that the background electric field across the unit cell without any objects $E_0 = V/(D+d)$ is a constant, where D is the dimension of the object. For simplicity the dielectric constant of the objects is set to be minus infinity as appropriate for a perfect conductor. The maximum field enhancement factor η is defined as, $\eta = Emax/E_0$.

4.3.1 Maximum field enhancement as a function of particle separation

In Fig. 4.8 we show the calculated maximum electric field enhancement factor for the S, C, and B arrays as a function of relative separation d/D for thin junctions. We also show the analytical result $\eta = \frac{D+d}{d}$ for the field enhancement in a junction of thickness d between two metallic spheres of diameter D derived previously using electrostatic arguments.[134] In this approach, the enhancement factor $\eta = E_{loc}/E_i$ which is the ratio of the incident field E_i and the local field E_{loc}, can be derived from the condition for the potential $E_i(D+d) = E_{loc}d$, obtaining $E_{loc}/E_i = (D+d)/d$.[134] The results show almost identical field enhancement factors. The fact that the relation between η and d/D is the same for these very different structures is a consequence of perfect metallic screening. The maximum field enhancement is only dependent on the closest distance between two equipotential particles and not on the detailed structure around the junction.

In Fig. 4.9 we show the calculated local electric fields and the electrostatic equipo-

tential surfaces of the C and B arrays. In panel (a) we show the electric field enhancement in these two systems. For the C array there is a distinct hotspot but for the B array the electric field is almost uniformly distributed in the junctions. Although the shapes of the field enhancement are totally different, the maximum field enhancement factors are same in both systems. In panels (b) and (c) we show the electrostatic equipotential surfaces of these two systems. Although the overall electric potential distributions are different for the B and C array, the close-up around the hot-spots are nearly identical.

In the analysis above we studied arrays of nanoparticles of the same aspect ratio in the lateral dimensions. The magnitude of the maximum field enhancements in the electrostatic limit will depend on the aspect ratio of the individual particles.

A factor of crucial importance for the efficiency of a substrate for SES is associated with the sensing volume, i.e., the volume inside which the electromagnetic field enhancements are large. A large hotspot volume means that a larger number of molecules can be probed. In the next subsection we investigate how the hotspot volume of conductive arrays (an assumption valid to describe behavior in the infrared) depend on interparticle separation and shape of the particles.

4.3.2 Hotspot volume in arrays of particles of different geometry

In this subsection we investigate how the volume of the hotspots in the arrays junctions depend on interparticle separation and also shape of the particles. Since

the electric field enhancements can vary significantly in space and their relevance for different SES depend on the how the cross sections depend on the power of the field enhancement, the hotspot volume needs do be defined differently for different spectroscopies. For SEIRA we define the SEIRA efficiency as

$$\Sigma = \int E^2 \cdot dV, \tag{4.1}$$

with a hotspot volume defined as $V_H = \Sigma / E_{max}^2$. To evaluate the integral we need to do a subdomain integration of energy density $E^2 \cdot dV$ for each system.

In Fig. 4.10 we show the calculated hotspot volume for the S, C, and B arrays as a function of separation. On a logarithmic scale, the calculated V_H of these three arrays each follows an almost perfect linear dependence on d/D and can be parametrized as:

$$V_H^B \propto (d/D)^{1.035} \tag{4.2}$$

$$V_H^C \propto (d/D)^{1.431} \tag{4.3}$$

$$V_H^S \propto (d/D)^{1.742} \tag{4.4}$$

These results can simply be rationalized by analyzing the surface curvatures of the different particles. For the blocks, the surfaces are flat so that the lateral size of the hotspot always equals the surface area of the particles. Hence V_H increases linearly with separation. For the cylindrical particles, the lateral size of hotspot in the plane parallel to the cylinder axis is constant, while the dimension in the plane perpendicular

to the cylinder axis is proportional to $(d/D)^{0.5}$. Thus V_H of the cylindrical particles should be proportional to $(d/D)^{1.5}$. For the spherical particles the lateral dimension of the hotspot should be proportional to $(d/D)^{0.5}$ which would lead to V_H being proportional to $(d/D)^2$. We believe that the reason the simple geometrical analysis does not work exactly for the sphere array is caused by the more inhomogeneous field intensity distribution in the sphere array compared to for the cylinder and block array. An explicit calculation of the volume within which the field enhancement remain larger than 10% of the maximum enhancement gives the powers 1.038, 1.494, and 2.033 for the B, C and S arrays The hotspot volumes for the block arrays are much larger *and homogeneous* than for the sphere arrays, with those for the cylinder array in between. Since the maximum field enhancements only depend on the separation, the block or cylinder arrays provide better SEIRA substrates than 2D sphere arrays.

We close this subsection by illustrating how our findings can be applied to to optimize a configuration of metallic nanoparticles on a finite sized substrate for maximum SEIRA efficiency. For simplicity, we consider a single layer square array of rectangular metallic blocks of length L, widths W, and height W, separated by junctions of a length d. The question we ask is what is the optimal shape of the individual particles for a given substrate area. For simplicity we will assume light incident perpendicular to the substrate. The electrostatic analysis in subsection IIIA shows that the maximum field enhancements in the junctions for longitudinal polarization (polarization

along L) is proportional to $(L+d)/d$. The corresponding hotspot volume will be proportional to W^2d with a SEIRA efficiency proportional to $(L+d)^2W^2/d$. For transverse polarization (polarization along W), the maximum field enhancement is $(W+d)/d$ with a hotspot volume of LWd. The SEIRA efficiency for transverse polarization is thus $(W+d)^2LW/d$. The surface footprint per particle is $(L+d)(W+d)$. By maximizing the SEIRA efficiency for a fixed surface area, it can trivially be shown that the optimal SEIRA efficiency per unit surface area is achieved for longitudinal polarization and high aspect ratio (L/W) particles. Such a substrate may be realized by aligning finite carbon nanotubes on the substrate,[135] or by electron or focused ion beam milling of a thin metallic film. For more complicated structures, the optimization problem becomes a multi-variable problem which can straightforwardly be solved using linear programming methods such as the Simplex Method.

4.4 Summary and Discussions

Using the FDTD and FEM methods we have analyzed the electromagnetic properties of two-dimensional close-packed nanoshell arrays. We have shown that the extinction spectrum for normal incidence is characterized by a narrow resonance in the NIR and a broad structure in the MIR in qualitative agreement with experimental results. These resonances are formed through interactions and hybridization of the individual nanoshell plasmons. The NIR resonance originates from the quadrupolar resonances of the individual nanoshells and the MIR resonance derives from the

dipolar resonances of the individual nanoshells. The strong broadening of the MIR resonance is caused by radiative damping which for normal incidence result in super radiance, i.e. a collective enhancement of the radiation from several dipolar emitters oscillating in phase. An analysis of the electromagnetic field enhancements in the array structure reveals large field enhancements in the nanoparticle junctions both for the excitation of the NIR and the MIR modes. The field enhancements associated with the NIR resonance can be understood as a conventional resonant excitation of a weakly damped plasmon mode, with a wavelength dependence that follows the extinction spectrum. The field enhancements associated with the MIR show a qualitatively different wavelength dependence with a slow monotonous increase with increasing wavelength and a saturation to the electrostatic result at a wavelength beyond 20 microns. The field enhancements induced in the MIR are not caused by excitations of plasmons but are a consequence of metallic screening, i.e., the lightning rod effect. At long wavelengths, metals behave like a perfect equipotential conductors and all the field enhancements result results from the drop of the potentials across the junctions between individual nanoparticles. In this limit, the field enhancements depend only on the geometrical structure of the substrate. The slow monotonous increase of the field enhancements in the MIR is analogous to the response of an overdamped oscillator and is consistent with our finding of large radiative damping of the MIR resonance. Our observation that the maximum field enhancements in the MIR does not depend

sensitively on wavelength is another advantage for SEIRA where the measurements need to be performed over an extended spectral region.

We have demonstrated that the properties of field enhancement and hotspot volumes in the infrared region of the spectrum where SEIRA takes place can be described using analytical electrostatic arguments. Following this simplistic, but practical approach, we have identified in a very general way, the structural requirements for optimization of a substrate for maximum SEIRA efficiency. Our initial investigations indicate that such a substrate should be composed of high aspect ratio particles. In contrast to the hotspots associated with resonant excitation of plasmons in SERS, high field enhancements in the far infrared do not require sharp junctions, but rather the use of narrow flat junctions with large hotspot volumes. The field enhancement is also more constant and homogeneous, compared to the plasmonic resonances in the visible, therefore the common magnification of the infrared signal has the advantage of preserving the information on the relative weight of the absorption peaks. Moreover, due to the fact that the nature of the enhancement in the far infrared is connected with the exclusion of the field from the conductor-like material, the trends for optimizing the enhancement can be extrapolated to Terahertz frequency regions, thus having a great potential for SEIRA on biomolecules. The concepts shown in this communication could lead to a new paradigm in the design of efficient substrates for visible (SERS) and far infrared (SEIRA) spectroscopies.

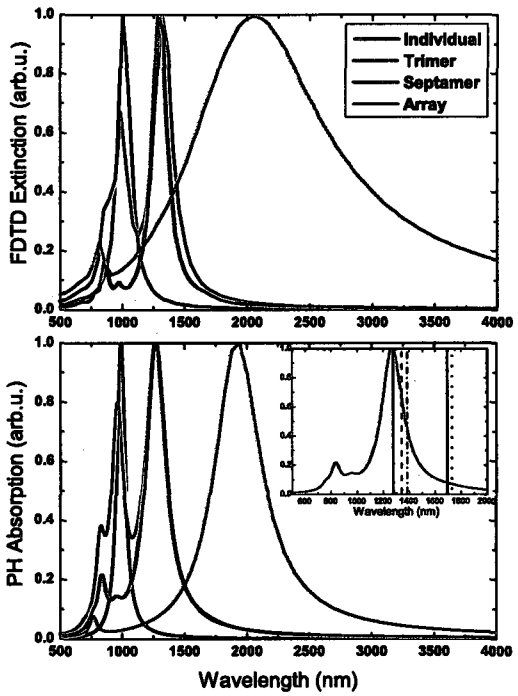

Figure 4.5 FDTD extinction spectra (a) and PH absorption spectra (b) of an individual nanoshell (black), a nanoshell trimer (red), a nanoshell septamer (blue) and an HCP nanoshell array (green). The inset in Panel (b) shows the energy and symmetry of the five lowest energy plasmon modes: E_{1u} (solid), A_{2g} (dotted), E_{2g} (dot-dashed), and B_{1u} (dashed) for the septamer calculated using PH. The size of nanoshells in each case is (R_1, R_2)=(18.75,21.5) nm, and the separation is d=1 nm. The calculations were performed using a pure Drude dielectric function with $\omega_B = 4.6$ eV and a damping of 0.15 eV.

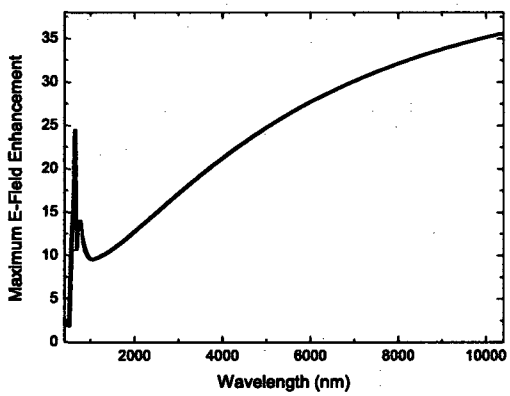

Figure 4.6 Maximum electric field enhancement factors in the HCP nanoshell array as a function of wavelength. The simulations are performed using COMSOL Multiphysics 3.3a. At MIR to IR regime (wavelength > 2000 nm) the maximum field enhancement factor steadily increases towards 35 at 10 microns. The maximum field enhancement saturates to a value around 40 beyond 20 microns.

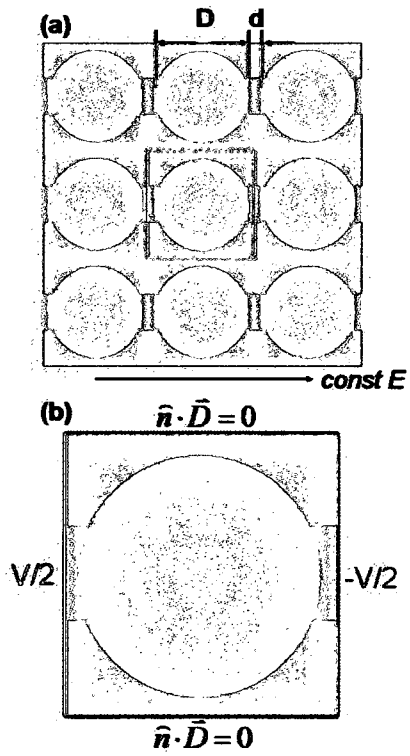

Figure 4.7 Schematic illustration of a typical COMSOL simulation on a 2D square lattice of spherical particles. The particles are perfect conductors with a diameter D and inter-particle separation d. Panel (b) shows the individual unit cell of the lattice. The left and right boundaries are equipotential boundaries with electric potentials $V/2$ and $-V/2$ respectively. The location of the hotspots in the nanoparticle junctions are illustrated in red and yellow.

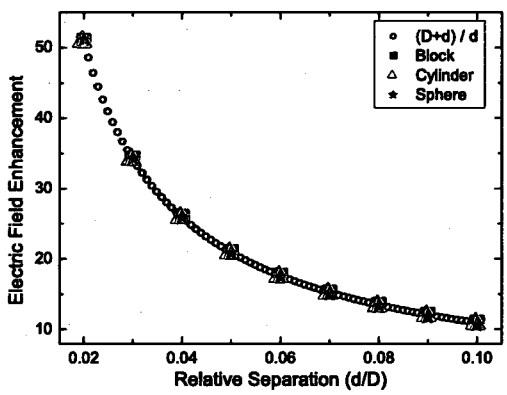

Figure 4.8 The maximum electric field enhancement factor η as a function of relative separation d/D for sphere, cylinder, and block arrays, respectively. The relation between η and d/D in these three systems almost overlap and can be parameterized as $\eta = (D+d)/d$.

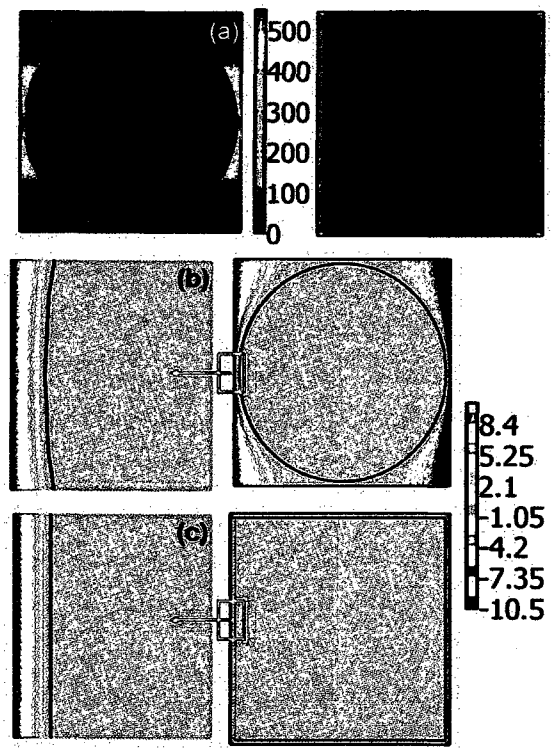

Figure 4.9 Local electric field enhancements and electrostatic potential surfaces for the 2D cylinder and block arrays. The applied electric field is $E_0 = 20$ and the relative separation is $d/D = 0.04$. Panel (a) shows the electric field enhancements for the C array (left) and the B array (right). Panel (b) shows the electric potential distribution in the C array (right) and the close-up (left). Panel (c) is organized as panel (b) but for the B array.

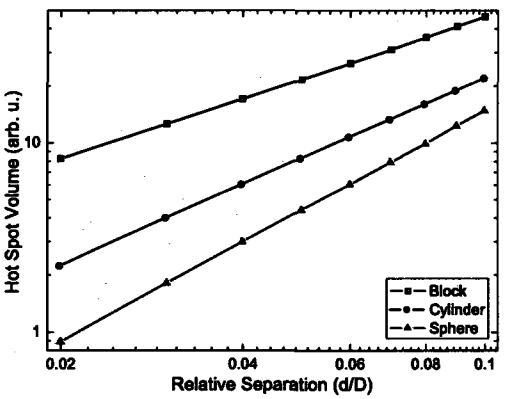

Figure 4.10 Hotspot volume V_H as a function of separation d/D for 2D square arrays of B, C, and S particles. The figure is plotted on a log-log scale and the slopes are 1.035 (B), 1.431 (C), and 1.742 (S).

Chapter 5
Nanoparticle Arrays with Oblique Incident Excitation

5.1 Introduction

The optical and plasmonic properties of metallic nanostructures have been of persistent interest to the scientific and engineering society during the last couple of years and have recently been the subject of several comprehensive reviews.[106, 136, 137] The resonant excitation of plasmons in a metallic nanostructure can induce large electromagnetic field enhancements. This phenomenon is the major factor responsible for large enhancements of Raman scattering of molecules adsorbed on the surfaces of the nanoparticles.[138, 139, 140] The plasmon resonances of a metallic nanoparticle depend sensitively on its geometrical structure.[141] This tunability which can be very significant for dielectric-core metallic-shell structures such as nanoshells,[142, 141, 143] has enabled a large number of applications of plasmonic nanoparticles in areas such as fluorescence enhancement,[26, 144, 145, 146] optical manipulation,[147, 148, 149] novel approaches to color displays,[150] and nanoscale PH meters.[151]

In parallel with the development of novel plasmonic applications there has been a substantial progress in the development of theoretical methods for the calculation of optical properties of metallic nanoparticles. Although, it is possible to calculate the optical properties of nanoparticle of general shape using analytical approaches,[152,

153, 154] such methods become cumbersome for strongly interacting systems such as nanoparticle pairs (dimers) separated by a narrow junction. For dimers and chains where the individual nanoparticles are characterized by a high degree of symmetry, multiple scattering approaches provide a computationally fast numerical approach.[155, 156] For multi-particle systems consisting of highly anisotropic nanoparticles, the most general approach is a brute force numerical solution of Maxwell's equations. One of the most prominent such approaches is the Finite-Difference Time-Domain (FDTD) method.[43] This method is based on spatial and temporal grid discretization and can provide exact numerical solutions for the optical properties of arbitrarily shaped objects of arbitrary composition. The disadvantage with fully numerical computational approaches is that they do not provide detailed physical insight into the problem. However, by analyzing the results from fully numerical methods using the Plasmon Hybridization (PH) concept,[106] it is often possible to interpret the optical spectra and explain the microscopic properties of the optically active plasmon resonances in a physically intuitive manner.[157, 158, 4, 159, 160]

One and two-dimensional nanoparticle arrays are examples of interesting nanostructures which present some challenging computational problems. Nanoparticle arrays can be fabricated relatively simply using self-assembly[126, 156] or lithographic methods,[161, 162] and are of considerable interest as substrates for surface enhanced spectroscopies because they provide a high concentration of junctions "hot-spots"

that can provide large field enhancements.[126, 163] One dimensional nanoparticle array structures also provide possible geometries for plasmonic waveguiding.[164, 34] As in any periodic structure, the plasmonic modes of an array form continuous bands where the resulting states represent traveling waves characterized by their Bloch wavevector.[104, 165, 166] While the optical properties of nanoparticle arrays for normal incidence can be calculated very simply using any numerical method by imposing Periodic Boundary Conditions (PBC), such boundary conditions cannot be imposed for oblique incidence of light. For oblique incidence, the electromagnetic fields reach different parts of the array at different times and the PBC implementation must take this retardation in account.

The two major advantages of the FDTD method compared to other numerical techniques are that a full spectral analysis can be obtained from a single simulation and that the method can be implemented very efficiently on parallel computer architectures.[43, 54] In the FDTD method one typically propagates an incident pulse in real time through the nanostructure. Since the temporal history of the electromagnetic fields can be stored, it is thus in principle possible to implement PBC taking into account that the PBC on the different sides of the unit cell should be implemented at different times. The difficulty with such an implementation is that one side of the PBC needs to be updated with times from the future, i.e. advanced times.[43]

Several methods for the extension of the FDTD method for periodic structure

under oblique incidence have been proposed.[43] The most widely used is the "Field Transformation Method" (FTM).[167, 168] The basic idea in FTM is to introduce a set of new field parameters to replace the original electric and magnetic field variables $\vec{E}$ and $\vec{H}$. These new fields, $\vec{P}$ and $\vec{Q}$, are in many respects very similar to $\vec{E}$ and $\vec{H}$ except that they contain the phase factor $e^{i\vec{k}\vec{r}}$. By doing this substitution, the requirement on future field values is evaded. However the modified Maxwell's Equations are much more difficult to solve and require very small grid sizes for large incident angles. For instance for the most popular FTM, the Split Field (SF) algorithm[43], due to the complexity in the modified Maxwell's Equations, the operation count per time step of SF is at least an order of magnitude higher than conventional FDTD. Besides, not only the auxiliary P_a and Q_a fields double the memory cost, but with frequency dispersive dielectric functions, the SF algorithm requires a significant amount of additional memory to store past field values up to four time steps while conventional FDTD only needs to store fields for two time steps. A conservative estimation on the memory usage of SF over conventional FDTD would thus be at least four times higher. The FTM has been used for Photonic Band Gap (PBG) substrates with frequency-independent dielectric properties.[169] The extension to metallic nanoparticles with frequency dependent dielectric functions results in significant further complications.[168]

In this chapter we investigate another method for the extension of the FDTD method to periodic structures for oblique incidence, the Multiple Unit Cell (MUC)

method.[43, 47, 170] In contrast to the FTM, this approach does not require a significant rewriting of an existing FDTD code and maintains the usual stability criterion for arbitrary incident angles. We discuss the details of the MUC implementation and present an investigation of numerical aspects such as computational overhead and convergence.

5.2 Implementation

The FDTD method is an explicit time marching algorithm for solving Maxwell's equations on a discretized spatial grid.[43] Each FDTD simulation typically takes thousands of iterations. During each iteration the $\vec{H}$ and $\vec{E}$-fields are updated alternately from the field values of the previous iteration using the curl form of Maxwell's equations.

The time-marching nature of FDTD imposes a certain obstacle when implementing PBC for oblique incident situations. In Fig. 5.1a we show the geometry of the problem. The incident angle with respect to the x-axis is ϕ_i which for simplicity will be assumed larger than zero and smaller than $\pi/2$. The periodicity of the array is D. In the frequency domain the PBC for Maxwell's equations take the form,[43],

$$\vec{H}(y = D) = \vec{H}(y = 0)exp(-jk_yD) \tag{5.1}$$

$$\vec{E}(y = 0) = \vec{E}(y = D)exp(+jk_yD), \tag{5.2}$$

where $k_y = k_0 sin\phi_i$ is the projection of the incident wavevector k_0 onto the y-axis.

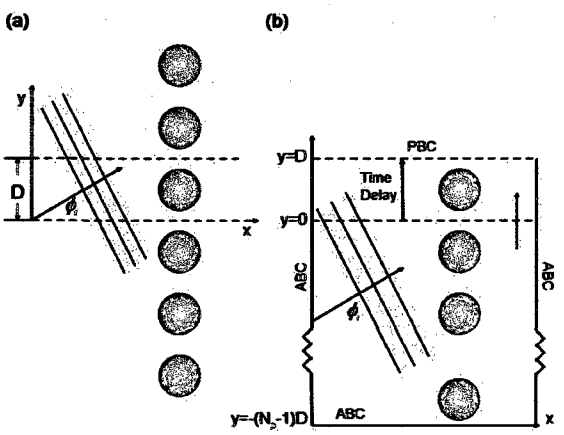

Figure 5.1 Schematic illustration of the geometry of the problem (a) and the MUC algorithm (b). The incident angle with respect to the x-axis is ϕ_i. The array is in the $\hat{y}$-direction with a periodicity D. In the MUC algorithm (b) the array is described as a finite structure of N_p cells. The unit cell is represented by the top cell between $y = D$ and $y = 0$. The $N_p - 1$ cells between $y = -D$ and $y = -(N_p - 1)D$ are referred to as the auxiliary structure. Retarded PBC are applied on the upper boundary $y = D$ while the fields on the lower boundary are updated normally from the auxiliary structure. Absorbing Boundary Conditions (ABC) are applied on all other boundaries.

For simplicity in the above equations we have neglected the half grid cell spatial offset between the $\vec{H}$ and $\vec{E}$ fields[43]. Since $\vec{H}$ and $\vec{E}$ fields are related by the Ampere's Law as well as the Faraday's Law, at each periodic boundary there is only one degree of freedom for them so that another version of Eq. (1) with $\vec{H}$ replaced by $\vec{E}$ and Eq. (4) with $\vec{E}$ replaced by $\vec{H}$ would be redundant. After transformation into time domain, the above equations take the form,

$$\vec{H}(y = D, t) = \vec{H}(y = 0, t - \Delta T) \tag{5.3}$$

$$\vec{E}(y = 0, t) = \vec{E}(y = D, t + \Delta T), \tag{5.4}$$

where $\Delta T = Dsin\phi_i/c$ is the time it takes for the incident wave to move a distance D

in the y-direction. In the following we will set the speed of light to c=1. The above equations shows that when the incident angle ϕ_i is non-zero, both past (retarded) field values at time $t - \Delta T$ and future (advanced) field values at time $t + \Delta T$ would be needed to update the $\vec{H}$ and $\vec{E}$ fields on the corresponding boundaries. The past field values can be stored using additional memory but the requirement on future fields represents a computational challenge.

The Multiple Unit Cell (MUC) method[43] can be considered as a semi-infinite array approximation so that the requirement of future field values is avoided. In Fig. 5.1(b) we illustrate the MUC algorithm. The system is modeled as a finite array of N_p nanoparticles. The unit cell is the top cell between $y = 0$ and $y = D$. The remaining $N_p - 1$ cells will be referred to as the auxiliary structure. Retarded PBC Eq. (5.3) are applied at $y = D$. The fields at the lower boundary are updated from the fields in the auxiliary structure using the conventional FDTD algorithm. The auxiliary structure is terminated with Absorbing Boundary Conditions (ABC) at $y = -(N_p - 1)D$. ABC are also used on the other surfaces surrounding the structure to eliminate reflections.

The introduction of ABC at $y = -(N_p - 1)D$ introduce an error at $y = 0$ which will decrease with increasing number of cells N_p. Previous studies using MUC has suggested that the spectra converge at five cells for one-dimensional arrays and 25 cells (5x5) for two-dimensional arrays.[47, 48] Our investigation shows that the number

of cells required for convergence depends on the periodicity D, the incident angle ϕ_i and the wavelength λ. The purpose of including the auxiliary structure is to provide a sufficient number of nanoparticles and space that the relevant Bloch waves can be excited. Therefore, the minimal number of cells N_{min} should be larger than at least half a full wavelength of the dominant plasmon wavelength, $\frac{1}{2}\lambda$. Here the factor $\frac{1}{2}$ comes from the fact that the other half of the wave will be generated by the periodic boundaries. A straightforward derivation shows that N_{min} takes the expression $N_{min}(\phi_i) = \lambda/(2D \cdot sin(\phi_i))$. The divergence at $\phi_i = 0$ means that an infinite number of nanoparticles need to be included to construct a full Bloch wave. However, since the interaction between nanoparticles decays rapidly for increasing separation, the spectrum converges at a finite chain length N_{int}. N_{int} depends on various parameters, including the geometry and material properties of particles, inter-particle separation, embedding medium, etc. For our specific structure, series of convergence tests have been performed and $N_{int} = 30$ at normal incidence. Therefore, N_{min} should be determined by the following equation:

$$N_{min}(\phi_i) = min(\lambda/(2D \cdot sin(\phi_i)), 30) \tag{5.5}$$

Despite the fact that MUC method requires more computational storage than ordinary FDTD, it is still quite appealing compared with the low efficiency for spectral analysis in the Sine-Cosine method[171] and the serious complications involved in

implementing FTM for frequency-dependent dielectric functions.[168]

5.3 Results

In this section we apply the MUC method for one-dimensional gold nanosphere arrays. Each nanosphere has a radius R=30 nm and the periodicity of the array is D=68 nm. The FDTD cell size is 2 nm in each direction. An investigation of the extinction spectra of an individual nanosphere calculated using this grid size showed no significant dependence of the angle of incidence caused by staircasing. The dielectric response of gold is modeled using a Drude form $\epsilon(\omega) = \epsilon_\infty - \omega_p^2/(\omega^2 + j\delta\omega)$, with parameters $\epsilon_\infty = 9.5$, ω_p=8.9488 eV and δ=0.06909 eV obtained by fitting to the experimental data for gold.[107] The system is placed in vacuum with no dielectric background or substrates. The absorbing boundary conditions consist of 10 cells of UPML. The time step is 3.34e-18 s and the number of time steps is 25,000. The excitation pulse is Gaussian enveloped sinusoid with a central frequency 428.6 THz, decay to 1/e time 8.89e-15 s. Far field monitors are applied on the planes perpendicular to the periodicity and they perform Discrete Fourier Transformations on received field values and convert the data to output in extinction.

In Fig. 5.2 we schematically illustrate the nature of the plasmon resonances in the nanosphere chain. Panels (a) and (b) show the transverse (T) and longitudinal (L) modes that are induced for normal incidence ($\phi_i = 0$). For S-polarization (E-field perpendicular to the plane determined by the nanosphere array and the incident

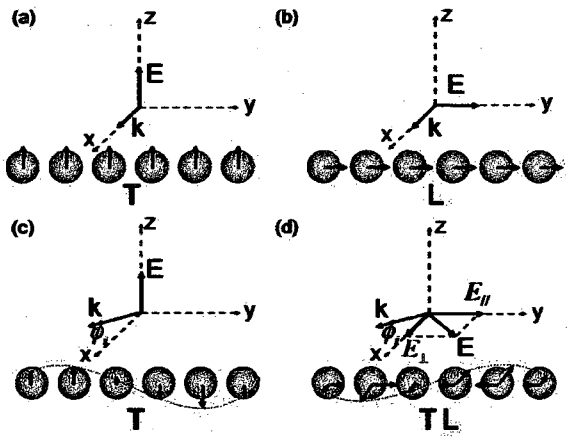

Figure 5.2 Schematic illustration of the plasmonic modes in one dimensional nanosphere arrays. Panel (a) shows the T mode at normal incidence. Panel (b) illustrates the L mode at normal incidence. Panel (c) shows the phase delayed T mode under S-polarization with non-zero ϕ_i. Panel (d) shows that both L and T phase delayed modes are excited for P-polarization at oblique incidence.

wave vector), the dipolar moments of all particles are excited perpendicular to the axis of the array. These dipoles collectively oscillates in phase. Due to the repulsive Coulomb interaction for this polarization, the collective plasmon resonance is blue shifted compared to the plasmon resonance for an individual nanosphere. For P-polarization (E-field parallel to the plane determined by the nanosphere array and the incident wave vector), only the L mode is excited. The dipolar moments of the nanoparticles are lined up along the chain and oscillate in phase. For this polarization, the Coulomb interaction is larger and attractive resulting in a redshifted collective mode.

Fig. 5.2c and 5.2d illustrate the effect of oblique excitation geometry. For such incidence, at a given time, the local electric field is different on each particle. The

phase delay modifies the Coulomb interaction between adjacent dipoles and the energy of the collective mode. For S-polarization, the Coulomb repulsion is reduced leading to a redshift of the T mode compared to normal incidence. For P-polarization the situation is slightly more complicated. As illustrated in Fig. 5.2d the electric field can be split into a parallel part $E_{\|} = Ecos\phi_i$ which interacts only with L modes and a perpendicular part $E_{\perp} = Esin\phi_i$ which only excites T modes. The effect of the phase delay on the T mode is the same as for S-polarization. The effect on the L modes is a reduction of the attractive Coulomb interaction between adjacent nanoparticles which leads to a blueshift of the L mode with increasing angle of incidence.

5.3.1 Convergence tests

Since the extinction maximum of an individual gold nanosphere of radius 30 nm is located around 480 nm, we can use this value as an approximation for λ, the wavelength of the dominant plasmon mode in the system. Equation (5.5) gives an estimate of the minimal number of cells $N_{min} = 3.53/sin(\phi_i)$ required for convergence. Therefore, for large incident angles, such as $\phi_i = 80°$, N_p=4 should be sufficient for spectral convergence. Small incident angles such as $\phi_i = 10°$ may need up to 20 cells.

In Fig. 5.3 (a) and (b) we show how the extinction spectra for P-polarization depend on N_p for two different angles of incidence. The short wavelength mode is a T mode and the long wavelength resonance is an L mode. The dispersion of these modes as the angle of incidence is varied will be discussed below in section IIIB.

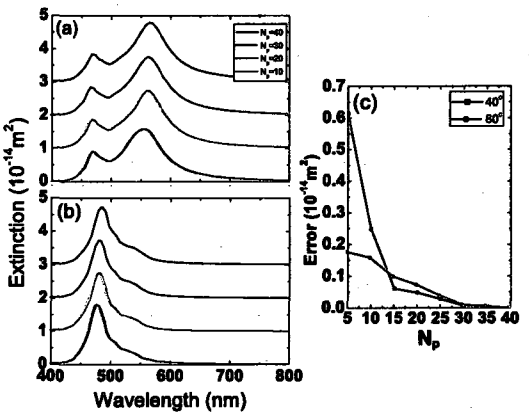

Figure 5.3 Convergence test on the nanosphere array with P-polarization. The incident angle is (a) $\phi_i = 40°$ and (b) $\phi_i = 80°$. Blue, Green, red and black curves are extinction spectra of the array simulated for N_p=10, 20, 30 and 40, respectively. All spectra are offset vertically. Panel (c) shows the error magnitude at the extinction peaks (564 nm for $\phi_i = 40°$ and 485 nm for $\phi_i = 80°$) versus different chain lengths N_p.

The figure shows that N_p=20 are sufficient for convergence of the lineshape of the resonances in agreement with our crude prediction using Eq. (5.5). A detailed analysis shows that the average difference in peak positions is around 10 nm for N_p=10 and 20, 4 nm for N_p=20 and 30, and smaller than 1 nm between N_p=30 and 40. In order to illustrate the improvement on convergence as N_p increases, in Panel (c) we plot the error magnitudes at the extinction peak positions (564 nm for $\phi_i = 40°$ and 485 nm for $\phi_i = 80°$). The error is defined as the absolute difference between the unconverged and the converged (N_p=40) extinction values. This panel shows that the convergence of the spectra improves considerably as N_p increases and we will normally use N_p=30 in the simulations presented below, with an estimated error of smaller than 1% compared to fully converged results.

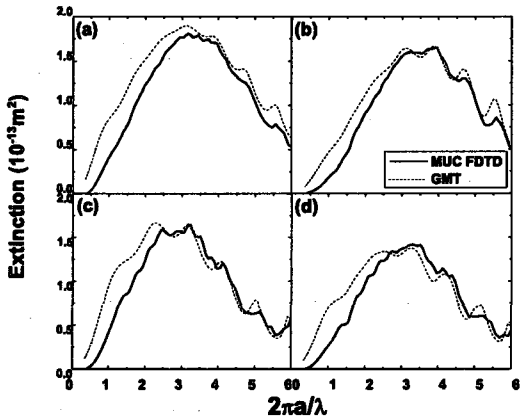

Figure 5.4 Comparison on extinction spectra of an infinite cylinder between MUC FDTD (black solid) and Generalized Mie Theory (red dashed). The extinction is measured for a unit length of cylinder (100 nm) and the radius of the cylinder is $a = 120nm$. The dielectric constant of the cylinder is $\epsilon = 2.25$. Panels (a) and (b) correspond to P and S polarizations for $\phi_i = 30°$, respectively. Panels (c) and (d) correspond to P and S polarizations for $\phi_i = 45°$, respectively.

To further test MUC FDTD, in the following we examine the extinction spectra of an infinite dielectric cylinder for oblique incidence. The optical properties of an infinite cylinder has been well studied and the analytical expression of the extinction cross-sections of an infinite cylinder under arbitrary incident angle is readily available[172] by means of the Generalized Mie Theory (GMT). In Fig. 5.4 we plot the extinction spectra per unit length (100 nm) of an infinite glass cylinder ($\epsilon = 2.25$) for a radius of $a = 120nm$. The FDTD model setup consists of a semi-infinite cylinder of 1200 nm in length, periodicity of 100 nm, and a cell size of 4 nm. In each panel the black curve is the simulation result from MUC FDTD and the red dashed curve is calculated using the GMT. Panels (a) and (b) stand for P and S polarizations

for an incident angle $\phi_i = 30°$ and panels (c) and (d) correspond to the P and S polarizations for $\phi_i = 45°$, respectively. The comparison between FDTD and GMT shows satisfactory agreement for both the lineshapes of the spectra as well as the extinction peak positions. This is a clear demonstration that MUC FDTD is capable of reproducing the analytical results from the Mie Theory.

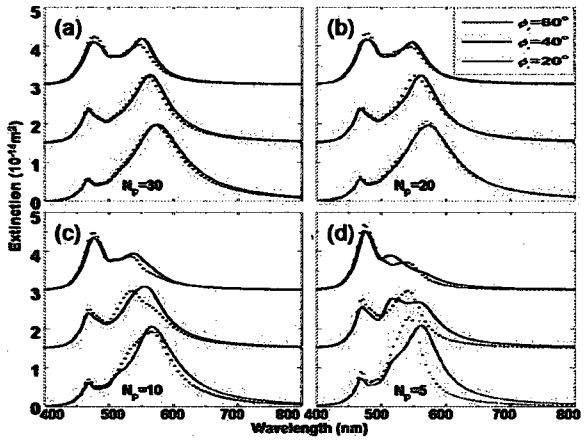

Figure 5.5 Comparison between the extinction spectra for P-polarization calculated with (solid lines) and without (dotted) the MUC algorithm for N_p= 30 (a), 20 (b), 10(c), and 5 (d). In each panel the incident angles are from top to bottom ϕ_i= 60° (black), 40° (red), and 20° (green). The spectra are offset vertically.

In spite of the MUC method using a large number of cells for convergence, it is still a superior method than a finite chain simulation. Figure 5.5 shows a comparison of the extinction spectra for P-polarization calculated using MUC and those simulated using finite chains for different chain lengths and angles of incidence. As demonstrated in Fig. 5.3, the MUC spectra for N_p=30 in panel (a) are fully converged. The panel shows that for the largest incidence angle, the L resonance is not fully accounted

for in the finite chain calculation. For N_p=20 (b), the difference between the MUC and the finite chain results are larger. For N_p=10 and 5, none of the spectra are converged. However, the MUC results are clearly closer to the converged results in panel (a) than the finite chain results. Interestingly the spectral shape of the T mode is well described even for the shortest chain. We believe that this is due to the relatively small interparticle interactions for transversely polarized dipoles.[173] It is also worthwhile to point out that the $\phi_i = 20°$ (green) spectra converge faster than the $\phi_i = 60°$ (black) spectra. This conclusion seems to contradicts Eq. (5) which implies that convergence is expected to be better for larger ϕ_i. The reason is that at large ϕ_i, the interaction potential among nanoparticles undergoes a frequent sign change due to strong phase delays.

5.3.2 Angular dependence of extinction spectra for S and P-polarization

In Fig. 5.6 we show the extinction spectra for a nanosphere array for S-polarization for different angles of incidence. For normal incidence, the spectrum is dominated by a narrow peak centered around 468 nm which is a T mode where the dipolar plasmons of all nanoparticles in the array oscillate in phase in a direction perpendicular to the array axis. As ϕ_i increases as discussed in Fig. 5.2, this peak redshifts because of the reduction of the Coulomb repulsion between two adjacent nanoparticle plasmons. The wavelength of this T mode for $\phi_i = 80°$ is 481 nm. The lineshapes of the peaks in each curve are almost the same except for a slight broadening as ϕ_i increases. The small

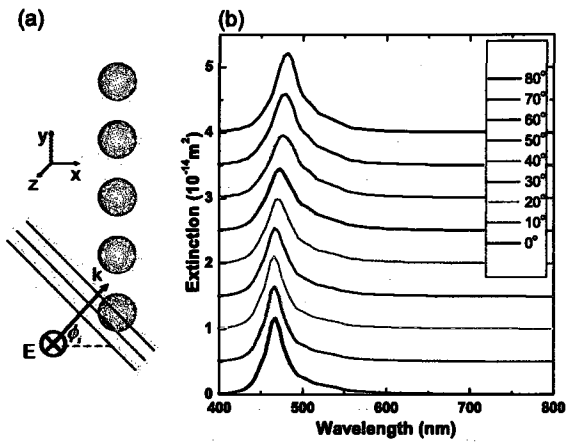

Figure 5.6 Extinction spectra of the one dimensional nanosphere array at different incident angles for S-polarization. Panel (a) shows the geometry and (b) shows the extinction spectra calculated for ϕ_i ranging from 0° to 80°, increased by units of 10°. The spectra are offset vertically.

shoulders around 510 nm and 530 nm in each spectrum are staircasing artifacts. It was shown that the shoulders around 510 nm and 530 nm also exist in the extinction spectrum of an individual nanosphere from the array and these spectral features can only be suppressed by refining the simulated geometry, i.e. decreasing the cell size while keeping the same physical size of the nanosphere.

In Fig. 5.7 we show the extinction spectra for P-polarization. As discussed in Fig. 5.2, for P-polarization we can excite both T and L modes with intensities determined by the angle of incidence, i.e. $(cos\phi_i)^2$ for L modes and $(sin\phi_i)^2$ for T modes. The spectra in Fig. 5.7 are characterized by a narrow short wavelength T resonance and a broader long wavelength L resonance. For normal incidence, the L resonance is located around 577 nm. The small feature at 470 nm for normal incidence is a

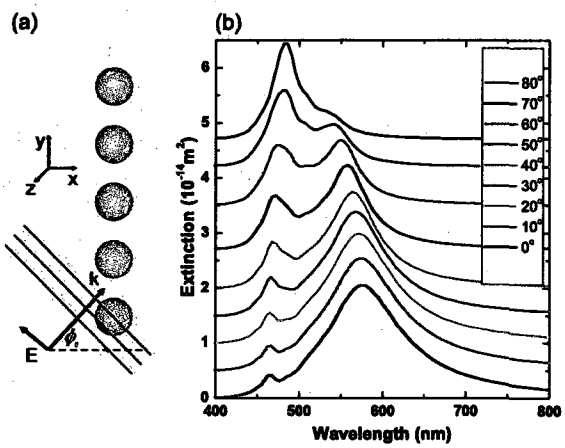

Figure 5.7 Same as Fig. 5.6 but for P-polarization.

hybridized longitudinal quadrupolar resonance.[173] This quadrupolar resonance is almost degenerate with the T resonance which cannot be excited for P-polarization for normal incidence. As ϕ_i increases, the long wavelength feature blueshifts and eventually reaches 545 nm for $\phi_i = 80°$. The intensity of the two L resonances decreases monotonously as ϕ_i increases.

The short wavelength T resonance exhibits the opposite behavior from the L mode. For normal incidence there is no transverse component of the electric field and the T mode at 468 nm is not excitable. The weak spectral feature at 470 nm is the aforementioned quadrupolar L mode. For the five smallest angles of incidence, $10° \leq \phi_i \leq 50°$, the transverse component of the incident field is finite and the short wavelength feature consists of both the T mode and the quadrupolar L mode. As the angle of incidence is increased further the T mode becomes the dominant mode and

exhibits the same redshift as was observed in Fig. 5.6.

5.4 Dispersion Relation of 1D Nanosphere Arrays

In this section we compare the dispersion relations of the 1D nanosphere array plasmons calculated using MUC with those obtained using a simple electrostatic point-dipole model.[104, 174, 166] In order to account for the dielectric screening effect on inter-particle interaction due to the background dielectrics of gold, we slightly modify the model derivation[174] by replacing the Drude dielectric function of gold with $\epsilon(\omega) = \epsilon_\infty - \omega_P^2/(\omega(\omega+i\delta))$, where $\epsilon_\infty = 9.5$ is the background dielectric constant of gold and $\omega_P = 8.9488eV$ is the bulk plasmon frequency of gold. δ is set to 0 to represent lossless material. In the non-retarded limit, the dipolar plasmonic mode of a gold nanosphere is[2] $\omega_0 = \omega_P\sqrt{\frac{1}{2+\epsilon_\infty}} = 2.64eV$. In order to correct the model for the retardation effect induced by the finite size of the nanosphere, ω_0 is replaced by the plasmonic energy of an individual gold nanosphere from FDTD calculation, i.e. $\omega_0 = 2.57eV$. Finally the electrostatic point-dipole model takes the form:

$$\omega^2(k_y) = \omega_0^2 \frac{1 + (\frac{R}{D})^3 \sum_{j=1}^{\infty} \kappa_{T,L} \frac{cos(jk_yD)}{j^3}}{1 + \frac{\epsilon_\infty - 1}{\epsilon_\infty + 2}(\frac{R}{D})^3 \sum_{j=1}^{\infty} \kappa_{T,L} \frac{cos(jk_yD)}{j^3}}. \tag{5.6}$$

The radius of the nanosphere is R=30 nm and the separation between adjacent nanospheres is D=68 nm. κ is a coefficient that depends on polarization with the value $\kappa = 2$ for T modes and $\kappa = -4$ for L modes. k_y is the wave vector along the

direction of the array. j refers to the j:th nearest neighbor. The sum over j converges rapidly and can be truncated at j=10.

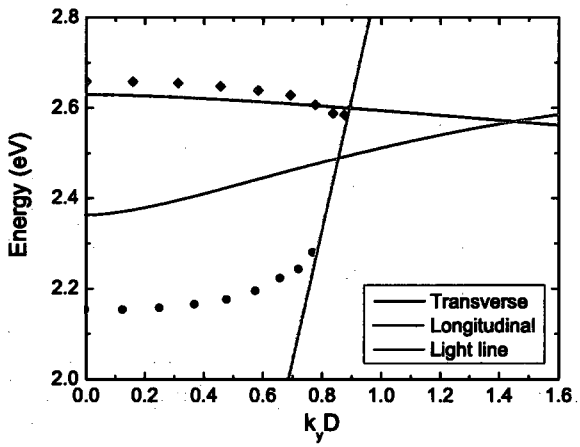

Figure 5.8 Dispersion relation of the one dimensional nanosphere array. The black (T) and red (L) curves are the results from the analytical model Eq. (5.6). The black and the red symbols are the dispersion relation obtained from the MUC calculations in Figs. 5.6 and 5.7. The green line is the light line.

In Fig. 5.8 we show the dispersion relations determined using the simple model Eq. (5.6). The dispersion relations extracted from the peak positions of the curves in Figs. 5.6 and 5.7 are shown with the symbols. The MUC results agree qualitatively with the simple analytical model showing a monotonous weak blueshift of the T mode and a stronger redshift of the L mode for increasing k_y. The green line is the light line determined by the relation $\omega = k_y c$. It can be seen that the transverse modes from the analytical model and MUC FDTD generally agree well while the longitudinal mode from FDTD appears to be around 0.2 eV below the prediction from

Eq. (5.6). The major reason for this is the neglect of the interactions with higher order multipolar plasmons from the analytical model. This interaction is generally much stronger for the L mode than the T mode and results in a hybridization of dipolar and higher multipolar plasmons for the L mode as was demonstrated in Fig. 5.7, where a quadrupolar L mode appeared for normal incidence. Since in our study the nanoparticle array has a relatively small separation (8 nm) compared to particle size (60 nm in diameter), the multipolar interaction is strong.

Several other groups[174, 175] have pointed out that the dispersion relation for the T modes should undergo a drastic change as it intersects the light line. When this happens, the T mode could decay (tunnel) into a free photon and both the dispersion and width of the T mode should be strongly modified near the light line. However, this effect is not observed in Fig. 5.8 and the reason is that the dispersion relation extracted from the FDTD simulation corresponds to the dispersion of real frequencies ω with respect to complex wavevectors $\vec{k}$, where damping causes the expected avoided-crossings in the T mode to merge[175]. In order to observe the avoided crossing described above, a computation on the dispersion relation of complex ω in terms of real $\vec{k}$ needs to be conducted, which is beyond the scope of the current paper.

5.5 Electric field enhancements

In the MUC method, only the electromagnetic fields in the unit cell are physically relevant. To reconstruct the fields in an infinite periodic array the fields in the unit

cell is translated to adjacent cells using the appropriate retarded or advanced PBC. In the geometry described in Fig. 5.1b we define the time domain electric field value at a given position $\vec{r}$ in the unit cell as $\vec{E}(\vec{r},t)$. The field values at time t in a cell at a distance nD from the unit cell can then be expressed as,

$$\vec{E}(\vec{r}-nD\hat{y},t)=\vec{E}(\vec{r},t-n\Delta T) \tag{5.7}$$

where $\Delta T = Dsin\phi_i$ is the time delay across the unit cell. In the frequency domain for a plane wave of frequency Ω, this time delay corresponds to a phase shift $e^{-nj\Omega\Delta T}$. With this relation, we can reconstruct the instantaneous electric fields around arbitrary particles in the array. The reconstruction method provides us with an intuitive and accurate visualization of the plasmonic modes in periodic nanoparticle arrays.

In Fig. 5.9 we show the instantaneous electric field enhancements for both T and L modes at the corresponding extinction maxima in Figs. 5.6 and 5.7 for each incident angle ϕ_i. The field enhancement is defined as the ratio of the instantaneous electric field and the electric field when the nanoparticles are absent. In each panel only the leftmost nanoparticle is located in the unit cell and the the field enhancements around the 19 remaining particles are obtained using Eq. (5.7).

For a plane wave of frequency ω incident at an angle ϕ_i, the projected wave vector along the chain is $k_y = \omega sin\phi_i$. The chain plasmons satisfy a dispersion relation $\omega_{chain}(k_y)$. The extinction maxima occur for chain plasmons where $\omega_{chain}(k_y) = \omega$. The period of the electric field enhancements in the chain is half of that of its

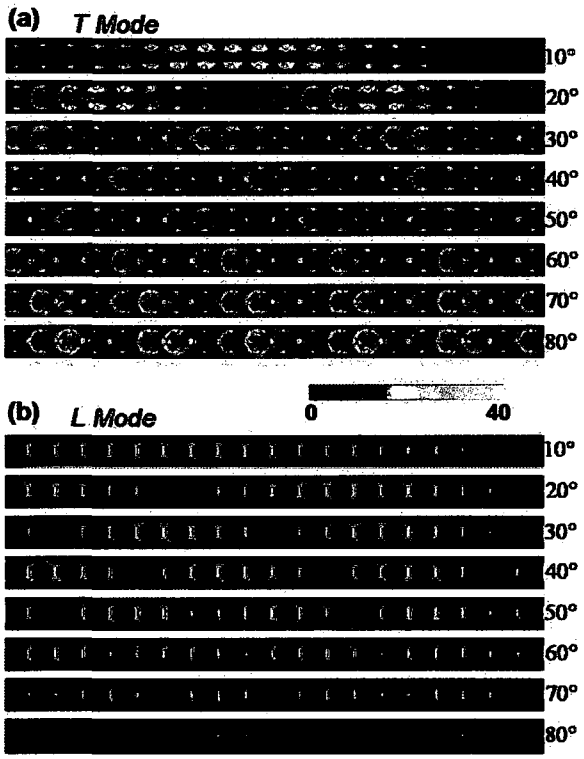

Figure 5.9 Instantaneous local electric field enhancements for the wavelengths corresponding to the extinction maxima of the T (a) and L (b) modes in Figs. 5.6 and 5.7. In each panel the field enhancements are reconstructed for incident angles ranging from 10° (top) to 80° (bottom). The wavelengths of the T modes are from top to bottom, 468, 468, 469, 471, 473, 477, 480, and 481 nm. The wavelengths for the T modes are, 577, 576 574, 571, 566, 559, 554, and 545 nm.

corresponding chain plasmon mode since the field enhancements are proportional to the square of the surface charges on the nanoparticles. It is instructive to express the period for the electric field enhancements in terms of the number of lattice constant D as,

$$P_E(\phi_i) = \frac{\lambda(\phi_i)}{2Dsin(\phi_i)} \tag{5.8}$$

For the T modes, this equation predicts P_E =19.8(10°), 10.1(20°), 6.90(30°), 5.39(40°),

4.54(50°), 4.05(60°), 3.76(70°), and 3.59(80°). For L mode, Eq. (5.8) predicts P_E= 24.4(10°), 12.4(20°), 8.44(30°), 6.53(40°), 5.42(50°), 4.75(60°), 4.33(70°), and 4.07(80°).

Figure 5.9 shows that the magnitude of the electric field enhancements depends both on polarization and angle of incidence. For the T modes, at small ϕ_i the local field is concentrated on the direction perpendicular to the array. As ϕ_i increases, the local electric field hotspots gradually merge into the junctions between adjacent nanospheres, indicating an increased inter-particle coupling due to the phase delay caused by the oblique incidence. For the L modes, the electric field is always concentrated in the junctions between neighboring nanospheres. For increasing ϕ_i, the phase delayed plasmonic interactions between adjacent nanoparticles results in a decreased magnitude of the field enhancements in the junctions.

5.6 Summary and Discussions

The implementation of oblique incident PBC represents a considerable challenge for time-domain methods such as FDTD. Numerous algorithms have been proposed but each has its own advantages and disadvantages. In this chapter we have investigated the numerical aspects of the Multiple Unit Cell method. We have shown that the method converges faster than a simple modeling of an array as a finite chain. Using this approach, we have studied the plasmonic properties of metallic nanoparticle arrays under oblique incident angles. We calculate the extinction spectra of one dimensional gold nanosphere array at different incident angles and polarizations. We

identify two basic modes, the narrow transverse mode at higher energy and the broad longitudinal mode at lower energy. Our investigation shows that S-polarization only excites the transverse mode while P-polarization excites both transverse and longitudinal modes and that the relative amplitude of these two modes is determined by the incident angle. The transverse mode exhibit a weak redshift and the longitudinal mode a stronger blueshift as the incident angle increases. The calculated dispersion relations are found to qualitatively agree with the dispersion relations obtained using a simple electrostatic model. We do not observe the predicted photon tunneling effect of the transverse mode near the light line.

Chapter 6
Conclusions

In this thesis, we apply both Plasmon Hybridization method and Finite-Difference Time-Domain method in analyzing and simulating various metallic nano-structures, such as the nanoparticle and metallic film structure, one and two dimensional arrays of nanoshells, etc. We focus on the extinction spectra and local electric field enhancements of these systems. We also compare our results with experimental measurements and the results from other analytical and numerical algorithms such as Mie Theory as well as the Finite Element method.

One of the main discoveries in our research is the virtual state (VS) induced by the plasmonic interactions between a nanoparticle (nanosphere, nanoshell, etc.) and a thin metallic film. When placed close to each other, the nanoparticle and the film plasmons can be coherently excited and the interaction between the discrete nanoparticle plasmons and the continuous film plasmons is highly analogous to what is depicted in the classic impurity model, the Anderson-Fano Model. We find that the nanoshell and film structure is a highly tunable system which has a plasmonic feature dependent on the geometric properties of both the nanoshell and the film. As the film thickness gradually decreases, three characteristic regimes are realized where the energy of the nanoparticle plasmon resonance lies above, within or below

the surface plasmon states. In the thin film limit, the plasmonic coupling between the nanoshell and the film induces a low energy VS consisting of delocalized thin film plasmons. We show that the energy and intensity of this state can be controlled both by changing the aspect ratio of the nanoshell and by changing the thickness of the film. The theoretical results are found to agree well with the experimental observations. Although the concept of VS was initially introduced by Anderson, to the best of our knowledge we are the first to apply it into nano-plasmonics.

Another important discovery lies in the spectral analysis of 2D hexagonal (hcp) arrays of nanoshells. During our study we find that the spectra calculated from FDTD do not perfectly match experimental measurements. The experimental extinction spectra shows a broad peak in mid-infrared (MIR) and a sharp peak in near-infrared (NIR). However, the FDTD simulation only shows the NIR sharp feature but the lower energy portion of the spectra are mostly structureless. Our later analysis shows that the difference is caused by the experimental defects in sample fabrication, which breaks the 2D hcp nanoshell array into small subdomains. These subdomains have different plasmonic eigenmodes and phases, which eventually cause destructive interference in their radiative fields. In contrast, FDTD simulates the hcp array as perfectly periodic and thus creates a strong super-radiant damping in MIR with all dipolar plasmons resonating in phase. Our research also demonstrates that the 2D hcp nanoshell array generates strong local electric field enhancements in both NIR

and MIR regimes. The NIR field enhancement is induced by the plasmonic coupling between adjacent nanoshells' quadrupolar plasmons while the MIR field enhancement is caused by the quasi-static field squeezing effect, in which the electric field is mostly concentrated in the gap between nanoshells as gold behaves like perfect conductors.

The FDTD investigation on the optical properties of oblique-incident 1D and 2D nanoparticle arrays also achieves success. It has been widely acknowledged that the implementation of oblique-incident Periodic Boundary Conditions (PBC) into FDTD is challenging, if not intimidating. The biggest obstacle lies in the frequency-to-time domain transformation, which turns the accumulated phase difference between ends of the periodic unit cells into time delayed and time advanced boundary update equations. In this thesis we apply the Multiple Unit Cell (MUC) method since it only requires moderate modifications to our existing FDTD program and meanwhile runs efficiently. Our research shows that the MUC method converges much faster than the finite chain approximation with a relatively small additional memory cost. We observe the Transverse and the Longitudinal modes and the dispersion relation from our simulation qualitatively agrees with the quasistatic model.

Appendix A
Derivation of the Lagrangian

The primitive film plasmons can be expressed in cylindrical Bessel Functions with an origin centered on the projection of the center of nanoshell on the film. $\vec{\rho} = (\rho, \phi)$ denotes the lateral position along the surface and z is the coordinate perpendicular to the surface. For the nanoshell plasmons we use spherical coordinates.

The Lagrangian for the nanoshell plasmons has been previously derived,[42] in which we showed that the plasmon energies of a nanoshell depend on $\omega_{B,S} = \sqrt{\frac{4\pi e^2 n_S}{m_e}}$, multipolar index l and its aspect ratio $x = a/b$,

$$\omega_{\pm}^2(x) = \frac{\omega_{B,S}^2}{2}[1 \pm \frac{1}{2l+1}\sqrt{1 + 4l(l+1)x^{2l+1}}]. \tag{A.1}$$

The bonding (-) and antibonding (+) eigenmodes are related to the primitive cavity and sphere modes as:

$$N_{lm}^{+} = C_{lm} sin\xi_l - S_{lm} cos\xi_l$$

$$N_{lm}^{-} = C_{lm} cos\xi_l + S_{lm} sin\xi_l, \tag{A.2}$$

where $tan\xi_l = \frac{\omega_{C,l}\omega_{S,l}}{\omega_{l+}^2 - \omega_{C,l}^2} x^{l+1/2}$.

The kinetic energy of the primitive plasmons of the film can be expressed as

$$T^{film} = \frac{n_F m_e}{2} \int dS \eta^* \nabla \eta, \tag{A.3}$$

where the integral is over the two surfaces of the film and the $*$ superscript denotes the complex conjugate. The integral can be evaluated analytically:

$$T^{film} = \frac{n_F m_e}{2} \int \frac{d\vec{k}}{(2\pi)^2} k(1 - e^{-2kT})[\dot{P}^2_{\vec{k}} + \dot{Q}^2_{\vec{k}}]. \tag{A.4}$$

The potential energy of the primitive plasmons of the film can be expressed as

$$V^{film} = \frac{1}{2} \int dS \phi^* \sigma, \tag{A.5}$$

where $\phi(\vec{r})$ and $\sigma(\vec{r})$ are the electrostatic potential and surface charge generated by the primitive plasmons of the film respectively. The integral can be evaluated analytically and takes the form:

$$\begin{aligned} V^{film} &= \frac{n_F m_e}{2} \frac{\omega^2_{B,F}}{2} \int \frac{d\vec{k}}{(2\pi)^2} k(1 - e^{-2kT}) \\ &\times [P^2_{\vec{k}} + Q^2_{\vec{k}} - 2P_{\vec{k}} Q_{\vec{k}} e^{-kT}].. \end{aligned} \tag{A.6}$$

The Lagrangian for the film $L^{film} = T^{film} - V^{film}$ can be written in a diagonal form by introducing bonding and antibonding combinations of P and Q,

$$M_{\vec{k}\pm} = \frac{1}{\sqrt{2}}(P_{\vec{k}} \pm Q_{\vec{k}}), \tag{A.7}$$

which can be shown to correspond to the plasmonic states of a thin film with energies

$$\omega_{\vec{k},\pm}(T) = \frac{\omega_{B,F}}{\sqrt{2}} \sqrt{1 \pm \exp[-kT]}. \tag{A.8}$$

In this representation the Lagrangian takes the form:

$$L^{film} = \frac{n_F m_e}{2} \sum_{j=\pm} \int \frac{d\vec{k}}{(2\pi)^2} k(1 - e^{-2kT})[\dot{M}^2_{\vec{k}j} - \omega^2_{\vec{k}j} M^2_{\vec{k}j}]. \tag{A.9}$$

The surface plasmons of the film form a continuous band ranging from zero energy up to the bulk plasmon frequency of the metal. The plasmonic density of states is peaked around the surface plasmon energy $\omega_{sp} = \omega_{B,F}/\sqrt{2}$. The plasmonic density of states depends strongly on film thickness. For infinite thickness, the film plasmons have no dispersion and the plasmonic density of states is a delta function centered on the surface plasmon energy $\omega_{sp} = \omega_{B,F}/\sqrt{2}$. For decreasing film thickness, the density of states broadens in energy. The modes $M_{\vec{k}\pm}$ represent the linearly independent, non-interacting plasmons of a thin film. In the presence of the nanoparticle, they no longer represent stationary states of the system.

The interaction between the film plasmons and the nanoshell plasmons is conveniently evaluated as an integral over the surface charge of the shell and takes the form:

$$V = \sum_{lm} \int \frac{d\vec{k}}{(2\pi)^2} R^2 \int d\Omega_{C,S} \phi^*_{\vec{k}i}(\vec{r}) \sigma_{lm}(\Omega_{C,S}), \tag{A.10}$$

where

$$\phi_{\vec{k}i} = \sqrt{2}\pi n_F e M_{\vec{k}i}(1 - e^{-2kT}) e^{i\vec{k}\cdot\vec{\rho}} e^{-kz} \tag{A.11}$$

is the electrostatic potential outside the film (for $z > 0$) from the primitive film plasmons and σ_{lm} is the charge density associated with the shell plasmons on both the cavity and the outer sphere surfaces.

We now make use of the azimuthal symmetry of the problem and expand the

exponential terms in $\phi_{\vec{k}i}$ in a Fourier series[81]

$$e^{i\vec{k}\cdot\vec{\rho}} = \sum_m i^m e^{-im\phi'} J_m(k\rho) e^{im\phi}, \tag{A.12}$$

where J_m is a cylindrical Bessel function of order m. We also introduce the Fourier transform

$$M_j(k,m) = \frac{i^m}{\sqrt{2\pi}} \int d\phi' M_{\vec{k}j} \exp[-im\phi']. \tag{A.13}$$

In this notation the interaction V becomes diagonal in azimuthal m and the Lagrangian of the combined system can be written $L = \sum_m L^m$, where

$$\begin{aligned} L^m &= \frac{n_S m_e}{2} \sum_{l,i=\pm} [\dot{N}^2_{lm,i} - \omega^2_{l,i} N^2_{lm,i}] \\ &+ \frac{n_F m_e}{2} \sum_{j=\pm} \int \frac{dk}{(2\pi)^2} k^2 (1 - e^{-2kT}) \\ &\times [\dot{M}^2_j(k,m) - \omega^2_{k,j} M^2_j(k,m)] \\ &+ \sqrt{\pi} n_F n_S e^2 \sum_l \sqrt{lR} y^m_l \sum_{i=\pm,j=\pm} \int dk k (1 - e^{-2kT}) \\ &\times e^{-kZ_0} I^m_{lk,i,j} N_{lm,i} M_j(k,m) \end{aligned} \tag{A.14}$$

where Z_0 is the distance between the center of the shell and the film surface and y^m_l is the normalization constant for the spherical harmonics. The integral

$$\begin{aligned} I^m_{kl,+,+} &= I^m_{kl,+,-} = F_1 I^m_{Ckl} + F_3 I^m_{Skl} \\ I^m_{kl,-,+} &= I^m_{kl,-,-} = F_2 I^m_{Ckl} + F_4 I^m_{Skl} \end{aligned} \tag{A.15}$$

where

$$I^m_{Ckl} = \int_0^\pi d\theta sin\theta J_m(kasin\theta) P^m_l(cos\theta) e^{-kacos\theta}$$

$$
\begin{aligned}
&= \frac{2}{2l+1}\frac{(-ka)^l}{(l-m)!} \\
I^m_{Skl} &= \int_0^\pi d\theta sin\theta J_m(kbsin\theta)P^m_l(cos\theta)e^{-kbcos\theta} \\
&= \frac{2}{2l+1}\frac{(-kb)^l}{(l-m)!}
\end{aligned} \tag{A.16}
$$

and

$$
\begin{aligned}
F_1 &= \sqrt{\frac{l+1}{a^3}}sin\xi_l + x^{l-1}\sqrt{\frac{l}{b^3}}cos\xi_l \\
F_2 &= \sqrt{\frac{l+1}{a^3}}cos\xi_l - x^{l-1}\sqrt{\frac{l}{b^3}}sin\xi_l \\
F_3 &= -x^{l+2}\sqrt{\frac{l+1}{a^3}}sin\xi_l - \sqrt{\frac{l}{b^3}}cos\xi_l \\
F_4 &= -x^{l+2}\sqrt{\frac{l+1}{a^3}}cos\xi_l + \sqrt{\frac{l}{b^3}}sin\xi_l
\end{aligned} \tag{A.17}
$$

With the substitutions

$$
N_{lm,i} \rightarrow \sqrt{\frac{2}{n_S m_e}}N_{lm,i} \tag{A.18}
$$

and

$$
M_j(k,m) \rightarrow \frac{2\pi}{k\sqrt{1-e^{-2kT}}}\sqrt{\frac{2}{n_F m_e}}M_j(k,m), \tag{A.19}
$$

the interaction term takes the form:

$$
\begin{aligned}
V^m_{lk,i,j}(Z_0) &= \sqrt{\pi}\omega_{B,F}\omega_{B,S}y^m_l\sqrt{lR}\sqrt{1-e^{-2kT}}e^{-kZ_0} \\
&\times \; I^m_{lk,i,j},
\end{aligned} \tag{A.20}
$$

resulting in the Lagrangian Eq. (3.2).

Appendix B
Discretization and Vector notation

The Lagrangian Eq. (3.2), can be discretized by introducing a vector $\vec{X}$ representing the amplitudes of the primitive plasmons. A particularly convenient choice is

$$\vec{X} = (N_{lm}^{-}, N_{lm}^{+}; \sqrt{\triangle k} M_{-}(k,m), \sqrt{\triangle k} M_{+}(k,m))^{T}, \tag{B.1}$$

with $l = 1, 2, ..., l_{max}$ and $k = 1, 2, ..., k_{max}$. In this expression $\triangle k$ is the spacing between adjacent wavevectors of the thin film plasmons.

In this representation, the kinetic energy matrix $\hat{T}_X$ is diagonal with,

$$\hat{T}_X = \begin{pmatrix} 1 - x^{2l+1} & & 0 \\ & \cdots & \\ 0 & & 1 - e^{-2kT} \end{pmatrix}, \tag{B.2}$$

with $l = 1, 2, ..., l_{max}$ and $k = 1, 2, ..., k_{max}$.

The potential energy matrix takes the form:

$$\hat{V}_X = \begin{pmatrix} \hat{V}_{ll} & \hat{V}_{lk} \\ \hat{V}_{kl} & \hat{V}_{kk} \end{pmatrix}, \tag{B.3}$$

where $l = 1, 2, ..., l_{max}$ and $k = 1, 2, ..., k_{max}$, with

$$\hat{V}_{ll} = (1 - x^{2l+1}) \begin{pmatrix} \omega_{l,-}^{2}(x) & 0 \\ 0 & \omega_{l,+}^{2}(x) \end{pmatrix}, \tag{B.4}$$

and

$$\hat{V}_{kk} = (1 - e^{-2kT}) \begin{pmatrix} \omega_{k,-}^2(T) & 0 \\ 0 & \omega_{k,+}^2(T) \end{pmatrix}, \tag{B.5}$$

and

$$\begin{aligned} \hat{V}_{lk} = \hat{V}_{kl} &= \frac{1}{2} y_l^m \sqrt{\pi \triangle k} \omega_{B,S} \omega_{B,F} (1 - e^{-2kT}) e^{-kZ_0} \\ &\times \begin{pmatrix} I_{kl,-,-}^m & I_{kl,-,+}^m \\ I_{kl,+,-}^m & I_{kl,+,+}^m \end{pmatrix}. \end{aligned} \tag{B.6}$$

The appearance of the $\sqrt{\triangle k}$ term here and in several equations below is due to our choice of $\vec{X}$ in Eq. (B.1).

It is useful to introduce a vector $\vec{\sigma}$ representing the surface charges associated with the primitive plasmons. We define this vector as

$$\vec{\sigma} = (\sigma_{C,l}, \sigma_{S,l}, \triangle k \sigma_{P,k}, \triangle k \sigma_{Q,k})^T, \tag{B.7}$$

where $l = 1, 2, ..., l_{max}$, $k = 1, 2, ..., k_{max}$. The surface charges $\sigma_{C,l}$ and $\sigma_{S,l}$ are the surface charges associated with the discrete cavity and sphere plasmons of the nanoshell and $\sigma_{P,k}$ and $\sigma_{Q,k}$ are the surface charges associated with the primitive film plasmons for a specific wavevector k. The $\triangle k$ factor in front of the primitive film plasmons arises from our discrete sampling of a continuum of primitive film plasmons.

With this definition, the physical surface charges associated with the primitive

plasmons can be expressed as $\vec{\sigma} = \hat{B} \cdot \hat{X}$, where

$$\hat{B} = \begin{pmatrix} \hat{B}_{shell} & 0 \\ 0 & \hat{B}_{film} \end{pmatrix}. \tag{B.8}$$

The transformation matrix for the nanoshell takes the form:

$$\hat{B}_{shell} = n_s e \begin{pmatrix} \hat{B}_1 & & 0 \\ & \cdots & \\ 0 & & \hat{B}_{l_{max}} \end{pmatrix}, \tag{B.9}$$

with

$$\hat{B}_l = \begin{pmatrix} F_2 & F_1 \\ F_4 & F_3 \end{pmatrix} \tag{B.10}$$

where the quantities F_i are defined in Eq. (A.17). The transformation matrix for the film takes the form:

$$\hat{B}_{film} = n_f e \begin{pmatrix} \hat{B}_1 & & 0 \\ & \cdots & \\ 0 & & \hat{B}_{k_{max}} \end{pmatrix}, \tag{B.11}$$

with

$$\hat{B}_k = \sqrt{\triangle k} \begin{pmatrix} 1 + e^{-kT} & 1 - e^{-kT} \\ -1 - e^{-kT} & 1 - e^{-kT} \end{pmatrix}. \tag{B.12}$$

In the discussion of the effects of background dielectrics, it becomes useful to express the potential energy of the system in terms of the surface charge vector $\vec{\sigma}$,

$$V = \frac{1}{2} \vec{\sigma}^T \hat{V}_\sigma \vec{\sigma}. \tag{B.13}$$

In this representation, the potential energy matrix takes the form

$$\hat{V}_\sigma = (\hat{B}^{-1})^T \hat{V}_X \hat{B}^{-1} \tag{B.14}$$

To achieve convergence for the systems studied in the present paper, we include all nanoshell plasmons up to $l_{max} = 40$ and employ a uniform discretization of the film continuum with a wavevector cut-off of $1nm^{-1}$ and $k_{max} = 800$.

Appendix C
Effects of dielectric background

In this section we discuss the effects of dielectric screening in the structure. We consider background dielectric polarizabilities of the metallic structures and the dielectrics of nonplasmonic embedding media. We will use the following notations to represent the permittivities of the different media: ϵ_C for the nanoshell core, ϵ_S for the metallic shell, ϵ_1 for an embedding medium around the nanoshell and above the metallic film, ϵ_F for metallic film background, and ϵ_2 for a dielectric substrate below the metallic film.

The effects of background dielectrics in the PH method is straightforward. In the presence of background dielectrics, the electrostatic energy in the system takes the form,

$$V = \frac{1}{2}\vec{\sigma}^T \hat{V}_\sigma \vec{\sigma}^{total}. \tag{C.1}$$

where σ refers to the real surface charge densities induced by the primitive plasmons and σ^{total} are the total surface charges (real+induced). The effects of background dielectric can thus conveniently be included through a matrix $\hat{\chi}$ that relates the total charges to the real charges, $\vec{\sigma}^{total} = \hat{\chi}\vec{\sigma}$. Using this relation the potential energy for the primitive plasmons in the presence of dielectric backgrounds takes the form,

$$V = \frac{1}{2}\vec{\sigma}^T \hat{V}_\sigma \hat{\chi} \vec{\sigma}$$

$$= \frac{1}{2}\vec{X}^T\hat{V}_X\hat{B}^{-1}\hat{\chi}\hat{B}\vec{X}$$
$$= \frac{1}{2}\vec{X}^T\hat{V}_X^D\vec{X}, \tag{C.2}$$

where, $\hat{V}_X^D = \hat{V}_X\hat{B}^{-1}\hat{\chi}\hat{B}$, is the potential energy matrix for dielectric systems and $\hat{V}_X$ is the potential energy matrix calculated in the absence of dielectric backgrounds.

The inverse matrix $\hat{E} = \hat{\chi}^{-1}$ can be calculated directly from the discontinuities of the displacement field at the boundaries of the dielectrics,

$$\epsilon_{i+1}\frac{\partial\Phi}{\partial r}|_{R_i^+} - \epsilon_i\frac{\partial\Phi}{\partial r}|_{R_i^-} = -4\pi\sigma_i, \tag{C.3}$$

where Φ_i is the potential generated by the $i:th$ total surface charge.

The electrostatic potential from the primitive plasmons of the nanoshell takes the form,

$$\Phi_{shell} = \sum_l \frac{4\pi}{2l+1}[a^2 v_l(r,a)\sigma_{C,l}^{total} + b^2 v_l(r,b)\sigma_{S,l}^{total}] \tag{C.4}$$

with $v_l(r,r') = \frac{r_<^l}{r_>^{l+1}}$, where $r_<$ and $r_>$ refer to the smaller and the larger of r and r', respectively. The electrostatic potential from the primitive film plasmons takes the form,

$$\Phi_{film} = \sum_k \frac{2\pi}{k}[e^{-k|z|}\sigma_{P,k}^{total} + e^{-k|z+T|}\sigma_{Q,k}^{total}] \tag{C.5}$$

Using these two expressions, the final expression for the matrix $\hat{E}$, is

$$\hat{E} = \begin{pmatrix} \hat{E}_{ll} & \hat{E}_{lk} \\ \hat{E}_{kl} & \hat{E}_{kk} \end{pmatrix}, \tag{C.6}$$

where $l = 1, 2, ..., l_{max}$ and $k = 1, 2, ..., k_{max}$, with

$$\hat{E}_{ll} = \begin{pmatrix} \frac{\epsilon_S(l+1)+\epsilon_C l}{2l+1} & \frac{(\epsilon_C-\epsilon_S)lx^{l-1}}{2l+1} \\ \frac{(\epsilon_1-\epsilon_S)(l+1)x^{l+2}}{2l+1} & \frac{\epsilon_1(l+1)+\epsilon_S l}{2l+1} \end{pmatrix}, \tag{C.7}$$

$$\hat{E}_{kk} = \begin{pmatrix} \frac{\epsilon_1+\epsilon_F}{2} & \frac{\epsilon_1-\epsilon_F}{2}e^{-kT} \\ \frac{\epsilon_2-\epsilon_F}{2}e^{-kT} & \frac{\epsilon_F+\epsilon_2}{2} \end{pmatrix}, \tag{C.8}$$

$$\begin{aligned} \hat{E}_{lk} &= \sqrt{\frac{\pi}{2k}} y_l^m l e^{-kZ_0} \\ &\times \begin{pmatrix} (\epsilon_C - \epsilon_S)\frac{I^m_{Ckl}}{a} & (\epsilon_C - \epsilon_S)\frac{I^m_{Ckl}}{a}e^{-kT} \\ (\epsilon_S - \epsilon_1)\frac{I^m_{Skl}}{b} & (\epsilon_S - \epsilon_1)\frac{I^m_{Skl}}{b}e^{-kT} \end{pmatrix}, \end{aligned} \tag{C.9}$$

and

$$\begin{aligned} \hat{E}_{kl} &= -\sqrt{\frac{\pi}{2}} y_l^m l k \triangle k e^{-kZ_0} \\ &\times \begin{pmatrix} (\epsilon_1 - \epsilon_F) I^m_{Ckl} a^2 & (\epsilon_1 - \epsilon_F) I^m_{Skl} b^2 \\ (\epsilon_F - \epsilon_2) I^m_{Ckl} a^2 e^{-kT} & (\epsilon_F - \epsilon_2) I^m_{Skl} b^2 e^{-kT} \end{pmatrix}. \end{aligned} \tag{C.10}$$

References

1. S. Maier, *Plasmonics: Fundamentals and Applications* (Springer, Berlin, 2007).
2. E. Prodan, C. Radloff, N. J. Halas, and P. Nordlander, Science **302**, 419 (2003).
3. D. S. Citrin, Opt. Lett. **31**, 98 (2006).
4. D. Neuhauser and K. Lopata, J. Chem. Phys. **127**, 154715 (2007).
5. S. Oldenburg, R. D. Averitt, S. Westcott, and N. J. Halas, Chem. Phys. Lett. **288**, 243 (1998).
6. S. Gresillon, L. Aigouy, A. C. Boccara, J. C. Rivoal, X. Quelin, C. Demarest, P. Gadenne, V. A. Shubin, A. K. Sarychev, and V. M. Shalaev, Phys. Rev. Lett. **82**, 4520 (1999).
7. R. Jin, Y. Wei, C. A. Mirkin, K. L. Kelly, G. C. Schatz, and J. G. Zheng, Science **294**, 1901 (2001).
8. M. I. Stockman, S. V. Faleev, and D. J. Bergman, Phys. Rev. Lett. **87**, 167401 (2001).
9. J. Bosbach, C. Hendrich, F. Stietz, T. Vartanyan, and F. Trager, Phys. Rev. Lett. **89**, 257404 (2002).
10. J. Aizpurua, P. Hanarp, D. S. Sutherland, M. Kall, G. W. Bryant, and F. J. G. de Abajo, Phys. Rev. Lett. **90**, 057401 (2003).
11. C. J. Murphy, T. K. San, C. J. Orendorff, J. X. Gao, L. Gou, S. E. Hunyadi, and T. Li, J. Phys. Chem. B **109**, 13857 (2005).
12. S. Nie and S. R. Emory, Science **275**, 1102 (1997).
13. K. Kneipp, Y. Wang, H. Kneipp, L. T. Perelman, I. Itzkan, R. R. Dasari, and M. S. Feld, Phys. Rev. Lett. **78**, 1667 (1997).
14. A. M. Michaels, M. Nirmal, and L. E. Brus, J. Am. Chem. Soc. **121**, 9932 (1999).
15. H. X. Xu, E. J. Bjerneld, M. Kall, and L. Borjesson, Phys. Rev. Lett. **83**, 4357 (1999).

16. G. C. Schatz and R. P. van Duyne, in *Handbook of Vibrational Spectroscopy*, edited by J. M. Chalmers and P. R. Griffiths (John Wiley, Chichester, 2002), pp. 1–16.

17. M. Moskovits and D. H. Jeong, Chem. Phys. Lett. **397**, 91 (2004).

18. Z. Wang, S. Pan, T. D. Krauss, H. Dui, and L. J. Rothberg, Proc. Nat. Acad. Sci. USA **100**, 8638 (2003).

19. J. B. Jackson and N. J. Halas, Proc. Nat. Acad. Sci. USA **101**, 17930 (2004).

20. R. Aroca and B. Price, J. Phys. Chem. B **101**, 6537 (1997).

21. M. Osawa, Top. Appl. Phys. **81**, 163 (2001).

22. M. Futamata, L. Luo, and C. Nishihara, Surf. Sci **590**, 196 (2005).

23. C. E. Talley, J. B. Jackson, C. Oubre, N. K. Grady, C. W. Hollars, S. M. Lane, T. R. Huser, P. Nordlander, and N. J. Halas, Nano Lett. **5**, 1569 (2005).

24. D. W. Brandl, C. Oubre, and P. Nordlander, J. Chem. Phys. **123**, 024701 (2005).

25. H. Wang and N. J. Halas, Nano Lett. **6**, 2945 (2006).

26. J. Zhang, Y. Fu, M. H. Chowdury, and J. R. Lakowicz, J. Phys. Chem. C **111**, 11784 (2007).

27. H. Watanabe, N. Hayazawa, Y. Inouye, and S. Kawata, J. Phys. Chem. B **109**, 5012 (2005).

28. T. Ichimura, N. Hayazawa, M. Hashimoto, Y. Inouye, and S. Kawata, Phys. Rev. Lett. **92**, 220801 (2004).

29. V. A. Fedotov, M. Rose, S. L. Prosvirnin, N. Papasimakis, and N. I. Zheludev, Phys. Rev. Lett. **99**, 147401 (2007).

30. D. Schurig, Int. J. Numer. Model. **19**, 215 (2006).

31. N. Liu, H. Guo, L. Fu, S. Kaiser, H. Schweizer, and H. Giessen, Adv. Mater. **19**, 3628 (2007).

32. J. Henzie, M. H. Lee, and T. W. Odom, Nature Nanotech. **2**, 549 (2007).

33. S. A. Maier, P. E. Barclay, T. J. Johnson, M. D. Friedman, and O. Painter, Appl. Phys. Lett. **84**, 3990 (2004).

34. S. A. Maier, M. L. Brongersma, P. G. Kik, S. Meltzer, A. G. Requicha, and H. A. Atwater, Adv. Mat. **13**, 1501 (2001).

35. M. Quinten, A. Leitner, J. R. Krenn, and F. R. Aussenegg, Opt. Lett. **23**, 1331 (1998).

36. W. E. Kock, Proc. IRE and Waves and Electrons **34**, 828 (1946).

37. D. J. R. J. B. Pendry, A. J. Holden and W. J. Stewart, IEEE Trans. Microwave Theory Tech. **47**, 2075 (1999).

38. A. Grbic and G. V. Eleftheriades, Phys. Rev. Lett **92**, 117403 (2004).

39. D. Schurig, J. J. Mock, B. J. Justice, S. A. Cummer, J. B. Pendry, A. F. Starr, and D. R. Smith, Science **314**, 977 (2006).

40. H. Boutayeb, T. A. Denidni, K. Mahdjoubi, A. Tarot, A. Sebak, and L. Talbi, IEEE Trans. Antenn. Prop. **54**, 211 (2006).

41. N. Engheta, Science **317**, 1698 (2007).

42. E. Prodan and P. Nordlander, J. Chem. Phys. **120**, 5444 (2004).

43. A. Taflove and S. C. Hagness, *Computational Electrodynamics: The Finite-Difference Time Domain Method* (Artech House, INC., Norwood, MA 02062, 2000).

44. D. M. Sullivan, *Electromagnetic Simulation Using the FDTD Method* (IEEE Press, Piscataway, NJ 08855-1331, 2000).

45. K. S. Yee, IEEE Trans. Antenn. Prop. **17**, 585 (1966).

46. G. Mur, IEEE Trans. Electromagnetic Compatibility **23**, 377 (1981).

47. J. Ren, O. P. Gandhi, L. R. Walker, J. Fraschilla, and C. R. Boerman, IEEE Microwave Guided Wave Lett. **4**, 109 (1994).

48. K. H. Lee and S. R. Laxpati, Proc. 1996 IEEE Antennas and Propagation Society International Symposium, Baltimore, MD **2**, 1284 (1996).

49. M. Fujii, D. Lukashevich, I. Sakagami, and P. Russer, IEEE Trans. Microwave Wireless Comp. Lett. **13**, 469 (2003).

50. S. Schmidt and G. Lazzi, IEEE Trans. Microwave Theory Tech. **52**, 1952 (2004).

51. O. Hess, C. Hermann, and A. Klaedtke, Phys. Stat. Sol. **197**, 605 (2003).

52. W. Kuang, W. J. Kim, and J. D. O'Brien, J. Lightwave Technol. **25**, 2612 (2007).

53. B. Wu, E. Yang, J. A. Kong, J. A. Oswald, K. A. McIntosh, L. Mahoney, and S. Verghese, Microw. Opt. Techn. Let. **27**, 81 (2000).

54. C. Oubre and P. Nordlander, J. Phys. Chem. B **109**, 10042 (2005).

55. C. Oubre and P. Nordlander, J. Phys. Chem. B **108**, 17740 (2004).

56. D. W. Brandl, N. A. Mirin, and P. Nordlander, J. Phys. Chem. B **110**, 12302 (2006).

57. D. W. Brandl and P. Nordlander, J. Chem. Phys. **126**, 144708 (2007).

58. F. Hao and P. Nordlander, Appl. Phys. Lett. **89**, 103101 (2006).

59. E. Yablonovich, Phys. Rev. Lett. **58**, 2059 (1987).

60. P. W. Anderson, Phys. Rev. **109**, 1492 (1958).

61. D. S. Wiersma, P. Bartolini, A. Lagendijk, and R. Righini, Nature **390**, 671 (1997).

62. P. Nordlander, C. Oubre, E. Prodan, K. Li, and M. I. Stockman, Nano Lett. **4**, 899 (2004).

63. W. R. Holland and D. G. Hall, Phys. Rev. Lett. **52**, 1041 (1984).

64. R. R. Chance, A. Prock, and R. Silbey, Adv. Chem. Phys. **37**, 1 (1978).

65. N. Felidj, J. Aubard, G. Levi, J. R. Krenn, G. Schnider, A. Leitner, and F. R. Aussenegg, Phys. Rev. B **66**, 245407 (2002).

66. P. W. Anderson, Phys. Rev. **124**, 41 (1961).

67. U. Fano, Phys. Rev. **124**, 1866 (1961).

68. G. D. Mahan, *Many-Particle Physics* (Kluwer Academic/Plenum Publishers, New York, 2000).

69. D. M. Newns, Phys. Rev. **178**, 1123 (1969).

70. R. Brako and D. M. Newns, Rep. Prog. Phys. **52**, 655 (1989).

71. J. C. Tully, Ann. Rev. Phys. Chem. **51**, 153 (2000).

72. J. Merino and J. B. Marston, Phys. Rev. B **69**, 115304 (2004).

73. P. Aravind and H. Metiu, Surf. Sci **124**, 506 (1983).

74. G. Videen, J. Opt. Soc. A. **8**, 483 (1991).

75. T. Okamoto and I. Yamaguchi, J. Phys. Chem. B **107**, 10321 (2003).

76. M. M. Wind, J. Vlieger, and D. Bedeaux, Physica A **141**, 33 (1987).

77. T. Yamaguchi, S. Yoshida, and A. Kinbara, Thin Solid Films **21**, 172 (1974).

78. V. V. Gozhenko, L. G. Grechko, and K. W. Whites, Phys. Rev. B **68**, 125422 (2003).

79. H. R. Stuart and D. G. Hall, Phys. Rev. Lett. **80**, 5663 (1998).

80. A. Pinchuk, A. Hilger, and G. von Plessen, Nanotechnology **15**, 1890 (2004).

81. P. Nordlander and E. Prodan, Nano Lett. **4**, 2209 (2004).

82. U. Kreibig and M. Vollmer, *Optical properties of metal clusters* (Springer, New York, 1995).

83. W. L. Barnes, A. Dereux, and T. W. Ebbeson, Nature **424**, 824 (2003).

84. S. I. Bozhevolnyi, E. D. V. S. Volkov, J. Y. Laluet, and T. W. Ebbeson, Nature **440**, 508 (2006).

85. J. Takahara, S. Yamagishi, H. Taki, A. Morimoto, and T. Kobayashi, Opt. Lett. **22**, 475 (1997).

86. J. R. Krenn, B. Lamprecht, H. Ditlbacher, G. Schider, M. Salerno, A. Leitner, and F. R. Aussenegg, Europhys. Lett. **60**, 663 (2002).

87. R. Zia, M. D. Selker, P. B. Catrysse, and M. L. Brongersma, J. Opt. Soc. Am. A **21**, 2442 (2004).

88. S. Link and M. A. El-Sayed, J. Phys. Chem. B **103**, 8410 (1999).

89. T. R. Jensen, M. D. Malinsky, C. L. Haynes, and R. P. van Duyne, J. Phys. Chem. B **104**, 10549 (2000).

90. A. Dmitriev, T. Pakizeh, M. Kall, and D. S. Sutherland, Small **3**, 294 (2007).

91. Z. Yuan and S. Gao, Phys. Rev. B **73**, 155411 (2006).

92. F. Wang and Y. R. Shen, Phys. Rev. Lett. **97**, 206806 (2006).

93. B.-H. Choi, H.-H. Lee, S. Jin, S. Chun, and S.-H. Kim, Nanotechnology **18**, 075706 (2007).

94. P. K. Aravind, A. Nitzan, and H. Metiu, Surf. Sci. **110**, 189 (1981).

95. K. R. Li, M. I. Stockman, and D. J. Bergman, Phys. Rev. Lett. **91**, 227402 (2003).

96. K. H. Su, Q. H. Wei, X. Zhang, J. J. Mock, D. R. Smith, and S. Schultz, Nano Lett. **3**, 1087 (2003).

97. W. Rechberger, A. Hohenau, A. Leitner, J. R. Krenn, B. Lamprecht, and F. R. Aussenegg, Optics Comm. **220**, 137 (2003).

98. D. P. Fromm, A. Sundaramurthy, P. J. Schuck, G. Kino, and W. E. Moerner, Nano Lett. **4**, 957 (2004).

99. C. Dahmen, B. Schmidt, and G. von Plessen, Nano Lett. **7**, 318 (2007).

100. R. Ruppin, Phys. Rev. B **45**, 11209 (1992).

101. M. Futamata, Y. Maruyama, and M. Ishikawa, J. Phys. Chem. B **107**, 7607 (2003).

102. S. A. Maier, M. L. Brongersma, P. G. Kik, and H. A. Atwater, Phys. Rev. B **65**, 193408 (2002).

103. G. Shvets and Y. A. Urzhumov, Phys. Rev. Lett. **93**, 243902 (2004).

104. S. Y. Park and D. Stroud, Phys. Rev. B **69**, 125418 (2004).

105. E. M. Hicks, S. Zou, G. C. Schatz, K. G. Spears, R. P. van Duyne, L. Gunnarsson, T. Rindzevicius, B. Kasemo, and M. Kall, Nano Lett. **5**, 1065 (2005).

106. H. Wang, D. W. Brandl, P. Nordlander, and N. J. Halas, Acc. Chem. Res. **40**, 53 (2007).

107. P. B. Johnson and R. W. Christy, Phys. Rev. B **6**, 4370 (1972).

108. G. Mie, Ann. Phys. **25**, 377 (1908).

109. H. X. Xu, J. Aizpurua, M. Kall, and P. Apell, Phys. Rev. E **62**, 4318 (2000).

110. S. A. Maier and H. A. Atwater, J. Appl. Phys. **98**, 011101 (2005).

111. L. Qin, S. Zou, C. Xue, A. Atkinson, G. C. Schatz, and C. A. Mirkin, Proc. Natl. Acad. Sci. USA **103**, 13300 (2006).

112. J. Zhu, Appl. Surf. Sci. **253**, 8729 (2007).

113. P. R. Evans, G. A. Wurtz, R. Atkinson, W. Hendren, D. O'Connor, W. Dickinson, R. J. Pollard, and A. V. Zayats, J. Phys. Chem. C **111**, 12522 (2007).

114. J. Zhang, M. H. Chowdhury, and J. R. Lakowicz, Nano Lett. **7**, 2101 (2007).

115. P. Johansson, H. X. Xu, and M. Kall, Phys. Rev. B **72**, 035427 (2005).

116. J. W. Gibson and B. R. Johnson, J. Chem. Phys. **124**, 064701 (2006).

117. B. G. Janesko and G. E. Scuseria, J. Chem. Phys. **125**, 124704 (2006).

118. Z. E. Goude and P. T. Leung, Solid State Commun. **143**, 416 (2007).

119. T. R. Jensen and R. P. van Duyne, Appl. Spectrosc. **54**, 371 (2000).

120. N. Goutev and M. Futamata, Appl. Spectrosc. **57**, 506 (2003).

121. K. Rodriguez, S. Shah, S. M. Williams, S. Teters-Kennedy, and J. V. Coe, J. Chem. Phys. **121**, 8671 (2004).

122. D. Enders, S. Rupp, A. Kuller, and A. Pucci, Surf. Sci **600**, L305 (2006).

123. R. D. Averitt, D. Sarkar, and N. J. Halas, Phys. Rev. Lett. **78**, 4217 (1997).

124. K. L. Kelly, E. Coronado, L. L. Zhao, and G. C. Schatz, J. Phys. Chem. B **107**, 668 (2003).

125. F. Neubrech, T. Kolb, R. Lovrincic, G. Hahsold, A. Pucci, J. Aizpurua, T. W. Cornelius, M. E. Toimil-Molares, R. Neuman, and S. Karim, Appl. Phys. Lett. **89**, 253104 (2006).

126. H. Wang, J. Kundu, and N. J. Halas, Angew. Chem. Int. Ed. **46**, 9040 (2007).

127. A. Taflove, *Advances in computational electrodynamics: The finite-difference time domain method* (Artech House, INC., Norwood, MA 02062, 1998).

128. R. H. Dicke, Phys. Rev. **89**, 472 (1953).

129. A. Christ, Y. Ekinci, H. H. Solak, N. A. Gippius, S. G. Tikhodeev, and O. J. F. Martin, Phys. Rev. B **76**, 201405R (2007).

130. Y. A. Urzhumov, G. Shvets, J. Fan, F. Capasso, D. W. Brandl, and P. Nordlander, Opt. Express **15**, 14129 (2007).

131. L. Mandel and E. Wolf, *Optical Coherence and Quantum Optics* (Cambridge, Cambridge, 1995).

132. J. Gersten and A. Nitzan, J. Chem. Phys. **73**, 3023 (1980).

133. P. F. Liao and A. Wokaun, J. Chem. Phys. **76**, 751 (1982).

134. H. X. Xu, E. J. Bjerneld, J. Aizpurua, P. Apell, L. Gunnarsson, S. Petronis, B. Kasemo, C. Larsson, F. Hook, and M. Kall, Proc. SPIE **4258**, 35 (2001).

135. L. Lou, P. Nordlander, and R. E. Smalley, Phys. Rev. B **52**, 1429 (1995).

136. J. K. Ghosh and T. Pal, Chem. Rev. **107**, 4797 (2007).

137. N. Harris, M. J. Ford, P. Mulvaney, and M. B. Cortie, Gold Bull. **41**, 5 (2008).

138. S. Lal, N. K. Grady, J. Kundu, C. S. levin, J. B. Lassiter, and N. J. Halas, Chem. Soc. Rev. **37**, 898 (2008).

139. M. J. Banholzer, J. E. Millstone, L. Qin, and C. A. Mirkin, Chem. Soc. Rev. **37**, 885 (2008).

140. C. Stanciu, M. Sackrow, and A. J. Meixner, J. Microscopy **229**, 247 (2008).

141. N. J. Halas, MRS Bulletin **30**, 362 (2005).

142. C. Radloff and N. J. Halas, Nano Lett. **4**, 1323 (2004).

143. V. V. Kulish and P. M. Tomchuk, Surf. Sci. **602**, 1045 (2008).

144. V. Giannini and J. A. Sanchez-Gil, Opt. Lett. **33**, 899 (2008).

145. S. D. Liu, M. T. Cheng, Z. J. Yang, and Q. Q. Wang, Opt. Lett. **33**, 851 (2008).

146. F. Tam, G. P. Goodrich, B. R. Johnson, and N. J. Halas, Nano Lett. **7**, 496 (2007).

147. M. Ringler, T. A. Klar, A. Schwemer, A. S. Susha, J. Stehr, G.Raschke, S. Funk, M. Borowsky, A. Nichtl, K. Kurzinger, R. T. Phillips, and J. Feldmann, Nano Lett. **7**, 2753 (2007).

148. U. Hakanson, M. Agio, S. Kuhn, L. Rogobete, T. Kalkbrenner, and V. Sandoghdar, Phys. Rev. B **77**, 155408 (2008).

149. J. Ng, R. Tang, and C. T. Chan, Phys. Rev. B **77**, 195407 (2008).

150. J. A. Gordon and R. W. Ziolkowski, Solid State Comm. **146**, 228 (2008).

151. S. W. Bishnoi, C. J. Rozell, C. S. Levin, M. K. Gheith, B. R. Johnson, D. H. Johnson, and N. J. Halas, Nano Lett. **6**, 1687 (2006).

152. D. Sarkar and N. J. Halas, Phys. Rev. E **56**, 1102 (1997).

153. J. Zhu, Appl. Phys. A **88**, 673 (2007).

154. D. J. Wu, X. D. Xu, and X. J. Liu, Solid State Comm. **146**, 7 (2008).

155. R. L. Chern, X. X. Liu, and C. C. Chang, Phys. Rev. E **76**, 016609 (2007).

156. B. N. Khlebtsov, V. A. Khanadeyev, J. Ye, D. W. Mackowski, G. Borghs, and N. G. Khlebtsov, Phys. Rev. B **77**, 035440 (2008).

157. F. Hao, C. L. Nehl, J. H. Hafner, and P. Nordlander, Nano Lett. **7**, 729 (2007).

158. H. Liu, D. A. Genov, D. M. Wu, Y. M. Liu, Z. W. Liu, C. Sun, S. N. Zhu, and X. Zhang, Phys. Rev. B **76**, 073101 (2007).

159. I. Romero, T. V. Teperik, and F. J. G. de Abajo, Phys. Rev. B **77**, 125403 (2008).

160. A. Christ, G. Leveque, O. J. F. Martin, T. Zentgraf, J. Kuhl, C. Bauder, H. Giessen, and S. G. Tikhdeev, J. Microscopy **229**, 344 (2008).

161. K. B. Crozier, E. Togan, E. Simsek, and T. Yang, Opt. Express **15**, 17482 (2007).

162. C. Langhammer, M. Schwind, B. Kasemo, and I. Zoric, Nano Lett. **8**, 1461 (2008).

163. F. Le, D. W. Brandl, Y. A. Urzhumov, H. Wang, J. Kundu, N. J. Halas, J. Aizpurua, and P. Nordlander, ACS Nano **2**, 707 (2008).

164. S. A. Maier, P. G. Kik, and H. A. Atwater, Phys. Rev. B **67**, 205402 (2003).

165. M. L. Brongersma, J. W. Hartman, and H. A. Atwater, Phys. Rev. B **62**, R16356 (2000).

166. A. F. Koenderink, R. de Waele, J. C. Prangsma, and A. Polman, Phys. Rev. B **76**, 201403 (2007).

167. J. A. Roden, S. D. Gedney, M. P. Kesler, J. G. Marloney, and P. H. Harms, IEEE Trans. Microwave Theory Tech. **46**, 420 (1998).

168. G. Zheng, A. A. Kishk, A. W. Glisson, and A. B. Yakovlev, Progress In Electromagnetics Research **59**, 85 (2006).

169. C. Oh and M. J. Escuti, Opt. Express **14**, 11870 (2006).

170. R. T. Lee and G. S. Smith, IEEE Trans. Antenn. Prop. **54**, 698 (2006).

171. T. Noda, T. Kanetani, and K. Uchidat, IEICE Transactions on Electronics **E79-C**, 1772 (1996).

172. C. Bohren and D. Huffman, *Absorption and scattering of light by small particles* (John Wiley & Sons, Ltd., New York, 1983).

173. J. B. Lassiter, J. Aizpurua, L. I. Hernandez, D. W. Brandl, I. Romero, S. lal, J. H. Hafner, P. Nordlander, and N. Halas, Nano Lett. **8**, 1212 (2008).

174. W. H. Weber and G. W. Ford, Phys. Rev. B **70**, 125429 (2004).

175. A. F. Koenderink and A. Polman, Phys. Rev. B **74**, 033402 (2006).